2019

A Kinetic Monte Carlo Study of Mesoscopic Perovskite Solar Cell Performance Behavior

Behzad Bahrami
South Dakota State University

Recommended Citation

Bahrami, Behzad, "A Kinetic Monte Carlo Study of Mesoscopic Perovskite Solar Cell Performance Behavior" (2019). *Electronic Theses and Dissertations*. 3185.
https://openprairie.sdstate.edu/etd/3185

A KINETIC MONTE CARLO STUDY OF MESOSCOPIC PEROVSKITE SOLAR CELL PERFORMANCE BEHAVIOR

BY

BEHZAD BAHRAMI

A dissertation submitted in partial fulfillment of the requirements for the

Doctor of Philosophy

Major in Electrical Engineering

South Dakota State University

2019

A KINETIC MONTE CARLO STUDY OF MESOSCOPIC PEROVSKITE SOLAR CELL PERFORMANCE BEHAVIOR

BEHZAD BAHRAMI

This dissertation is approved as a creditable and independent investigation by a candidate for the Doctor of Philosophy in Electrical Engineering and is acceptable for meeting the dissertation requirements for this degree. Acceptance of this dissertation does not imply that the conclusions reached by the candidate are necessarily the conclusions of the major department.

Qiquan Qiao, Ph.D. Date
Dissertation Advisor

George Hamer, Ph.D. Date
Acting Head, Department of Electrical
Engineering
and Computer Science

Dean, Graduate School Date

ACKNOWLEDGEMENTS

The work presented in this dissertation was supported by grants from the NSF MRI (grant no. 1428992), NASA EPSCoR (grants NNX13AD31A and NNX15AM83A), and the U.S. - Egypt Science and Technology Joint Fund EE Ph.D. program by the State of South Dakota.

I would like to express my sincere gratitude to Dr. Qiquan Qiao for providing the opportunity to work as a graduate research assistant in the Center for Advanced Photovoltaics at South Dakota State University. Dr. Qiao’s guidance and encouragement have been crucial throughout the course of my research work and in improving the technical quality of this dissertation.

I would also like to thank Dr. Parashu Kharel, Dr. Alireza Salehnia, Dr. Huitian Lu and Dr. George Langelett, my thesis committee members, for their time and consideration in reviewing this dissertation. I am equally thankful to Dr. Brian Moore for his support in high performance computing and giving me the chance to learn about cluster computing.

Special thanks to Sally Mabrouk, Ashim Gurung, Khan Mamun Reza, Ashraful Haider Chowdhury, and all my group members for helping me with solar cell fabrication and characterization, as well as their general friendship and support during this period.

Finally, I would like to thank my family and friends for their love, support, motivation, and continuous encouragement.

TABLE OF CONTENTS

LIST OF FIGURES ix

LIST OF TABLES xiii

ABSTRACT xiv

Chapter 1: Introduction 1

  1.1 Background 1

    1.1.1 First Generation Solar Cells 3

    1.1.2 Second Generation Solar Cells 3

    1.1.3 Third Generation Solar Cells 3

    1.1.4 Importance of Perovskite Performance Modeling 5

  1.2 Previous Solar Cell Research 6

    1.2.1 Non-Perovskite Solar Cells 6

    1.2.2 Perovskite Solar Cells 7

    1.2.3 Modeling and Simulations of Perovskite Solar Cell 8

  1.3 Motivation 10

  1.4 Objectives 10

Chapter 2: Theory 12

  2.1 Solar Cell 12

    2.1.1 p-n Junction Solar Cell Overview 12

    2.1.2 Band Diagram of p-n Junction Solar Cell 13

  2.1.3 Solar Cell Equivalent Circuit Model 15
  2.1.4 Air Mass (AM) 17
  2.1.5 External Quantum Efficiency (EQE) 18
2.2 Perovskite Solar Cell 19
  2.2.1 Device Structures and Working Principle of Perovskite Solar Cells 20
  2.2.2 Band Diagram of Perovskite Solar Cell 22
  2.2.3 “Disordered” Materials 24
2.3 Exciton Generation 27
2.4 Charge Recombination 28
2.5 Coulombic Interaction Model 28
2.6 Kinetic Monte Carlo Method 29
2.7 High Performance Computing 29
  2.7.1 Cluster Computing at SDSU 30
  2.7.2 Tools for Cluster Computing 31
2.8 Characterization 34
  2.8.1 UV-Visible Spectroscopy 34
  2.8.2 X-ray Diffraction (XRD) 35
  2.8.3 Atomic Force Microscopy (AFM) 36
  2.8.4 Scanning Electron Microscopy 39
  2.8.5 Transient Photocurrent Measurement 40

2.8.6 Transient Photovoltage Measurement 41

2.8.7 Profilometry 42

Chapter 3: Procedure 43

3.1 Modeling Procedure 43

3.1.1 Morphology Generation 43

3.1.2 Calculation of Physical Event Rates 48

3.1.3 Kinetic Monte Carlo Simulation 50

3.1.4 J-V Plots Generation and Data Analysis 51

3.1.5 Coulombic Interaction Model 53

3.1.6 Simulation on High Performance Computing 54

3.2 Fabrication Procedure 55

3.2.1 Materials 55

3.2.2 Device Fabrication 56

3.3 Parameter Variations 57

3.3.1 Parameter Variation – Model Simulations 58

3.3.2 Parameter Variation – Cell Fabrication 58

3.4 Film Characterizations 58

3.4.1 UV-Visible Absorption Spectroscopy 58

3.4.2 X-ray Diffraction (XRD) 59

3.4.3 Atomic Force Microscopy (AFM) 60

3.4.4 Scanning Electron Microscope (SEM) 61
3.4.5 Dektak 150 Profilometer 62
3.5 Device Characterization 63
3.5.1 Current Density-Voltage (J-V) Measurement 63
3.5.2 External Quantum Efficiency Measurement (EQE)...64
3.5.3 Transient Photocurrent/Photovoltage Spectroscopy..64
Chapter 4: Results and Discussion...66
4.1 Perovskite Solar Cell Structure Simulation..66
4.2 Variation of Morphological Parameters in Simulation 66
4.2.1 Variation of Capping Layer Coverage..66
4.2.2 Variation of Capping Layer Thickness...72
4.3 Variation of Morphological Parameters in Cell Fabrication...................................76
4.3.1 Variation in PbI_2 Concentration 76
4.3.2 Variation on Spin Coating Speed 82
4.4 Comparison of Simulated and Experimental Results..86
4.4.1 Simulated / Experimental Capping Layer Coverage Comparison.....................87
4.4.2 Simulated / Experimental Capping Layer Thickness Comparison....................89
Chapter 5: Summary and Conclusions...92
5.1 Summary 92
5.2 Conclusions 93

5.3 Future work 94

References 95

LIST OF FIGURES

Figure 1.1. Efficiency evolution of solar cells from 1976 to 2018 2

Figure 1.2 Progress in the efficiency of perovskite solar cells from 2006 to 2018. 5

Figure 2.1. p-n Junction Solar Cell with Depletion Region...13

Figure 2.2. Illuminated p-n Junction Solar Cell Band Diagram 14

Figure 2.3. Solar Cell Equivalent Circuit Model 16

Figure 2.4. J-V and Power Curves of Solar Cell Under Illumination...............................17

Figure 2.5 Different Air Mass on the Earth Relative to Solar Position 18

Figure 2.6. Crystal Structure of Perovskite (ABX_3) 20

Figure 2.7. (a) n-i-p, (b) p-i-n Planar Structure of Perovskite Solar Cell 21

Figure 2.8. Schematic of a Mesoscopic n-i-p Structure of Perovskite Solar Cell 22

Figure 2.9. Energy band diagram of n-i-p perovskite solar cell structure 22

Figure 2.10. Band diagram of PSC (a) Under Short Circuit Condition, (b) Open Circuit Condition...23

Figure 2.11. The potential Distribution at Any Point 24

Figure 2.12. Active PuTTY Session 32

Figure 2.13. Active WinSCP Session 33

Figure 2.14. (a) A pbs script file; (b) MATLAB source implementing parallel processing 34

Figure 2.15. Schematic of Absorbance Spectrophotometer...35

Figure 2.16. X ray Diffraction Patterns From Sample...36

Figure 2.17. (a) Schematic of an Atomic Force Microscope; (b) Force-Distance Curve between Tip and Sample 38

Figure 2.18. Atomic Force Microscope Phase Image Amplitude and Phase Changes at Sample Surface 38

Figure 2.19. Schematic of a Scanning Electron Microscope. 39

Figure 2.20. (a) Schematic of Transient Photocurrent Measurement, (b) Transient Photocurrent Decay....40

Figure 2.21. (a) Schematic of Transient Photovoltage Measurement (b) Transient Photovoltage Decay 41

Figure 2.22. (a) Schematic of a Stylus Profilometer; (b) Stylus Movement in a Stylus Profilometer; (c) Principle of Linear Variable Differential Transducer 42

Figure 3.1. A Typical Model of n-i-p Perovskite Solar Cell With 100% Capping Layer Coverage 44

Figure 3.2. Site Lattice Schematic 45

Figure 3.3. Flow Chart of Morphology Generation and Conduction/Valence Band Distribution 46

Figure 3.4. Ohmic Contacts between Active Layer and Transport Layers....50

Figure 3.5. KMC Simulation and Energy Sites Tracking Flow Chart....51

Figure 3.6. Predicted J-V Characteristic Generation and Data Analysis Flowchart....53

Figure 3.7. Coulombic Interactions of Charge Particles (a) at Site i; (b) at Site j. 54

Figure 3.8. n-i-p Structure of Fabricated Perovskite Solar Cell 55

Figure 3.9. Agilent 8453 UV-Visible Spectrophotometer....59

Figure 3.10. Rigaku Smartlab X-Ray Diffraction Diffractometer....60

Figure 3.11. Agilent SPM 5500 Atomic Force Microscope 61

Figure 3.12. Hitachi S-3400N SEM....62

Figure 3.13. Dektak 150 Profilometer 62

Figure 3.14. Solar Cell J-V Characteristic Measurement 63

Figure 3.15. EQE Measurement Setup. 64

Figure 3.16. Transient Photoconductivity Measurement Set up 65

Figure 4.1. 3D Image and Top View, Simulated Morphology of Perovskite Solar Cells with Different Capping Layer Coverage (a, b) 85%; (c, d) 90%; (e, f) 95%; (g, h) 100%67

Figure 4.2. (a-d) Energy Band Diagram under Thermal Equilibrium; (e-h) Under 0.975 V, 1.025 V, 1.050 V and 1.10 V Forward Bias for Different Capping Layer Coverages (85%, 90%, 95 % and 100%), respectively. 69

Figure 4.3. Simulated Cell Performance vs. Capping Layer Coverage: (a) Predicted J-V Characteristics; (b) TPC Decay; (c) TPV Decay; (d) Number of Recombination Events at J-V MPP....................71

Figure 4.4. Simulated Morphology of Perovskite Solar Cells with Different Capping Layer Thickness (a) 350 nm; (b) 400 nm; (c) 450 nm; (d) 500 nm....................73

Figure 4.5. (a-d) Simulated Cell Performance vs. Capping Layer Thickness: (a) Predicted J-V Characteristics; (b) TPC Decay; (c) TPV Decay; (d) Number of Recombination Events at J-V MPP....................75

Figure 4.6. XRD Spectra of FTO / c-TiO_2 / m-TiO_2; Perovskite Films of Varying PbI_2 Concentration on Top of m-TiO_2....................77

Figure 4.7. AFM and SEM Images of Fabricated Perovskite Films: (a-e) AFM Topography; (f-j) AFM Phase; (k-o) SEM images. Figures (a, f, k) are FTO/compact TiO_2/m-TiO_2; figures (b, g, l), (c, h, m), (d, i, n), and (e, j, o) are Perovskite Films on m-

TiO_2 at PbI_2 concentrations of 62 mg/ml, 262 mg/ml, 462 mg/ml, and 662 mg/ml, respectively 79

Figure 4.8. Measured Solar Cell Performance with Respect to PbI_2 Concentration: (a, b) Current Density-Voltage Characteristics (Forward Scan, Reverse Scan); (c) TPC Decay; (d) TPV Decay. 81

Figure 4.9. (a) UV-vis Absorbance Spectra; (b) EQE Spectra and Integrated Photocurrent Density J_{sc} of Perovskite Solar Cells Prepared with Different PbI_2 Concentrations. 82

Figure 4.10. Measured Solar Cell Performance with Respect to Capping Layer Thickness: (a, b) Current Density-Voltage Characteristics (Forward Scan, Reverse Scan); (c) TPC Decay; (d) TPV Decay. 84

Figure 4.11. (a) UV-vis Absorbance Spectra; (b) EQE Spectra and Integrated Photocurrent Density J_{sc} of Perovskite Solar Cells Prepared with Different Capping Layer Thicknesses. 85

Figure 4.12. Statistics of Efficiency for Perovskite Solar Cell with Optimized PbI_2 Concentration and Capping Layer Thickness 86

Figure 4.13. Simulated / Measured Performance Comparison with Respect to Capping Layer Coverage: (a) Efficiencies; (b) Charge Transport Time; (c) Charge Carrier Recombination Lifetime 89

Figure 4.14. Simulated / Measured Performance Comparison with Respect to Capping Layer Thickness: (a) Efficiencies; (b) Charge Transport Time; (c) Charge Carrier Recombination Lifetime 91

LIST OF TABLES

Table 3.1. Materials used at Different Layers of Perovskite Solar Cells..........................56

Table 4.1. Simulated Device Performance of Perovskite Solar Cells at 85%, 90%, 95%, and 100% Capping Layer Coverage 72

Table 4.2. Simulated Device Performance of Perovskite Solar Cells...............................75

Table 4.3. Photovoltaic Parameters, Charge Transport Time and Charge Carrier Recombination Lifetime for Perovskite Solar Cells Prepared with Different PbI_2 Concentration. 82

Table 4.4. Photovoltaic Parameters, Charge Transport Time and Charge Carrier Recombination Lifetime for Perovskite Solar Cells with Different Capping Layer Thickness. 85

Table 4.5. Compact-TiO_2, mesoporous-TiO_2, and spiro-OMeTAD Layer Thicknesses Used for Studying Capping Layer Coverage and Thickness of Perovskite.......................87

Table 4.6. Perovskite Capping Layer Thickness Parameters..87

Table 4.7. Simulated / Measured Performance Capping Layer Coverage Comparison. ...88

Table 4.8. Simulated / Measured Performance Capping Layer Thickness Comparison ...90

ABSTRACT

A KINETIC MONTE CARLO STUDY OF MESOSCOPIC PEROVSKITE SOLAR CELL PERFORMANCE BEHAVIOR

BEHZAD BAHRAMI

2019

Perovskite solar cells have received considerable attention in recent years due to their low processing cost and high energy conversion efficiency. However, the mechanisms of perovskite solar cell performance are not fully understood. Models based on probabilistic and statistical approaches can be used to simulate, optimize, and predict perovskite solar cell photovoltaic performance, and they can also guide experimental processing and fabrication conditions to achieve higher photovoltaic efficiency. This work developed a 3D model based on the kinetic Monte Carlo (KMC) approach to simulate 3D morphology of perovskite-based solar cells and predict their photovoltaic performance. The model incorporated the physical behavior of perovskite cells with respect to their charge generation, transport, and recombination characteristics. KMC simulation results showed that perovskite films with the pin holes-free and a homogenous perovskite capping layer of 400 nm thickness produced a maximum photovoltaic efficiency of 20.85%, resulting in minimal charge transport time (τ_t) and maximum charge carrier recombination lifetime (τ_r). Photovoltaic performance from the fabricated device has been used to validate this simulation model. This model provides significant conceptual advances in identifying current performance constraints and guiding novel device designs that enhance overall perovskite photovoltaic performance.

Chapter 1: Introduction

1.1 Background

Approximately two thirds of current global energy usage comes from electrical energy generated from fossil fuels. As the global population increases, so does the demand for energy. There are many disadvantages to using fossil fuels to power the world. First, fossil fuels are nonrenewable; at current consumption rates, it is estimated that the known deposits of oil, gas, and coal will run out by 2060 [1]. In addition, fossil fuel consumption poses high risks to the environment. These risks include global warming that is heating the Earth to a degree where many life forms cannot survive, along with increasing levels of air pollution that are harmful to all life. The current rate of global average temperature rise puts approximately half of all plants and animals at risk of extinction [2]. In 2013, the World Health Organization concluded that fossil fuel use contributes to the increased emission of potentially carcinogenic agents into the air [3].

The International Energy Agency (IEA) was created in 1973-1974 to provide policy advice and technological insights into increasing use of renewable energy sources for heating, electrical energy generation, and transportation purposes [4]. Renewable energy is central to the development of a more sustainable, less carbon-intensive global energy system. Furthermore, the use of renewables such as wind power and solar photovoltaics has substantially reduced costs worldwide. The commitment to the implementation of renewables across the globe is depicted by the IEA’s expectation that by 2022, generation of electrical energy from renewable sources will increase by more than 30% [5].

Global use of solar energy is continually increasing. Starting at virtually no usage in 2000, solar energy usage had increased to approximately 50 GW by 2010, and a potential solar power capacity of approximately 305 GW currently exists [6]. This growth is hugely significant, as it offers a way to address crucial climate change issues critically impacting the Earth's environmental health. Compared to nonrenewable resources, the amount of sunlight striking the Earth's surface in eighteen days contains the amount of energy stored in all of the planet's coal, oil, and natural gas reserves [7]. Converting to renewable energy sources such as solar cells is vital to the survival of this planet.

Solar energy can be directly converted to electrical energy with photovoltaic devices without need of turbines or generators. Three generations of solar cell technology have been developed. Figure 1.1 shows the advances in reported conversion efficiency for each generation. Each generation is considered in greater detail in the following sections.

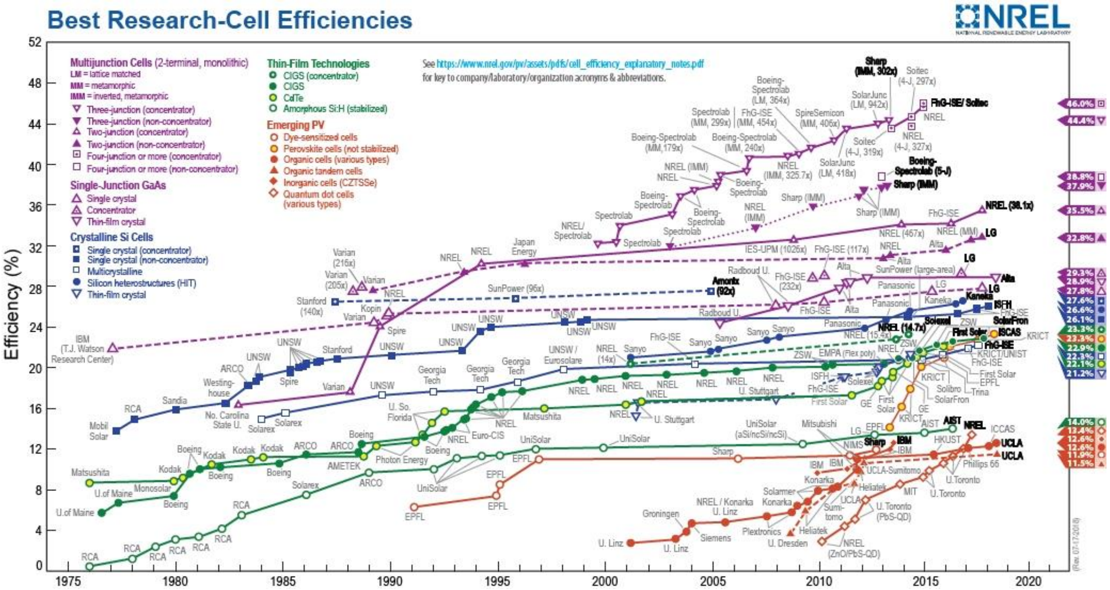

Figure 1.1. Efficiency evolution of solar cells from 1976 to 2018 [8].

1.1.1 First Generation Solar Cells

The first generation solar cells were fabricated with crystalline silicon as the photovoltaic material. At the present time, polycrystalline and crystalline silicon-based solar cells account for the majority of commercially available photovoltaic devices and exhibit typical efficiencies of approximately 20.4% and 25%, respectively [9]. However, these devices are more costly to fabricate, due to i) the increased amount of energy required in the fabrication process; and ii) the need for an abundant amount of 99.99% pure material that can be fabricated into layers of a few hundred microns in thickness [10, 11] .

1.1.2 Second Generation Solar Cells

The second generation of solar cells was developed using thin films of III-V and II-VI compounds such as gallium arsenide (GaAs), as an alternative to crystalline silicon. These semiconductor materials possess higher absorption coefficients than crystalline Si, resulting in increased light absorption within a thinner layer of material [12]. Consequently, their fabrication is technologically simpler and less costly than for the first generation cells. Currently, cadmium telluride (CdTe), copper indium selenide (CIS) and copper indium gallium (di) selenide (CIGS) are the materials commonly used for second generation solar cell production [13]. Expanded use of second generation technology, however, is ultimately limited due to the relative scarcity of the base elements in nature [13].

1.1.3 Third Generation Solar Cells

Recent advances in material science have led to the development of the third generation of solar cells that are increasing of interest. These cells are based on novel organic and inorganic materials and material structures. They include the dye-sensitized solar cell (DSSC), the polymer solar cell, the oligomers solar cell, and the organic/inorganic hybrid perovskite solar cell. In particular, an organic-inorganic hybrid perovskite cell design has generated much interest, as it compares favorably to current silicon-based cell designs in terms of power conversion efficiencies (PCEs), manufacturing cost, and processing effort [14]. The PCEs of these hybrid perovskite cells have increased from 3.8% in 2009 to over 23% for a newly developed n-i-p mesoscopic structure [15-17].

Perovskite compounds have been in use in solar cells since 2009. Initially, they were used as absorbers in DSSC solar cells that achieved PCEs of approximately 3% to 4% [18]. Starting in 2011, they were directly fabricated into solar cells with PCEs of up to 6.5% [19]. By 2015, reported perovskite cell PCEs had significantly increased to over 20% [20]. Within the last three years, the reported PCEs have increased less dramatically, from approximately 22.1% in 2016 [21] to approximately 23.2% in 2018 [17]. Figure 1.2 shows the progression in reported PCE (%) during this period [14]. As a result of this demonstrated growth, perovskite-based technologies appear to be most promising for future solar cell development. With the potential of achieving even higher efficiencies and much lower fabrication costs, perovskite solar cells have become more attractive commercially, to the extent that allowed start-up companies to promise delivery of devices by 2017 [22-24].

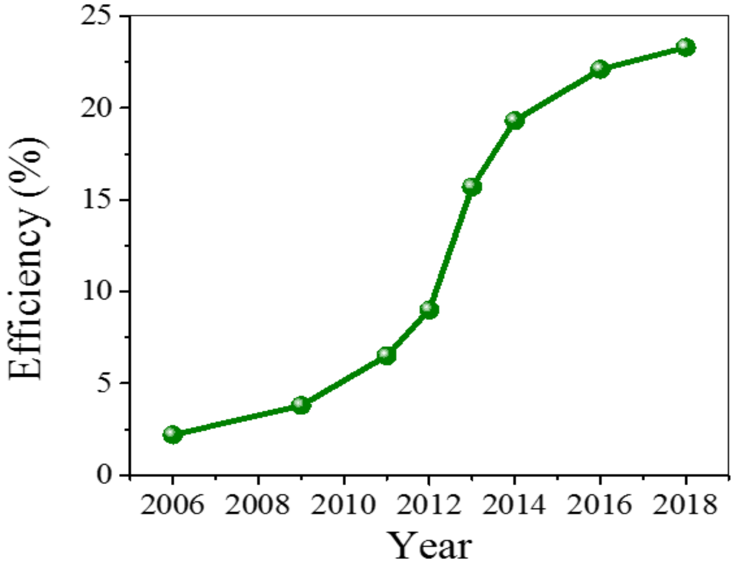

Figure 1.2 Progress in the efficiency of perovskite solar cells from 2006 to 2018 [14].

1.1.4 Importance of Perovskite Performance Modeling

Because development of perovskite-based solar cells has occurred so recently, knowledge of the fundamental mechanisms enabling their performance is not well understood [25, 26]. This knowledge can be acquired through rigorous computer-based modeling of the device physics and performance characteristics represented by the photoconversion efficiency and charge carrier dynamics. With this information, devices of greater efficiency can be fabricated at significantly reduced fabrication costs.

Existing modeling and analysis tools such as COMSOL and Simulink have been used to facilitate research into improvements of solar cell technology, AC/DC electrical characteristics and battery cell dynamics that achieve savings in fabrication cost and required material usage [27, 28]. Additional software has been developed to model fundamental solar cell physics; however, this software is limited to modeling behavior in 1 or 2 spatial dimensions [29]. More realistic models for perovskite solar cells need to simulate morphology and carrier dynamics in three spatial dimensions; the typical approach based on closed-form solutions of partial differential equations is not sufficient for this task [30]. Alternatively, a statistical/probabilistic approach to modeling can be considered, such as a Monte Carlo simulation. In particular, a Kinetic Monte Carlo (KMC) simulation has demonstrated great potential in temporal modeling of 3D morphology, charge transport mechanisms, and charged particle generation/recombination as realistic natural phenomena [31, 32].

1.2 Previous Solar Cell Research

1.2.1 Non-Perovskite Solar Cells

The first p-n junction was fabricated from crystalline silicon by Russel Ohl in Bell laboratories in 1946 [33]. This was followed by the development of a first-generation solar cell at Bell laboratories by Chapin *et al*. in 1954, with an estimated PCE of approximately 6% [34]. In 1972, Gereth *et al*. improved this efficiency to 12.4 % by increasing the purity of crystalline silicon [35]. To reduce the material and processing cost, in 1976, Carlson *et al*. fabricated a solar cell from amorphous silicon with an estimated PCE of 2.4%; this cell was among the first to use a layer of silicon that was only a few microns in thickness [36]. Silicon-based mono-crystal and multi-crystal solar cells with PCEs of approximately 24.4% and 19.8%, respectively, were fabricated by Zhao *et al.* in 1998 [37]. Several studies have been conducted into the development of thin-film solar cells based on III-V or II-VI compound structures, primarily CdTe, CIGS, and CdS, in an attempt to reduce processing cost and required material usage [38-40].

In 1986, Tang reported the bi-layer heterojunction organic solar cell with a PCE of approximately 1% [41]. This type of organic solar cell has low PCE. In 1995, Yu *et al.*

investigated a bulk heterojunction polymer solar cell design with the intent of improving the PCE [42]. In 2005, Yang *et al.* achieved a PCE of around 4.4% in bulk heterojunction polymer solar cells [43]. In 2012, He *et al.* reported the PCE of 9.2% for an inverted bulk heterojunction polymer solar cell structure [44]. In 2013, You *et al.* fabricated a-based polymer tandem solar cell with a PCE of approximately 10.6% [45].

A novel dye-sensitized solar cell (DSSC) with an estimated efficiency of approximately 8% [46] was fabricated by Brian O' Regan and Michael Gratzel in 1991 using i) a mesoporous semiconductor which increases light absorption by increasing the amount of dye adsorbed; and ii) an electrolyte containing iodide/triiodide redox species. Perovskite solar cells (PSCs) are derived from the DSSC concept. Their history is briefly summarized in the next section.

1.2.2 Perovskite Solar Cells

In 2009, the first PSC with a PCE of 3.8% was fabricated by Kojima *et al.* [18, 47-49]. They replaced the dyes with a perovskite ($CH_3NH_3PbI_3$) absorber compound. The perovskite has several advantages over the standard DSSC dye, including i) excellent optical properties which can be tuned by managing chemical compositions; ii) broader absorption; iii) low exciton binding energy; iv) ambipolar charge transport v) long charge carrier lifetime; and vi) long electron−hole diffusion lengths [50-53]. However, his proposed structure was unstable because the perovskite compound dissolved in the liquid electrolyte. To address this issue, Kim *et al.* in 2012 fabricated the first perovskite ($CH_3NH_3PbI_3$) based solid-state mesoscopic solar cell to achieve a PCE of 9.7%, using mesoporous-TiO_2 (m-TiO_2) as the electron transport layer (ETL) and spiro-MeOTAD as the hole transport layer (HTL) [54].

In 2013, Burschka *et al.* applied the sequential deposition method to control perovskite ($CH_3NH_3PbI_3$) morphology and fabricated a solid-state mesoscopic with a reported PCE of approximately 15% [55]. In 2015, Ahn *et al.* fabricated similar structure devices with a maximum PCE of approximately 19.7%. They achieved an average PCE of approximately 18.3% when a Lewis based adduct of PbI_2 was used [56].

In 2015, Yang *et al.* fabricated formamidinium lead iodide ($FAPbI_3$) based PSCs with a maximum PCE of more than 20% [20]. In 2017, they achieved a PCE of approximately 22.1%, by decreasing the concentration of deep level defects through addition of iodide ions into the organic cation solution [57]. In 2018, Jeon *et al.* sensitized a fluorine-terminated hole-transporting material with a fine-tuned energy level with the mixed perovskite $(FAPbI_3)_{0.95}$ $(MAPbBr_3)_{0.05}$ to achieve a PCE of 23.2% [17].

1.2.3 Modeling and Simulations of Perovskite Solar Cell

Analytical models based on partial differential equations are typically used to conduct 1D and 2D simulations of planar perovskite cell structures due to their simplicity and efficiency [58-63]. A general solar cell simulation program, AMPS-1D, has been used to show the effects of thickness, recombination and defect density on perovskite cell photovoltaic performance [64]. Sun *et al.* assumed a constant electric field in perovskite solar cell to obtain an analytical solution using general equations [59]. Their model parameters were obtained through fits to experimentally measured J-V curves as opposed to a predictive model. Incorporation of interfacial and bulk recombination effects, [58, 60, 65] in perovskite solar cells have been investigated with 1D-numerical models. Sherkar *et al.* used a 1D device model based on the standard drift-diffusion model to study the correlation of trap assisted recombination at grain boundaries and interfaces with defect ions in perovskite solar cells [66]; as with Sun's work, the resulting model parameters were derived through fits to experimentally measured data. Wang *et al.* reported the interrelationship between the trap distributions of mesoporous-structured perovskite solar cells and carrier recombination dynamics by using 1D multiple trapping models [67]. The 2D planar configuration was developed to study the effect of carrier diffusion length on the performance of perovskite solar cells [61, 62].

As mentioned earlier, these 1D and 2D models based on closed-form solutions of partial differential equations cannot adequately simulate actual 3D morphology of perovskite based solar cell structures. To address this issue, Monte Carlo (MC) simulation using a more probabilistic/statistical approach is essential [63]. In addition, a time-dependent variant of MC simulation, known as kinetic MC (KMC), has the capability to transition between various states by calculating all transition rates and randomly selecting one transition for execution [68, 69]. Fortunately, microscopic models based on KMC simulation have been developed to describe charge carrier behavior (e.g., charge carrier generation, dissociation, recombination, and transport) in organic solar cells [70-72]. The KMC method has helped generate important findings in experimental data by closely simulating charge transfer [71], carrier mobility, geminate recombination [72] and bimolecular recombination [70]. This method has been considered a useful tool for studying, understanding, and improving the performance of organic solar cells [73-77] and silicon solar cells [78, 79].

As perovskite solar cell technology is still a new field, the fundamental device mechanisms are still not well understood [25, 26]. In 2013, Yadari *et al.* used MC simulations to study the magnetic properties of the double perovskite compound nano

Sr_2VMoO_6, [80]. In 2018, Gagliardi *et al.* reported the role of the mesoporous-TiO_2 interface between the perovskite and the electron transport layer (ETL) [30]. They used the MC-based “metropolis” algorithm to make the 3D morphology of device in the mesoscopic case and a 1D model in the planar case. They found that the planar structures were less tolerant of ion vacancy migration than the mesoscopic structure.

In summary, the hybrid lead halide perovskite is a promising material in photovoltaic technology. The PCE of perovskite solar cells has drastically increased from 3.8% to 22.7% during the past ten years [81-88]. Sensitivity studies show that perovskites are potentially the most environmentally sustainable photovoltaic technology [89]. Since the KMC method is based on possible transition rates, this modeling method produces a more realistic 3D model by considering physical processes (e.g., charge generation, charge transport, and charge recombination) in perovskite solar cells. However, no research has been reported on modeling and simulating a complete perovskite solar cell using the KMC approach. A substantial need exists to develop a realistic model to simulate 3D perovskite solar cells in order to study morphological variations and their effects on device performances.

1.3 Motivation

There is a need for an improved 3D model to simulate spatial and temporal perovskite solar cell characteristics and performance that addresses how variation in morphological parameters impacts the ultimate device performance.

1.4 Objectives

The objectives of this work were to develop a 3D model that can reflect the variation of morphological parameters on the performance parameters of the device and to validate simulation results against the corresponding experimental measurements. To achieve these objectives, the following tasks were performed:

1. Develop morphology of perovskite solar cell using general Monte Carlo simulation
2. Compare the performance parameters of simulated devices with fabricated cells possessing similar physical characteristics
3. Simulate various perovskite solar cell models with:
    a. Variation of the percentage coverage of capping layer
    b. Variation of capping layer thickness
4. Fabricate various perovskite solar cells with:
    a. Variation of PbI_2 concentration
    b. Variation of capping layer spin coating speed
5. Compare and correlate simulation and experimental results by:
    a. Relating coverage of capping layer to PbI_2 concentration
    b. Relating capping layer thickness to spin coating speed

Chapter 2: Theory

2.1 Solar Cell

A solar cell is fundamentally a semiconductor device that converts solar energy directly into electrical energy. The energy conversion occurs when a photon is absorbed by a semiconducting material. When a beam of light falls on a semiconductor device, the bounded electrons are excited to higher energy states due to the absorbed photon energy, forming electron-hole pairs. These are separated and allowed to collect at two different terminals, ultimately generating an electric current.

In general, photovoltaic (PV) cells are not 100% efficient due to reflection of a portion of light striking on the cell. At low energy levels (in the infrared portion of the spectrum) this decreases the charge separation efficiency. At higher energy levels (in or beyond the ultraviolet) this increases generation of heat, which leads to thermal losses.

2.1.1 p-n Junction Solar Cell Overview

A typical solar cell is based on a p-n junction diode, which is formed when p-type and n-type materials are physically joined together (Figure 2.1). The first p-n junctions were formed from crystalline Si doped with Group III elements (e.g., Boron) to form the hole-rich p-type material and Group V elements (e.g., Phosphorous) to form the electron-rich n-type material. The holes diffuse into the n-type material while the electrons diffuse into the p-type material, forming a depletion or space charge region near the junction boundary [90]; a quasi-neutral region (QNR) on each side of the junction beyond the boundary contains the majority of free charge carriers equal to the density of material doping for that side [91]. Therefore, a built-in electric field (E) is generated in the space charge region due to formation of positive ions in the n-type material and negative ions in the p-type material, which ultimately prevents further electron/hole diffusion. The depletion region thus plays an important role in dissociating electron-hole pairs and forcing photogenerated carriers towards their respective electrodes.

When the energy of incident photons illuminating a semiconductor is greater than its band gap energy, electrons are excited from the valence band to the conduction band, while holes are left behind in the valence band. These free charge carriers are transported to their respective electrodes by drift due to the built-in electric field in the space charge region, and by diffusion in the QNR. Both drift and diffusion currents are formed; however, drift through the space charge region occurs more quickly than diffusion through the QNR. This has led to solar cell designs where the space charge region is as wide as possible while the QNR is as thin as possible. This design is implemented by the p-i-n solar cell [91].

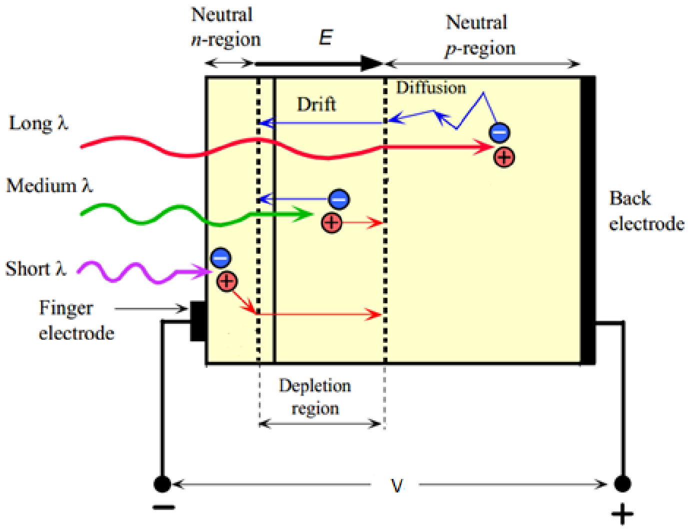

Figure 2.1. p-n Junction Solar Cell with Depletion Region [92].

2.1.2 Band Diagram of p-n Junction Solar Cell

Figure 2.2 shows a band diagram of a p-n junction solar cell under illumination with the conduction band (E_C), valence band (E_V) and band gap (E_g). An absorbed photon excites an electron from E_V to E_C to generate free electrons in the n-type material and free holes in the p-type material. In undoped semiconductors, the Fermi level (E_F) is generally in the middle of the band gap between E_C and E_V; in n-type semiconductors, it increases towards E_C (termed as E_{FC}), while in p-type semiconductors it decreases towards E_V (termed as E_{FV}). There is an offset potential between E_{FC} and E_{FV}, which is an output open-circuit voltage (V_{oc}).

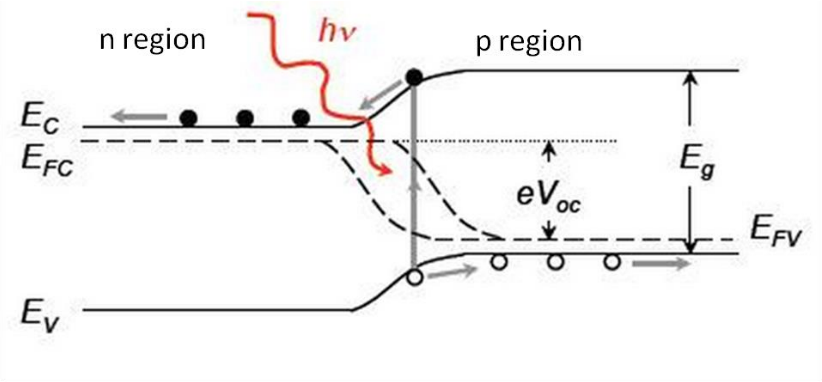

Figure 2.2. Illuminated p-n Junction Solar Cell Band Diagram [93]

The movement of charge carriers depends on the carrier velocity (v) and electric field (F). Therefore, the mobility (μ) is calculated by [94]:

$$\mu = \frac{<v>}{F} \tag{2.1}$$

The electron drift current (J_n), and hole drift current (J_p) densities are related to the mobility of electrons (μ_n) and holes (μ_p) as [91]:

$$J_n = qn\mu_n F \tag{2.2}$$

$$J_p = qp\mu_p F$$

where q, n, and p are the elementary charge constant, electron and hole free carrier density, respectively and F is the space charge region electric field. The charge carrier diffusion co-efficient (D_z) along the direction of the electric field (e.g., z-direction) is defined as [94]:

$$D_z = \frac{<z^2> - <z>^2}{2t} \tag{2.3}$$

where z is the location of the charge carrier in the QNR or in regions where the electric field strength is zero [91], and t is the time spent by the carrier in each location.

2.1.3 Solar Cell Equivalent Circuit Model

An equivalent circuit model for a generic solar cell is shown in Figure 2.3, which consists of a p-n junction diode in parallel with a photocurrent (J_{ph}) source and series (R_s) and shunt resistances (R_{sh}), respectively. A potential difference (V) applied as a load to the circuit causes a small current to flow in the diode (J_d) which is in the opposite direction of J_{ph}. This reverse current equals the dark current (J_{dark}) of the diode [91], which is given by:

$$J_{dark}(V) = J_o(e^{\frac{qV}{mKT}} - 1) \tag{2.4}$$

where J_o and m are the dark saturation current density and diode ideality factor, respectively, and K, T, and V are Boltzmann's constant, the absolute temperature and the applied potential difference, respectively.

The net current density (J) through the load is calculated by:

$$J(V) = J_{dark}\,(\mathrm{V}) - J_{PH} \tag{2.5}$$

Substituting equation (2.4) into (2.5) yields

$$J(V) = J_0(e^{\frac{qV}{mkT}} - 1) - J_{ph} \tag{2.6}$$

When the load resistance is zero, the current density through the solar cell is the short circuit current density (J_{sc}), which is obtained by setting V=0 in equation (2.6):

$$J = J_{sc} = -J_{ph} \tag{2.7}$$

When the net current density is zero, the voltage across the load is the open circuit voltage, which is at its maximum value. This can be determined by substituting J=0 in equation (2.6):

$$V_{OC} = \frac{mKT}{q}\ln\left(\frac{J_{ph}}{J_0} + 1\right), \tag{2.8}$$

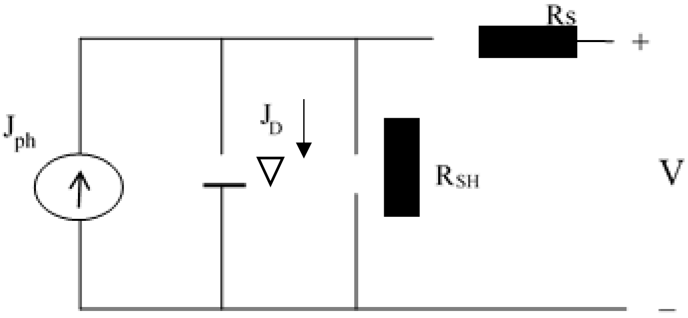

Figure 2.3. Solar Cell Equivalent Circuit Model

J-V and power curves of a solar cell under illumination are shown in Figure 2.4 . The fill factor (FF) of a solar cell depends on the transport of electron and hole carriers, recombination losses, and ohmic contributions of the electrode and the contact. The fill factor is defined as

$$FF = \frac{P_{max}}{J_{SC}V_{OC}} \tag{2.9}$$

where P_{max} is the maximum power point, which is given by

$$P_{max} = J_M V_{M,} \tag{2.10}$$

The efficiency of the solar cell is defined as the ratio of maximum power delivered to the incident light power (P_s) under a standard illumination condition and is defined by

$$\eta = \frac{P_{max}}{P_s} \tag{2.11}$$

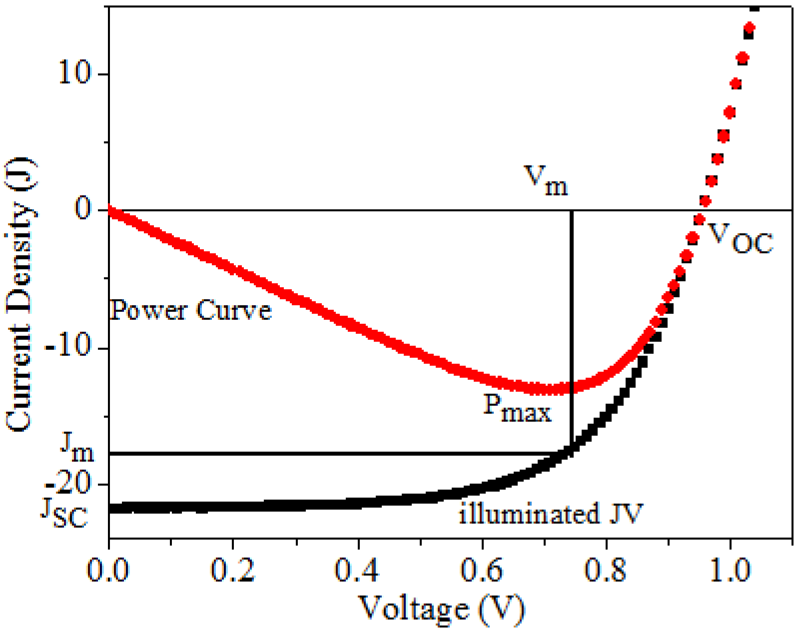

Figure 2.4. J-V and Power Curves of Solar Cell Under Illumination [95]

2.1.4 Air Mass (AM)

The air mass (AM) is defined as the path length of light through the Earth's atmosphere relative to the shortest vertical path at the solar zenith. It depends on the solar position and is defined as

$$AM = \frac{1}{\cos\theta} \qquad (2.12)$$

where θ is the angle between the solar zenith position and the current solar position (Figure 2.5). Due to variation in solar position throughout the day, the AM value can also change. A typical AM value is 1.5, which corresponds to a θ of approximately 48.2°. Standard test conditions for solar cell research use this AM value with an incident power density of 100mW/cm^2 and an ambient air temperature of 25° C [96].

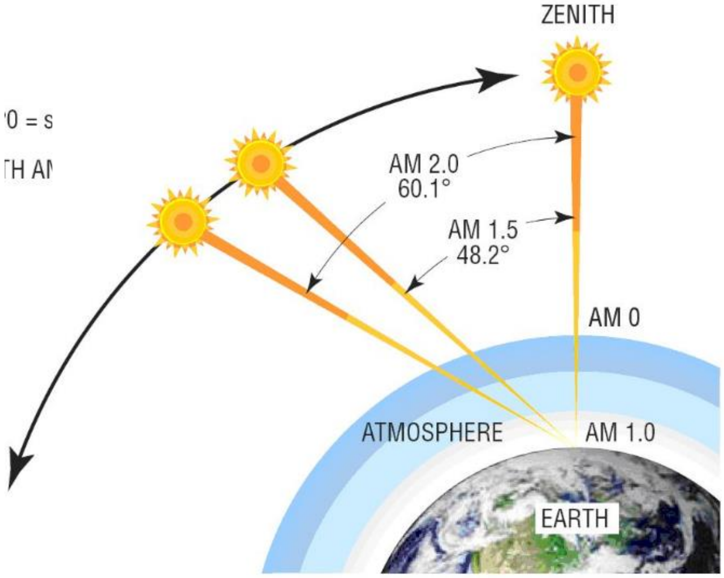

Figure 2.5 Different Air Mass on the Earth Relative to Solar Position [97]

2.1.5 External Quantum Efficiency (EQE)

The ability of a solar cell to convert absorbed light energy into an electrical current is represented by the cell’s external quantum efficiency (EQE), which is quantitatively defined as the ratio of the number of charge carriers collected at the electrodes (n_e) to the number of incident photons (n_{ph}) at a given wavelength:

$$EQE(\lambda) = \frac{n_e(\lambda)}{n_{ph}(\lambda)} \tag{2.13}$$

The EQE is most affected by external photon losses and reflection [98].

The solar cell short circuit current density J_{sc} is a function of its EQE and is determined by

$$J_{SC} = \int_{\lambda_1}^{\lambda_2} e \cdot \Phi_{AM1.5}(\lambda) \cdot EQE(\lambda)\ d\lambda \tag{2.14}$$

where e is the electronic charge, $\Phi_{AM1.5}(\lambda)$ and EQE(λ) are, respectively, the photon flux density and external quantum efficiency at a wavelength λ in the incident solar spectrum at AM 1.5, and λ_2 is the solar cell's cut off absorption wavelength.

2.2 Perovskite Solar Cell

In 1839, Gustav Rose first identified a perovskite crystalline structure in the mineral calcium titanate ($CaTiO_3$); he named the structure in honor of the Russian mineralogist Aleksevich von Perovski [99, 100]. Since then, numerous natural compounds have been identified as possessing a perovskite or related crystalline structure, and more recently, perovskite compounds have been synthesized. As a result, "perovskite" has become an umbrella term to generally indicate any compound with that general structure.

A typical perovskite crystalline structure is represented by ABX_3, where A and B represent cations and X is the anion to which they bond. Figure 1.6 shows an example of the general structure.

Organic-inorganic halide perovskites are a special class of materials formed from an organic cation such as the compound $CH_3NH_3^+$ (MA^+) at A sites, an inorganic cation such as elemental lead (Pb^{2+}) at B sites, and a halide anion such as iodide (I^-) at X sites. This class of perovskite compounds has attracted significant interest for use in solar cell design; during the past several years [82, 83, 101], the power conversion efficiency (PCE) of cells fabricated with these compounds has drastically increased from 3.8% to 23.3%. This is due to their highly desirable properties such as high absorption coefficients, tunable optical band gaps, long range carrier diffusion lengths (100 - 1000 nm), small exciton binding energies, and ambipolar charge transport [102, 103].

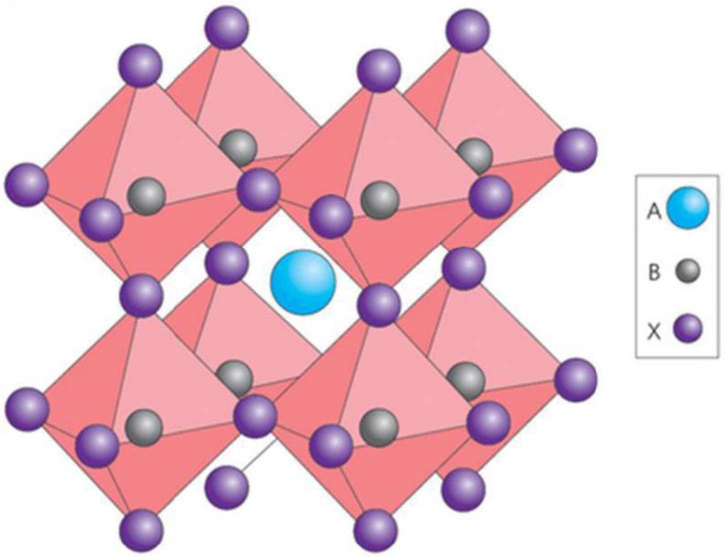

Figure 2.6. Crystal Structure of Perovskite (ABX_3) [47]

2.2.1 Device Structures and Working Principle of Perovskite Solar Cells

Perovsikite-based solar cells (PSCs) can be fabricated in an “n-i-p” or an inverted “p-i-n” structure, as shown in Figure 2.7(a) and (b). The more commonly used “n-i-p” structure is fabricated with a stack consisting of an electron transport layer (ETL) material at the bottom, an absorber layer and a hole transport layer (HTL) material at the top; the “p-i-n” stack is fabricated in the reverse order. Either stack can be bonded on top of a glass/FTO or glass/ITO substrate that has an attached silver electrode. The ETL/HTL in an n-i-p device (or in a p-i-n device) can be fabricated with a planar structure (as shown in Figure 2.7(a) and (b)) or a mesoscopic structure. For the purposes of this work, further consideration is given only to mesoscopic n-i-p device (as shown in Figure 2.8) theory and operation.

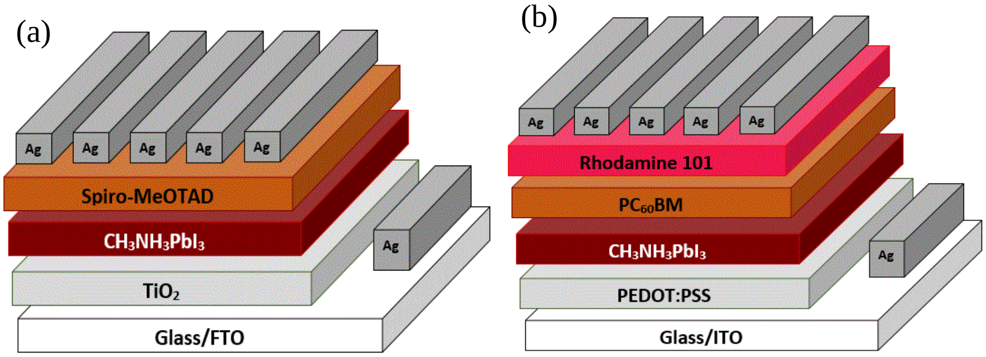

Figure 2.7. (a) n-i-p, (b) p-i-n Planar Structure of Perovskite Solar Cell

Mesoscopic n-i-p perovskite crystals absorb photons, which results in exciton creation. However, the low exciton binding energy can result in dissociation into electrons and holes at room temperature [104]. The electrons are transported to the ETL (TiO_2) and subsequently transferred to the external circuit through the cell electrode. The holes remaining in the crystal are transferred to the HTL (Spiro-OMeTAD) and then ultimately out of the cell through the electrode. Figure 1.8 shows both processes.

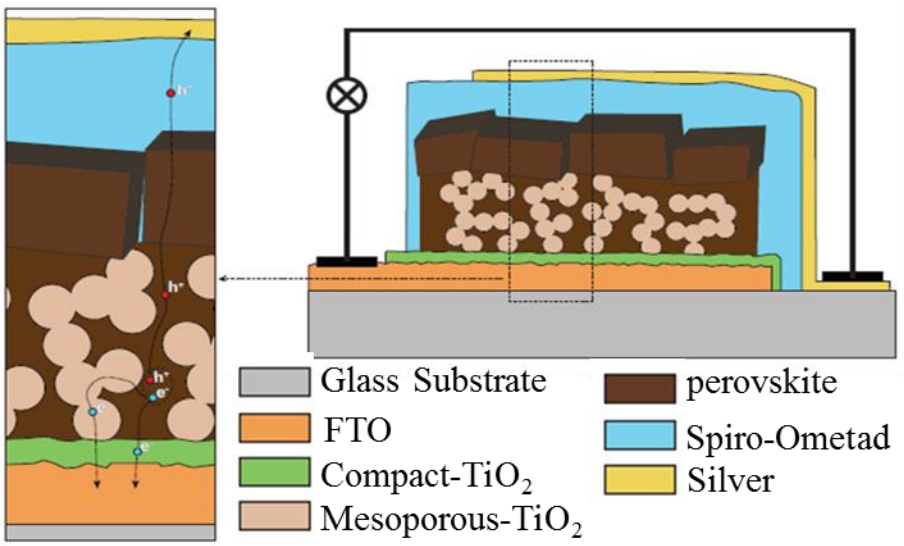

Figure 2.8. Schematic of a Mesoscopic n-i-p Structure of Perovskite Solar Cell [105]

Figure 2.9 shows the energy band diagram of an n-i-p perovskite solar cell. The separated electrons are transported to the FTO electrode from the TiO_2 conduction band. Holes are transported to the electrode from the Spiro-OMeTAD valence band.

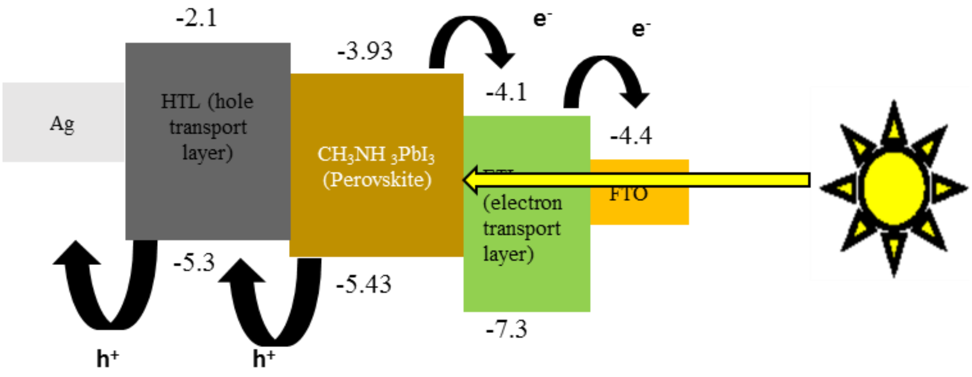

Figure 2.9. Energy band diagram of n-i-p perovskite solar cell structure

2.2.2 Band Diagram of Perovskite Solar Cell

Two junctions will form in a PSC when the perovskite and carrier transport layers come into contact. One forms at the ETL/perovskite interface, while the other forms at the perovskite/HTL interface. These junctions play important roles establishing the mechanism of carrier transport from the photoactive layer to the respective electrodes. The Fermi level of the HTL, absorber layer and ETL are at the same level, E_{F_0} , when a PSC is not illuminated and in a short circuit state (Figure 2.10 (a)). An intrinsic voltage (V_{bi}) is created due to the difference between the HTL and ETL work functions (ϕ_{HTL}, ϕ_{ETL}). qV_{bi} is the offset between the conduction band (CB) and valence band (VB) energy levels [106]. In the case of an open circuit state (Figure 2.10 (b)), the Fermi levels of the HTL and ETL are split to E_{F_p} and E_{F_n} , respectively. The open circuit voltage (V_{oc}) is the difference between the split Fermi levels and is due to i) application of a forward bias; and ii) the photocurrent generated by illumination of the cell surface. V_{oc} is the maximum voltage across the solar cell terminals when the net current through the device is zero. Application of the forward bias induces a weak electric field in the absorber layer, which causes the initial band bending to flatten. It also decreases the CB and VB offsets.

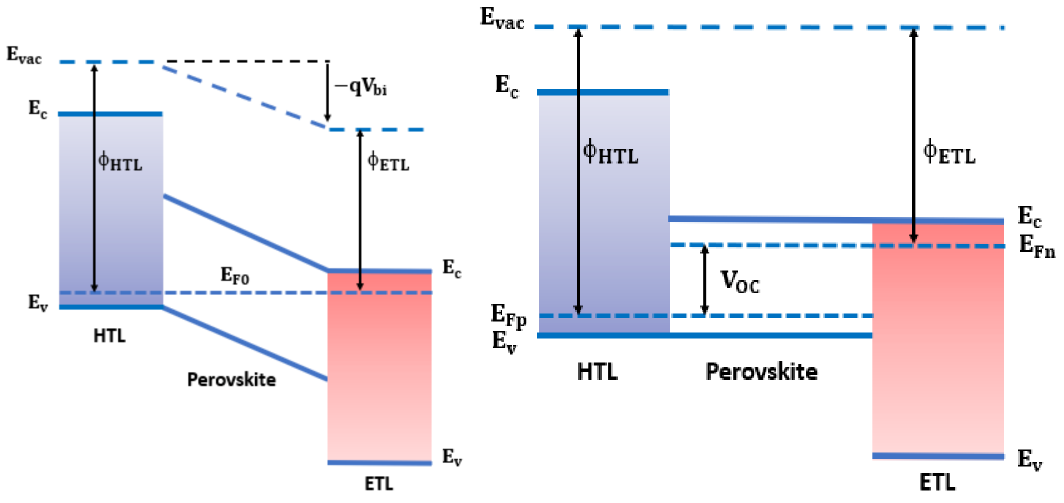

Figure 2.10. Band diagram of PSC (a) Under Short Circuit Condition, (b) Open Circuit Condition [107]

The potential distribution across the active layer can be simply modeled as a linear function of the distance within the layer [59], with V_A as an applied bias and V_{bi} as the intrinsic voltage. For the purposes of this thesis, this basic model is used. Applying geometric analysis to Figure 2.11, it can be shown that $\frac{V_{bi}-V_A}{L} = \frac{\psi(z)}{L-z}$. Consequently, the potential distribution energy $\psi(z)$ with respect to the z-axis can be stated as

$$\Psi(z) = (V_{bi} - V_A) - \frac{V_{bi} - V_A}{L} z \tag{2.15}$$

where z and L are, respectively, the location within the active layer and the thickness of the active layer, respectively.

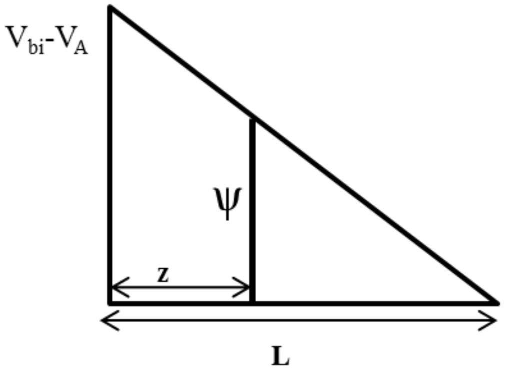

Figure 2.11. The potential Distribution at Any Point [108]

2.2.3 "Disordered" Materials

A material is considered "disordered" if there is no long-range order in atomic arrangement and/or translation symmetry [109]. Energy disorder also be present in these materials and results from the structural disorder [110]. This characteristic behavior allows for fabrication of low-cost devices that are based on novel design concepts. In fact, during the last 30 years, research has been directed towards the use of disordered semiconductor materials for applications ranging from thin film transistors to photovoltaic solar cells.

However, it has not been definitively established what constitutes a disordered material, as comparisons to other materials are typically made with respect to crystal properties. In particular [109]:

- Crystalline structures in practice do not exhibit infinite long-range order due to surface defects and/or doping.
- Disordered semiconductor materials exhibit varying degrees of short-range and medium-range order in their atomic arrangement, without having translation symmetry.

For the remainder of this thesis, consideration is given to the modeling and performance characterization perovskite solar cells fabricated from methylammonium lead iodide ($MAPbI_3$). This compound exhibits both structural and energy disorder [111-113]. Modeling of the density of states (DOS) in disordered semiconductors is typically performed assuming a normal (Gaussian) distribution [113-115]. Additional details relating to this modeling are provided in the next section.

2.2.3.1 Gaussian Distribution Modeling of Disordered Semiconductor Materials

In 1993, Bässler *et al*. first described use of the Gaussian distribution to model charge transport in a disordered semiconducting material [116]. The standard deviation of the DOS represents the energy disorder in the material. The hopping rate of charge particles varies from location to location in disordered materials due to changes in energy level. A Gaussian density of states distribution can be used to define the energy of charge transport sites in disordered systems.

The Gaussian distribution model is given as:

$$g(\varepsilon) = \frac{N}{\sigma\sqrt{2\pi}} \exp\left(-\frac{\varepsilon^2}{2\sigma^2} \right) \tag{2.16}$$

where N is the density of states within given device geometry, and ε and σ are, respectively, the mean energy levels of the conduction band minimum (CBM) or valence band maximum (VBM) and the deviation from the mean energy level, respectively.

2.2.3.2 Charge Hopping

There are two main charge transport models: multiple trapping and hopping in disordered materials [117, 118]. The multiple trapping model transport occurs through extended states, but the transport process is impeded due to multiple trapping and detrapping events in the localized states [117]. At this time, it is unclear whether the multiple trapping model can effectively be used [117, 119, 120]. One reason may be that the particular structure of disordered materials does not allow for extended states. For this kind of materials, carrier jumps between localized states through tunneling and/or thermal activation appears to be the preferred charge transfer mechanism; this mechanism might be much better understood through use of the hopping model [117]. The rate of carrier hopping depends on the energy difference between the localized states and the spatial distance between them [117, 118].

Miller Abraham's theory defines the charge transport rate (R_{ch}) based on the hopping model for a disordered semiconductor material as [121]:

$$\begin{aligned} R_{ch} &= w_{0ch} \exp\left(-2\gamma r_{ij}\right) \begin{cases} \exp\left(-\dfrac{E_j - E_i}{kT} \right) & : E_j > E_i \\ 1 & : E_j \le E_i \end{cases} \\ w_{0ch} &= \frac{6KT\mu_{ch}}{el^2} \exp(2\gamma l) \end{aligned} \tag{2.17}$$

where W_{0ch} is the charge hopping pre-factor; γ is the inverse localization radius typically assumed to be 2 nm^{-1}, as the average localization size is considered to be 0.5 nm [122]; E_i and E_j indicate the energy of the site for given charged particles at sites of i and j; r_{ij} and μ_{ch} are the distance between the two sites of interest and the mobility of a charged particle, respectively; and *l* is the average charge transfer distance, typically assumed to be 0.64 nm [123].

Ma *et al.* reported that the charge density of the CBM and the VBM are localized in nanoscale with the size of a few nanometers, because of the random orientation of the organic molecule CH_3NH_3 in $CH_3NH_3PbI_3$ [122]. Doping the TiO_2 layer underneath the perovskite causes narrowing of the depletion region at the interface, thus improving charge carrier tunneling which facilitates efficient charge transport via the high-resistance TiO_2 layer [124-127].

2.3 Exciton Generation

Excitons are generated when photons with energy larger than the semiconductor band gap are absorbed. The generation of excitons is related to the incident photon flux and is known as the exciton generation rate (G_x), defined as [128]:

$$G_x = \int_{\lambda_1}^{\lambda_2} \int_{0}^{L} (1 - R(\lambda)) \times \varphi_s(\lambda) \times \exp(-\alpha(\lambda)x) \times \alpha(\lambda)\, d\lambda dx \tag{2.18}$$

where $R(\lambda)$ and $\phi_s(\lambda)$ are the surface reflectance of the solar cell and the surface photon flux density, respectively, λ_1 and λ_2 define the absorption wavelength range of the active material, L is the thickness of the active layer, and $\alpha(\lambda)$ is the absorption coefficient at that wavelength and x is the depth inside the active layer.

2.4 Charge Recombination

Electrons and holes can recombine before their respective electrodes within the cell collect them. The recombination rate (R_{CR}) is expressed by [129]:

$$R_{CR} = w_{CR}\, exp(-2\gamma\, r_{ij}) \tag{2.19}$$

where w_{CR} and γ are the charge recombination rate constant and inverse localization radius, respectively. As mentioned in the section 2.2.3.2, γ is typically assumed to be 2 nm^{-1}, and r_{ij} is a distance between two sites of interest.

2.5 Coulombic Interaction Model

The Coulombic potential energy is the potential energy due to an electrostatic force between two charges separated by a given distance [130]:

$$E = \frac{q_1 q_2}{4\pi\varepsilon_r \varepsilon_0 r_{12}} \tag{2.20}$$

where q_1 and q_2 are point charges at sites 1 and 2 separated by the distance $r_{1,2}$. ε_r and ε_0 are, respectively, the relative and absolute permittivity, which for the ($CH_3NH_3PbI_3$) perovskite solar cell are 24.1 and 8.85×10^{-14} F/cm [131]. According to the equation (2.20), this energy becomes weaker as the distance between the two charges increases. It means that there is a limit distance only as the charges confirm electrostatic effect during this distance. This distance called cut-off radius (r_c) where the thermal energy can overcome the coulombic energy. Therefore, the cut off radius for a perovskite ($CH_3NH_3PbI_3$) solar cell is around 3 nm and can be determined by solving

$$\frac{q^2}{4\pi\varepsilon_r\, \varepsilon_0 r_c} = kT \cong 0.025 \tag{2.21}$$

for r_c as:

$$r_c = \frac{q^2}{4\pi\varepsilon_r\varepsilon_0 kT} \tag{2.22}$$

With several charges present, the interactions between them result in variation of the overall potential energy at a localized site.

2.6 Kinetic Monte Carlo Method

Simulation modeling is a powerful tool for studying and predicting device performance under different conditions. More realistic models for perovskite solar cells need to simulate morphology and carrier dynamics in three spatial dimensions; the typical approach based on closed-form solutions of partial differential equations is not sufficient for this task [30]. Alternatively, a statistical/probabilistic approach to modeling can be considered, such as a Monte Carlo simulation. In particular, KMC simulation has demonstrated great potential in temporal modeling of 3D morphology, charge transport mechanisms, and charged particle generation/recombination as realistic natural phenomena [31]. Simulations using this type of model require greater computational efficiency due to the more complex nature of the model. This demand could be satisfied by executing the model calculations on high performance systems in parallel computing architecture.

2.7 High Performance Computing

A high-performance computer system (HPC) is comprised of multiple networked computers that are centrally organized by through special software. When the computers are physically close together, the HPC is referred to as a cluster [132]. A cluster can contain many individual computer “nodes” with each node supporting one or more processors. Simulations executed on a cluster can run for extended periods of time, such as several days or weeks, depending on the complexity of the simulation model. In addition, required processing tasks within the model can be efficiently distributed to multiple processors through use of parallel computing techniques.

2.7.1 Cluster Computing at SDSU

South Dakota State University (SDSU) currently supports a 70+ node Linux-based cluster system, located in the Data Center on the first floor of the Morrill Admin Building [133]. “blackjack” is a host within this cluster that is used for job submission. Three other hosts within the cluster, “flapjack”, “kojack”, and “bigjack” are used as an interactive test node, a virtual network computing (VNC) visualization node, and a network file server node, respectively.

The cluster has the following specifications [108]:

1. 71 IBM IdataPlex, IBM DX350 M3 nodes
2. Each node: 12 cores consisting of two hex-core Intel Xeon X5670 (Westmere), 2.93 GHz
3. Each node supports 48 GB or 96 GB RAM capacity
4. Infiniband-high speed, low latency interconnect to each node, as well as gigabit Ethernet
5. Nine nodes support high-performance graphics with dual Nvidia Tesla 2090 series GPU hardware on each node
6. SLES 11.3 operating system
7. SAN block storage for flexible deployment of large partitions to head node

2.7.2 Tools for Cluster Computing

2.7.2.1 PuTTY

The PuTTY software [134] was used to establish a secure shell (SSH) connection to the “blackjack” host, submit processing jobs to the cluster and remotely execute various operations within the cluster. Figure 2.12 shows an active PuTTY session executed on a Microsoft Windows-based client computer. The following set of Linux commands were used in a typical PuTTY session to perform basic cluster-related processing tasks:

1. ***cd*****:** change directory or folder command.
2. ***qsub*****:** submit a job to the cluster
3. ***qstat*****:** present the status of the job
4. ***showq*****:** display the current status of executing jobs in the queue
5. ***qdel <id>****:* delete the running job with ID number <id>
6. ***checkjob <id>****:* checks the status of the given job with ID number <id>

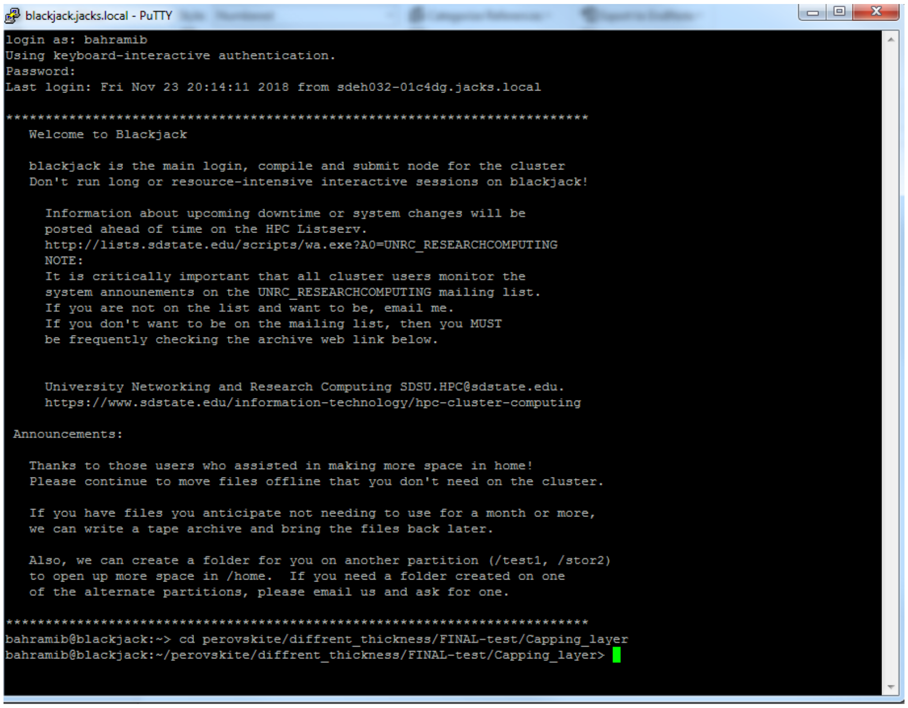

```
login as: bahramib
Using keyboard-interactive authentication.
Password:
Last login: Fri Nov 23 20:14:11 2018 from sdeh032-01c4dg.jacks.local

**************************************************************************
   Welcome to Blackjack

   blackjack is the main login, compile and submit node for the cluster
   Don't run long or resource-intensive interactive sessions on blackjack!

     Information about upcoming downtime or system changes will be
     posted ahead of time on the HPC Listserv.
     http://lists.sdstate.edu/scripts/wa.exe?A0=UNRC_RESEARCHCOMPUTING
     NOTE:
     It is critically important that all cluster users monitor the
     system announements on the UNRC_RESEARCHCOMPUTING mailing list.
     If you are not on the list and want to be, email me.
     If you don't want to be on the mailing list, then you MUST
     be frequently checking the archive web link below.


     University Networking and Research Computing SDSU.HPC@sdstate.edu.
     https://www.sdstate.edu/information-technology/hpc-cluster-computing

 Announcements:

   Thanks to those users who assisted in making more space in home!
   Please continue to move files offline that you don't need on the cluster.

   If you have files you anticipate not needing to use for a month or more,
   we can write a tape archive and bring the files back later.

   Also, we can create a folder for you on another partition (/test1, /stor2)
   to open up more space in /home.  If you need a folder created on one
   of the alternate partitions, please email us and ask for one.

**************************************************************************
bahramib@blackjack:~> cd perovskite/diffrent_thickness/FINAL-test/Capping_layer
bahramib@blackjack:~/perovskite/diffrent_thickness/FINAL-test/Capping_layer>
```

Figure 2.12. Active PuTTY Session

2.7.2.2 WinSCP

The WinSCP software [135] was used to perform secure file transfers between a local computer and remote hosts within the cluster. Figure 2.13 shows an example WinSCP session. The left and right panes in the main WinSCP application window display the contents in a user’s local computer “home” folder and the same user’s contents in their home folder on the “blackjack” host. WinSCP supports two-way file/data transfer between a local host and the cluster.

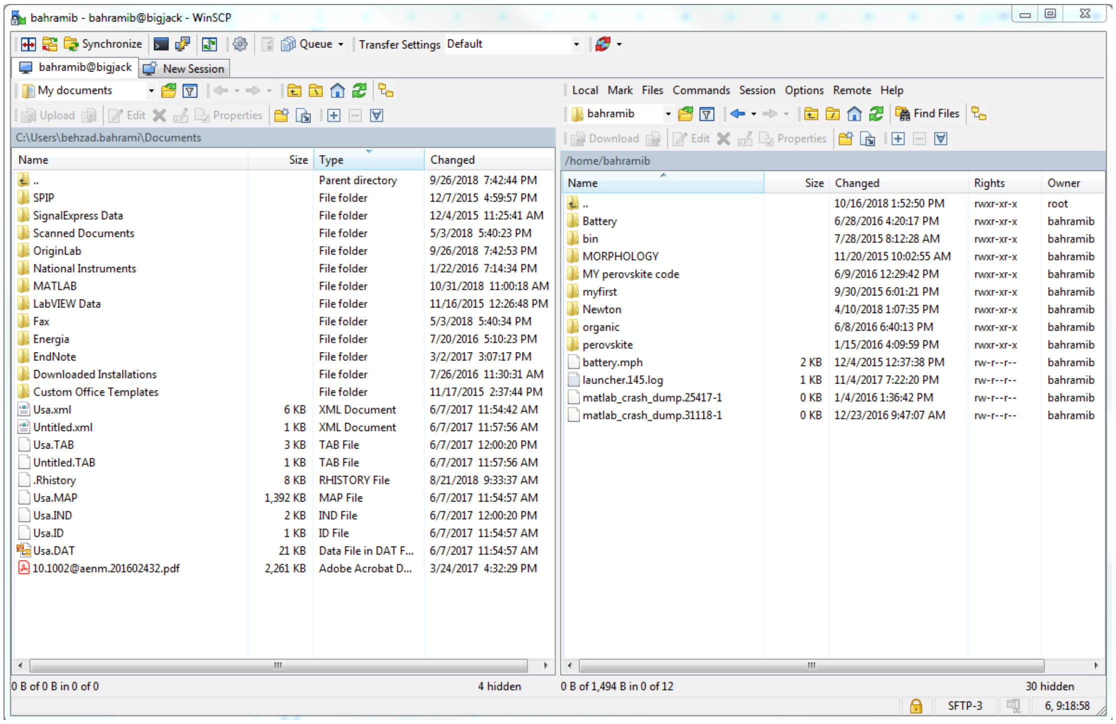

C:\Users\behzad.bahrami\Documents

Name	Size	Type	Changed
..		Parent directory	9/26/2018 7:42:44 PM
SPIP		File folder	12/7/2015 4:59:57 PM
SignalExpress Data		File folder	12/4/2015 11:25:41 AM
Scanned Documents		File folder	5/3/2018 5:40:23 PM
OriginLab		File folder	9/26/2018 7:42:53 PM
National Instruments		File folder	1/22/2016 7:14:34 PM
MATLAB		File folder	10/31/2018 11:00:18 AM
LabVIEW Data		File folder	11/16/2015 12:26:48 PM
Fax		File folder	5/3/2018 5:40:34 PM
Energia		File folder	7/20/2016 5:10:23 PM
EndNote		File folder	3/2/2017 3:07:17 PM
Downloaded Installations		File folder	7/26/2016 11:30:31 AM
Custom Office Templates		File folder	11/17/2015 2:37:44 PM
Usa.xml	6 KB	XML Document	6/7/2017 11:54:42 AM
Untitled.xml	1 KB	XML Document	6/7/2017 11:57:56 AM
Usa.TAB	3 KB	TAB File	6/7/2017 12:00:20 PM
Untitled.TAB	1 KB	TAB File	6/7/2017 11:57:56 AM
.Rhistory	8 KB	RHISTORY File	8/21/2018 9:33:37 AM
Usa.MAP	1,392 KB	MAP File	6/7/2017 11:54:57 AM
Usa.IND	2 KB	IND File	6/7/2017 12:00:20 PM
Usa.ID	1 KB	ID File	6/7/2017 11:54:57 AM
Usa.DAT	21 KB	Data File in DAT F...	6/7/2017 11:54:57 AM
10.1002@aenm.201602432.pdf	2,261 KB	Adobe Acrobat D...	3/24/2017 4:32:29 PM

0 B of 0 B in 0 of 0 4 hidden

/home/bahramib

Name	Size	Changed	Rights	Owner
..		10/16/2018 1:52:50 PM	rwxr-xr-x	root
Battery		6/28/2016 4:20:17 PM	rwxr-xr-x	bahramib
bin		7/28/2015 8:12:28 AM	rwxr-xr-x	bahramib
MORPHOLOGY		11/20/2015 10:02:55 AM	rwxr-xr-x	bahramib
MY perovskite code		6/9/2016 12:29:42 PM	rwxr-xr-x	bahramib
myfirst		9/30/2015 6:01:21 PM	rwxr-xr-x	bahramib
Newton		4/10/2018 1:07:35 PM	rwxr-xr-x	bahramib
organic		6/8/2016 6:40:13 PM	rwxr-xr-x	bahramib
perovskite		1/15/2016 4:09:59 PM	rwxr-xr-x	bahramib
battery.mph	2 KB	12/4/2015 12:37:38 PM	rw-r--r--	bahramib
launcher.145.log	1 KB	11/4/2017 7:22:20 PM	rw-r--r--	bahramib
matlab_crash_dump.25417-1	0 KB	1/4/2016 1:36:42 PM	rw-r--r--	bahramib
matlab_crash_dump.31118-1	0 KB	12/23/2016 9:47:07 AM	rw-r--r--	bahramib

0 B of 1,494 B in 0 of 12 30 hidden

Figure 2.13. Active WinSCP Session

2.7.2.3 Pbs Script

Pbs script is used to submit a processing job. A configuration file is used to specify parameters setting up the simulation environment in which the scripts execute. These parameters include the walltime (HH:MM:SS) required to run a simulation, the number of nodes and corresponding processors per node needed to run a simulation, and a requirement module specifying the code/application used to run a simulation, as shown in Figure 2.14(a). This figure illustrates an example processing environment set up to simulate perovskite solar cell performance under different applied bias voltages. The simulation environment was set as follows:

- The maximum walltime (168 hours for Matlab module)
- 1 node and 12 processors are allocated to execute the job

- MATLAB is to execute the simulation, and the required source filename is new_ill1.m which is required for the simulation (as shown in Figure 2.14(b))

The ***matlabpool*** function shown in Figure 2.14(b) was used to process 12 bias voltage inputs in parallel during each iteration, with each processor working on a single voltage input.

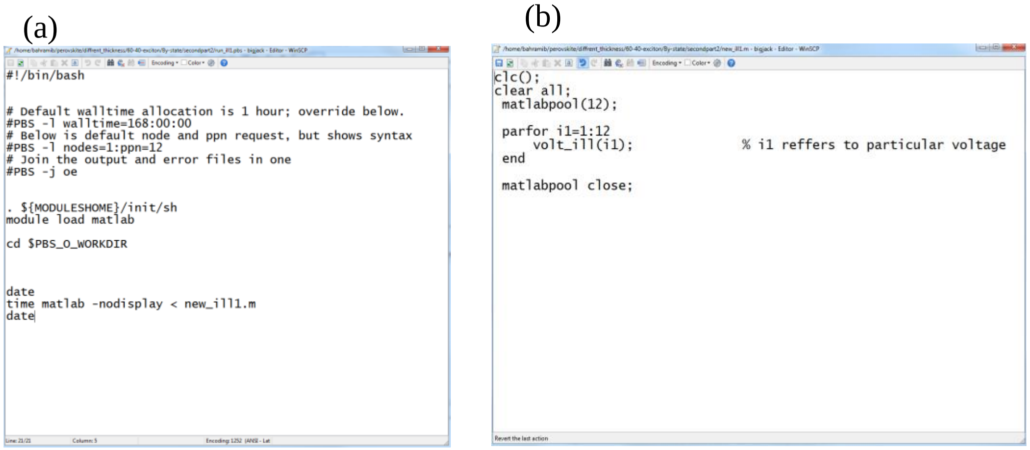

(a)

```
#!/bin/bash


# Default walltime allocation is 1 hour; override below.
#PBS -l walltime=168:00:00
# Below is default node and ppn request, but shows syntax
#PBS -l nodes=1:ppn=12
# Join the output and error files in one
#PBS -j oe


. ${MODULESHOME}/init/sh
module load matlab

cd $PBS_O_WORKDIR



date
time matlab -nodisplay < new_ill1.m
date
```

(b)

```
clc();
clear all;
 matlabpool(12);

 parfor i1=1:12
     volt_ill(i1);                 % i1 reffers to particular voltage
 end

 matlabpool close;
```

Figure 2.14. (a) A pbs script file; (b) MATLAB source implementing parallel processing

2.8 Characterization

2.8.1 UV-Visible Spectroscopy

Absorption of visible or ultraviolet (UV) light causes excitation of electrons from lower energy or ground states to empty higher energy or excited states; examples include excitation of electrons from HOMO to LUMO states or from valence band to conduction band states. Ultraviolet-visible (UV-Vis) spectroscopy can be used to measure the absorbance of UV or visible light by a sample at one or more desired wavelengths within the spectrum. The light source contains a tungsten lamp and deuterium lamp to generate light in the visible and near UV spectrum. To transmit a selectable narrow band of light wavelengths, the light from the source passes through a monochromator, as shown in Figure 2.15.

The Beer-Lambert law, the principle behind UV-Vis spectroscopy, is used to estimate the absorbance of the sample as follows:

$$\mathrm{A}(\lambda) = -\log(T(\lambda)) = -\log_{10}\left(\frac{I}{I_0}\right) = \varepsilon bc \tag{2.23}$$

where T(λ) is the transmittance at a particular wavelength of light, I and I_0 are the intensity of transmitted light and incident light, respectively, ε is the molar absorptivity, b is the path length of the sample and c is the concentration of the compound in solution [136].

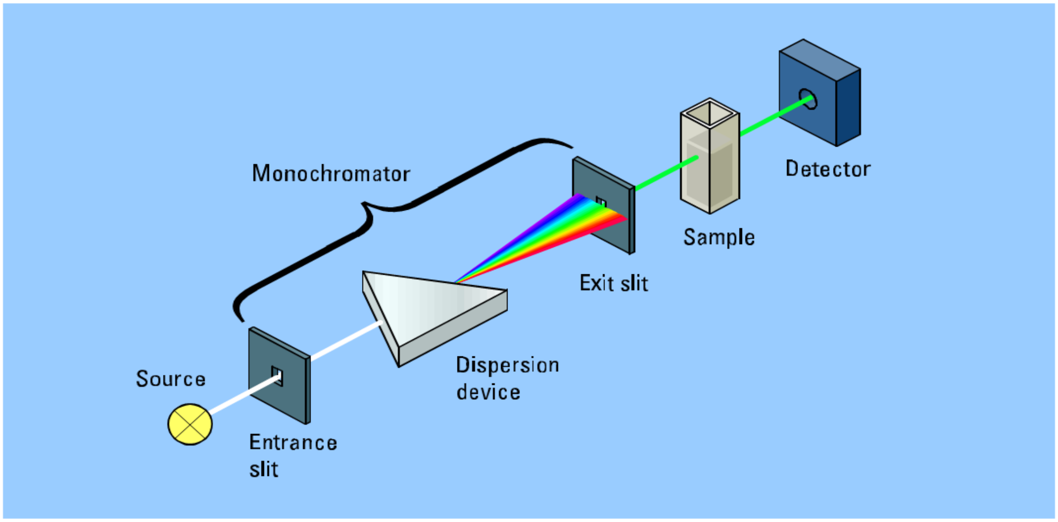

Figure 2.15. Schematic of Absorbance Spectrophotometer [137]

2.8.2 X-ray Diffraction (XRD)

X-ray diffraction (XRD) measurement is used to identify and quantitatively analyze crystalline phases of different materials. When an incident beam of X-rays strikes a sample, the X-rays scatter from the sample with varying intensities due to diffraction. The diffraction pattern can be defined by Bragg's law:

$$2d\sin\theta = n\lambda \tag{2.24}$$

where θ is the angle of the incident and reflected beams, d and λ are the spacing between the crystal layer and the X-ray wavelength, respectively, and n is an integer. Figure 2.16 illustrates diffraction from a sample with incident x-rays.

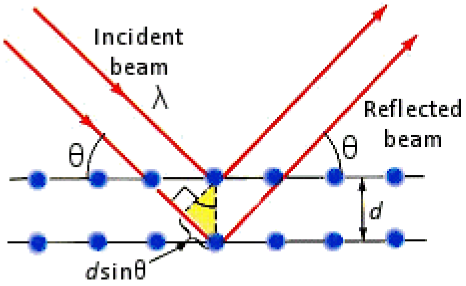

Figure 2.16. X ray Diffraction Patterns From Sample [138]

2.8.3 Atomic Force Microscopy (AFM)

The scanning tunneling microscope (STM), a form of the scanning probe microscope (SPM), was developed by Binnig and Rohrer in 1980 [139]. One limitation of the STM as originally designed is that the material to be analyzed should either be a conductor or semiconductor. To address this issue, the first atomic force microscope (AFM) was invented in 1986; it is currently the most common type of SPM [139].

Figure 2.17 (a) shows a schematic of an AFM. The instrument consists of a laser leveler, 4-quadrant photodiode, and a cantilever having a sharp tip at its apex. A diode laser beam from a laser leveler is incident at the tip of the cantilever and is reflected to the position photodiode. The cantilever deflects due to Van der Waals, electrostatic or coulombic, capillary and adhesive forces between the sample surface and the tip. This deflection leads to displacement of the laser reflected beam position on the photodiode which translates to feedback electronics. The feedback signal is then converted to a topographic image.

AFM imaging works in three modes, depending on the interaction force between the cantilever tip and the sample: contact mode, tapping mode and non-contact mode. Figure 2.17 (b) illustrates the force versus distance curve between the tip and the sample. When the tip is very far from the sample, there is no interaction between them. As the tip moves closer to the sample, a weak attractive force forms; in this state the AFM images in its non-contact mode. When the tip is very near the sample surface, repulsive van der Waals forces are dominant, and the net electrical force is positive; in this state the AFM images in its contact mode. The typical AFM imaging mode is the tapping mode and occurs when the tip moves closer to or further away from the sample to generate oscillating repulsive and attractive forces. Tapping mode imaging has the benefit of providing high resolution topographic and phase imagery.

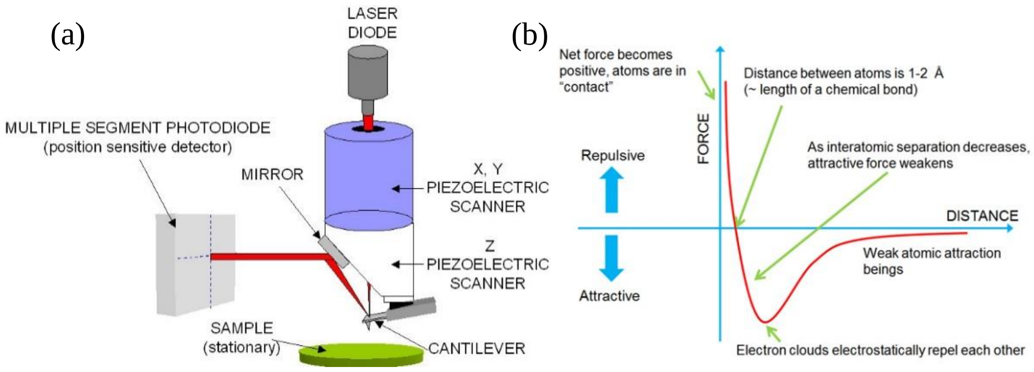

Figure 2.17. (a) Schematic of an Atomic Force Microscope [140]; (b) Force-Distance Curve between Tip and Sample [141]

AFM phase imaging in tapping mode [142] can be used to characterize a sample surface's mechanical properties of elasticity, adhesion, and friction. The AFM cantilever tip oscillates at a given amplitude (A_0) when it is far from the sample surface. As the tip comes nearer to the surface, the oscillation amplitude reduces, and oscillation phase shifts occur (Figure 2.18); these changes are related to the mechanical properties at the sample surface. The phase images are generated from the recorded oscillation amplitudes and phase angles.

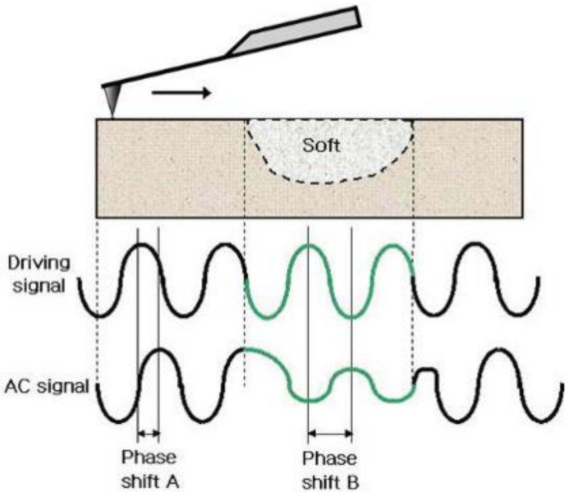

Figure 2.18. Atomic Force Microscope Phase Image Amplitude and Phase Changes at Sample Surface [143]

2.8.4 Scanning Electron Microscopy

The scanning electron microscope (SEM) is typically used to determine the morphology at a sample's surface. Figure 2.19 shows the basic schematic for an SEM device. An electron gun generates a beam that is focused by the "condenser" lens. A scanning coil in front of the condenser lens produces a magnetic field that deflects the electron beam. The "objective" lens in front of the scanning coil focuses the beam onto the sample. When the focused beam strikes the sample, X-rays and three types of electrons (i.e., primary back-scattered, secondary, and Auger) are emitted. A detector measures the secondary electrons emitted from the sample, thus generating an image of the sample surface.

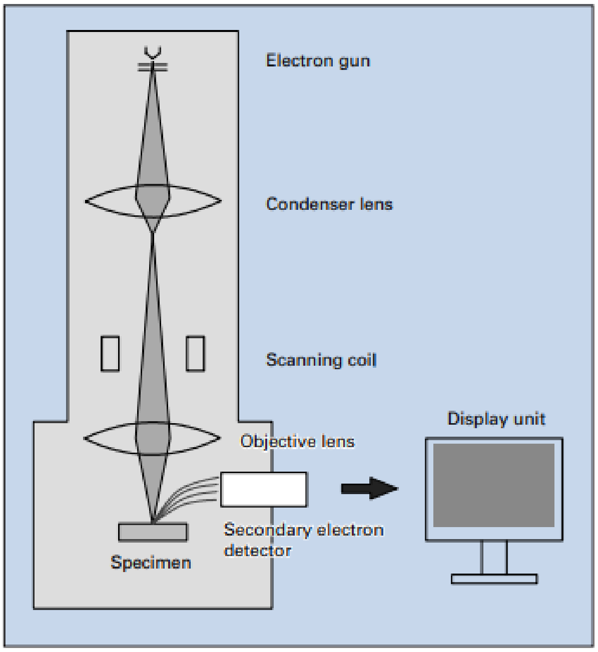

Figure 2.19. Schematic of a Scanning Electron Microscope [144].

2.8.5 Transient Photocurrent Measurement

Transient photocurrent (TPC) measurements are used to characterize the charge carrier transport time (τ_r). Nanosecond laser pulse can be used to measure transient photocurrent in a perovskite solar cell, as shown in Figure 2.20(a). To obtain these measurements, the device is kept in a short-circuited state by applying a small resistance (on the order of 50Ω) across the device terminals. The time (τ_t) represents the time required for the carriers to reach the device electrodes. The TPC decay pattern is exponential in nature, as shown in Figure 2.20(b), and is given by [95, 145]:

$$I(t) = I_0 e^{-\frac{t}{\tau_t}} \tag{2.25}$$

where t is the time, and I_0 is the initial current at t=0.

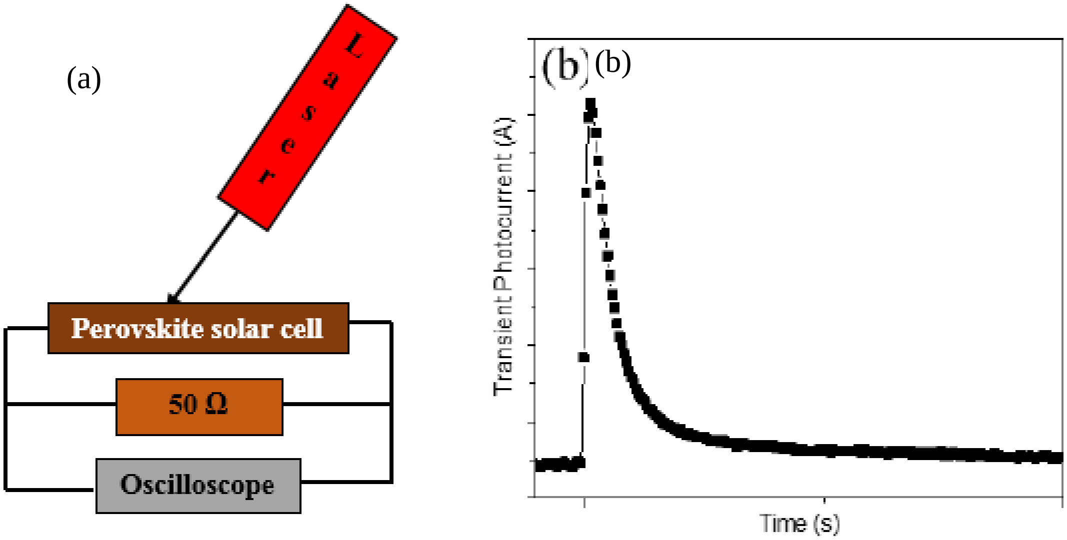

Figure 2.20. (a) Schematic of Transient Photocurrent Measurement, (b) Transient Photocurrent Decay[146]

2.8.6 Transient Photovoltage Measurement

Transient photovoltage (TPV) measurements are used to characterize the charge carrier recombination lifetime (τ_r). Nanosecond laser pulse is applied to a perovskite solar cell exposed to constant illumination, resulting in a steady state. The device is kept in the open-circuited condition by applying a large resistance (on the order of 1 MΩ) across the device terminals, as shown in Figure 2.21(a). The change in the voltage is exponential, as shown in Figure 2.21 (b), and is given by [95]:

$$\Delta V(t) = \Delta V_0 e^{-\frac{t}{\tau_r}} \tag{2.26}$$

where t is the time, and ΔV_0 is the transient photovoltage at t=0.

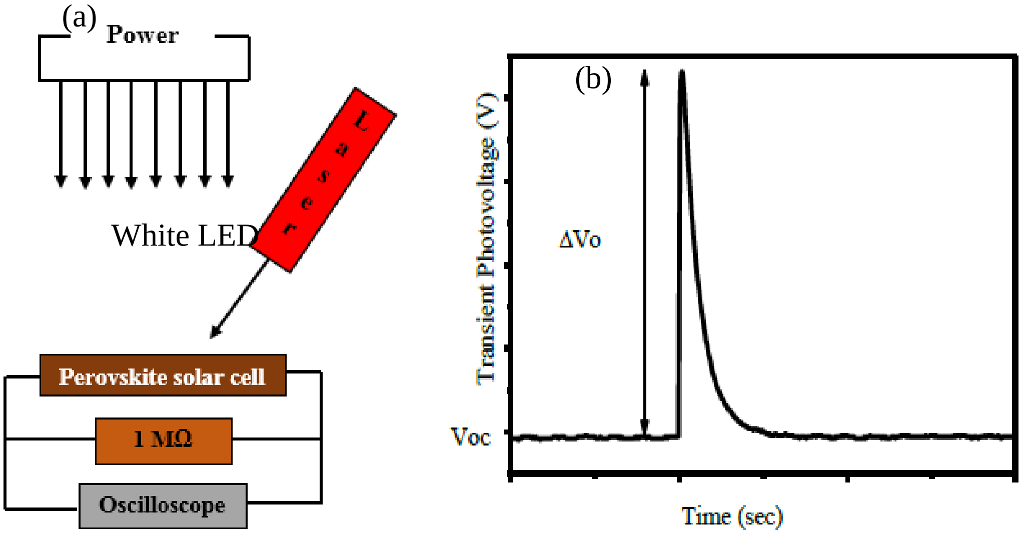

Figure 2.21. (a) Schematic of Transient Photovoltage Measurement (b) Transient Photovoltage Decay [95]

2.8.7 Profilometry

Profilometry is a technique used to quantify surface topographic data. This technique leads to information about general surface morphology, step heights and surface roughness. There are two different types of profilometers used for these measurements i) the contact or stylus profilometer; and ii) the non-contact profilometer, which uses a focused light beam to scan the surface [147].

Stylus profilometers use a diamond stylus which is physically in contact with a sample. All stylus profilometers contain a gear box, the stylus, a pickup, a datum, a data acquisition system, a linear variable differential transformer (LVDT) transducer, and a control unit (Figure 2.22 (a)). The pickup, which includes the transducer and stylus, is driven by the gear box, which moves the stylus across the sample at a constant speed with a given contact force, as shown in Figure 2.22 (b). The z-axis displacement of the stylus is sensed by the LVDT as an electrical signal during sample scanning, as shown in Figure 2.22 (c), which is recorded by the data acquisition system [148].

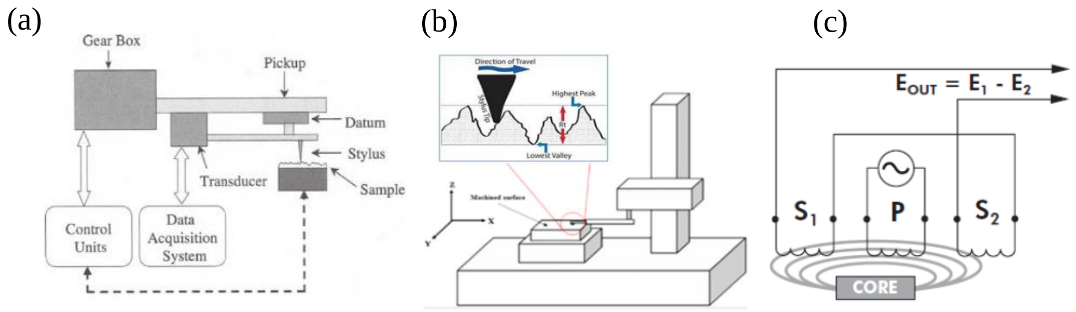

Figure 2.22. (a) Schematic of a Stylus Profilometer [148]; (b) Stylus Movement in a Stylus Profilometer [147]; (c) Principle of Linear Variable Differential Transducer [149]

Chapter 3: Procedure

3.1 Modeling Procedure

3.1.1 Morphology Generation

A 3D matrix with dimensions of 2000×2000×900 was used to generate the morphology of an n-i-p perovskite solar cell as shown in Figure 3.1. The electron transport layer (ETL) and hole transport layer (HTL) were assumed to be compact TiO_2 (c-TiO_2) and spiro-OMeTAD, respectively. The ETL and HTL were oriented parallel to the x-y plane, initially located between $0 < z \leq 50$ and $700 < z \leq 900$, respectively, with thicknesses of 50 nm and 200 nm. The initial active layer was assumed to consist of a 250 nm thick layer of m-TiO_2 and perovskite located at $50 < z \leq 300$, and a 400 nm thick capping layer composed of perovskite and spiro-OMeTAD located at $300 < z \leq 700$. +1 and -1, representing the perovskite and m-TiO_2 spins, were randomly distributed throughout the perovskite/m-TiO_2 layer. Similarly, +2 and -2, representing the perovskite and spiro-OMeTAD spins, were randomly distributed throughout the perovskite/spiro-OMeTAD layer. Morphological parameters such as the capping coverage and thickness were altered by changing i) the perovskite/spiro-OMeTAD ratio (by varying the number of assigned sites in the volume of the device); and ii) the z-dimensions of the device layer.

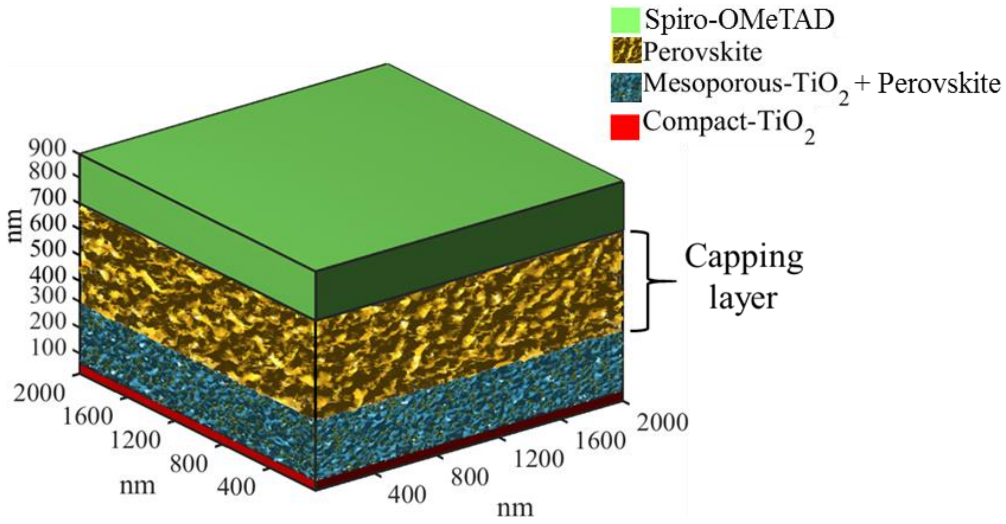

Figure 3.1. A Typical Model of n-i-p Perovskite Solar Cell With 100% Capping Layer Coverage

The Metropolis Monte Carlo algorithm [30, 74, 150] and the Kawasaki spin exchange model were used to simulating the relaxation of excited states to lower energy levels at equilibrium. The Ising Hamiltonian energy function was calculated at a given site as follows [150]:

$$\in_i = -\frac{J}{2}\sum_j (\delta_{Si,Sj} - 1) \tag{3.1}$$

$\delta_{si,sj}$ is the Kronecker delta function, with values of 1 when $s_i=s_j$, and 0 when $s_i \neq s_j$. s_i and s_j are the spins at neighboring sites *i* and *j*, respectively (where *j* is the first or second nearest neighbor site to *i*). *J* is the interaction energy, which was chosen to be *kT* by assuming the system to be in thermal equilibrium.

The Hamiltonian function at site *i* decreases as the donor or acceptor domains increase [150]. To account for the longer distance, the energy contribution of the second nearest neighbor site was weighted by a factor of $1/\sqrt{2}$. Figure 3.2 shows the square lattice with nearest neighbor sites ‘j’ and ‘k’ in relation to the site of interest ‘i’, assuming physical lattice dimensions of 1nm × 1 nm.

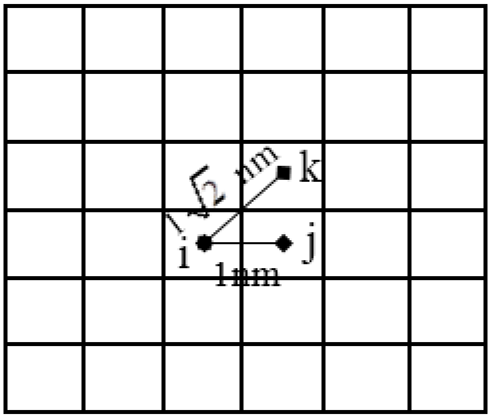

Figure 3.2. Site Lattice Schematic [108]

According to the Kawasaki spin-exchange model, if the total energy in the new configuration is suppressed, a swap is implemented with a probability of 1; otherwise, the probability of swap between two sites *i* and *j* (i.e., *i* and *j* switch) was calculated as [150]:

$$P(\Delta \in)=\frac{\exp\left(-\frac{\Delta \in}{kT}\right)}{1+\exp\left(-\frac{\Delta \in}{kT}\right)} \tag{3.2}$$

where $P(\Delta\varepsilon)$ is the probability of swap, $\Delta\varepsilon = \epsilon_j - \epsilon_i$ is the difference in energy between sites *i* and *j,* and *kT* is the thermal energy.

Figure 3.3 displays a flowchart for generating the morphology, distribution of energies to each site and effects of band bending due to the effect of the built-in voltage of the device. For this modeling, the ETL and HTL free charge carrier densities were set at 5×10^{19} cm^{-3} and 3×10^{18} cm^{-3}, respectively [64]. The active layer sites were distributed with a density of 2.5×10^{20} cm^{-3} [64]. The average distance between two sites was set at 1 nm, and the critical distance (i.e., the minimum lattice distance between neighboring sites) was set at 0.64nm [123].

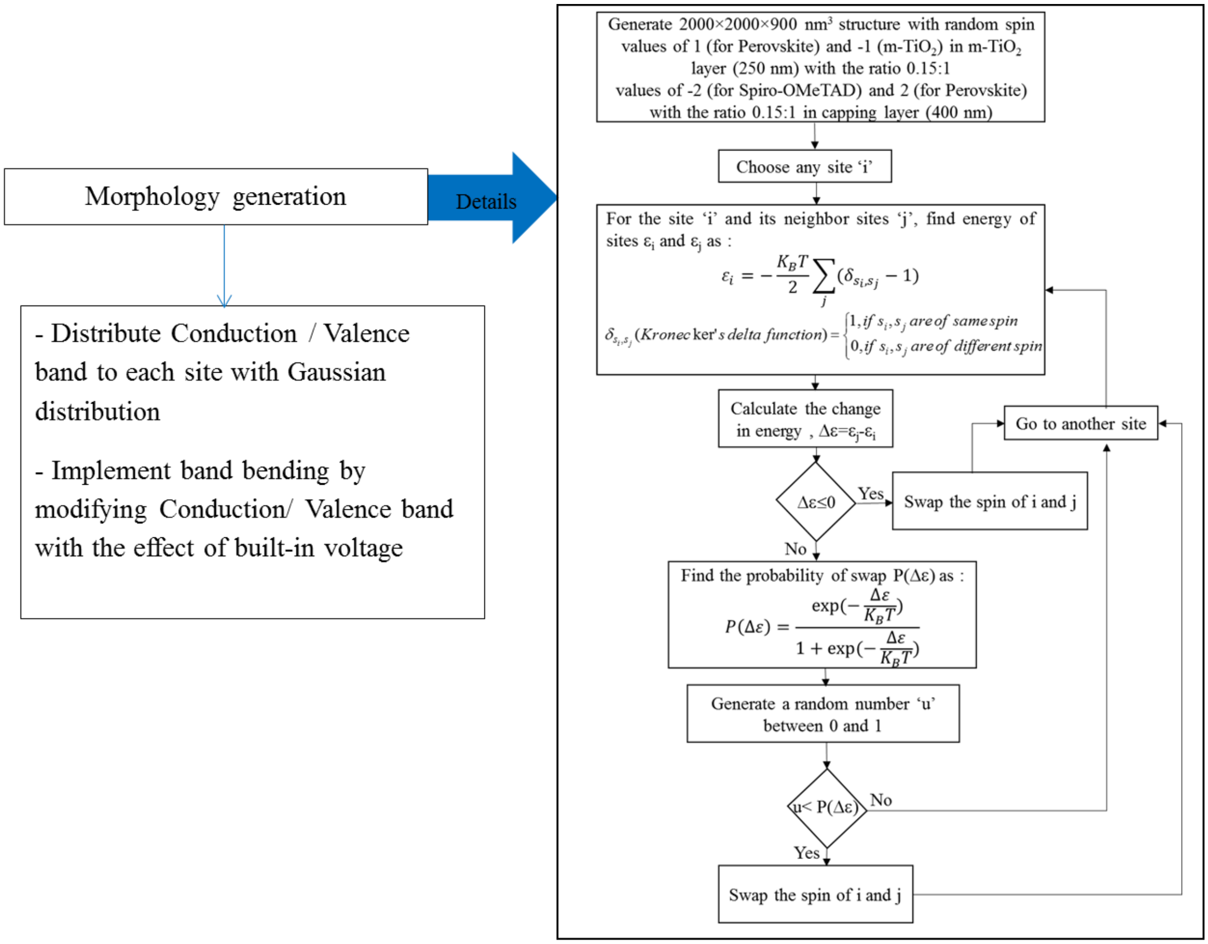

Figure 3.3. Flow Chart of Morphology Generation and Conduction/Valence Band Distribution [108]

Average lattice site for each lattice site is 1 nm. Neighboring sites are the sites within 3 nm radius. CBM and VBM of c-TiO_2, m-TiO_2, perovskite, and spiro-OMeTAD were assigned as -4.1eV/-7.3eV, -4.1eV/-7.3eV [151], -3.93eV/-5.4eV, and -2.1eV/-5.3eV [152], respectively. The CBM/VBM levels with a Gaussian energy distribution of 0.1 eV standard deviation were distributed to each site [64]. The capping layer is 2000 nm × 2000 nm × 400 nm in the x, y, and z directions respectively. The CBM of ETL (-4.1 eV) and VBM of HTL (-5.3 eV) were selected to collect separated charge carriers in perovskite solar cells efficiently. Therefore effective built-in voltage (V_{bi}) was 1.2 V. Considering V_A as applied voltage, the potential distribution was varied linearly from 0 V to (V_{bi}-V_A) across the z-direction of the active layer [59].

The following procedure is performed to implement band bending in the simulation models, assuming a Gaussian distributed random energy distribution

$$E_\sigma = \frac{1}{\sigma\sqrt{2\pi}} e^{-\frac{(x-\mu)^2}{2\sigma^2}} \tag{3.3}$$

where μ the is mean of the CBM donor or VBM acceptor materials, x is an arbitrary energy value, and σ is the deviation from the mean energy level, respectively: The net band energy (E_i) is calculated as the sum of the disorder, coulombic, and bias energies as

$$\begin{aligned} E_i &= E_\sigma + E_c + E_{bias} \\ E_c &= \sum_{j=1}^{n} \frac{q_i q_j}{4\pi\varepsilon_0\varepsilon_r r_{ij}} \\ E_{bias} &= qV_{bias}, V_{bias} = V_{bi} - V_A \end{aligned} \tag{3.4}$$

where E_c is the coulombic potential energy of charge i, r_{ij} is the mutual distance between a moving charge i and a neighboring charge j within the coulomb cut-off radius (r_c), ε_r is the relative dielectric permittivity, ε_0 is the free space permittivity, and n is the total number of charges inside r_c.

V_{bi} is the work function difference between the cathode and anode; it drives photogenerated carriers towards their respective electrodes. An external bias, V_A, is applied to the solar cell during current density versus voltage measurements. The net bias potential (V_{bias}) is the superposition of the built-in potential and external biases.

The overall site energy distribution at each time step was saved for each applied external bias voltage.

3.1.2 Calculation of Physical Event Rates

The major physical processes addressed in the simulation model were exciton generation, hole/electron transfer, and charge recombination in the active layer and charge injection/extraction in the active layer.

Illumination under 1.5 AM sunlight results in a generation rate (G_x) of $2.5nm^{-3}s^{-1}$ [58]. The overall generation rate of the perovskite capping layer surface coverage (s) under a solar illumination of 1.5 AM is given by

$$G(s) = s \times G_x(100) \tag{3.5}$$

where $G_x(100)$ is the generation rate in the active layer for a device with 100% surface coverage [153].

The charge transportation rate was calculated from equation (2.17), where the charge hopping pre-factor (w_{och}) was determined from equation (2.17). Assuming electron mobility (μ) of 6×10^{-3} cm^2 V^{-1} s^{-1} for m-TiO_2 and hole mobility of 50 cm^2 V^{-1} s^{-1} and 1×10^{-4} cm^2 V^{-1} s^{-1} for, the perovskite and spiro-OMeTAD, respectively, [64] the corresponding carrier hopping pre-factors were calculated as 0.286 ps^{-1}, 2.39 fs^{-1}, and 0.0048 ps^{-1}. Similarly, the net charge recombination rate (R_{CR}) was calculated from equation (2.19) with W_{CR} set at a constant rate of 35 $μs^{-1}$. The net rate is the sum of the monomolecular, bimolecular electron-hole recombination, and Auger recombination rates [154, 155].

The transport layers were retained neutral within the simulation by adding/removing a free carrier generated within 3 nm from the contacts to/from the transport layers. Equation (3.6) was used to calculate the injection (dark current) and extraction (photocurrent) carriers in the simulation assuming a free carrier density of 5×10^{19} cm^{-3} for the ETL and 3×10^{18} cm^{-3} for the HTL [64].

$$\begin{aligned}
\Delta n_{injection} &= n_{0-ETL} - n_{e-ETL} && if \;\; n_{0-ETL} > n_{e-ETL} \\
\Delta n_{extraction} &= n_{e-x} - n_{0-e_x} && if \;\; n_{e-x} > n_{0-e_x} \\
\Delta p_{injection} &= n_{0-HTL} - n_{h-HTL} && if \;\; n_{0-HTL} > n_{h-HTL} \\
\Delta p_{extraction} &= n_{h-x} - n_{0-h_x} && if \;\; n_{h-x} > n_{0-h_x}
\end{aligned} \tag{3.6}$$

where n_{0-ETL} and n_{0-HTL} are the numbers of electrons and holes in of the entire ETL and HTL, respectively, assuming thermal equilibrium. n_{0-e_x} and n_{0-h_x} are the number of electrons and holes, respectively, within a 3nm strip of the ETL and HTL assuming thermal equilibrium. n_{e-ETL} and n_{e-x} are the electron concentrations, respectively, within the entire ETL and a 3nm strip within the ETL. Similarly, n_{h-HTL} and n_{h-x} are the hole concentrations in the entire HTL and a 3nm strip within the HTL. Figure 3.4 displays a schematic of the ohmic contacts between the active and transport layers.

The total number of free carriers (n_c) within the transport layers at the current time step Δt is given by [156]

$$n_c = \frac{1}{A\Delta z}\sum_{i=1}^{n}\frac{\delta t_i}{\Delta t} \tag{3.7}$$

where $A\Delta z$ and δt_i are the transport layer volume and the time spent by the charge i in the transport layer, respectively. To be comparable with the relaxation time of the transport layers, a time step of 10^{-12}s was chosen [157].

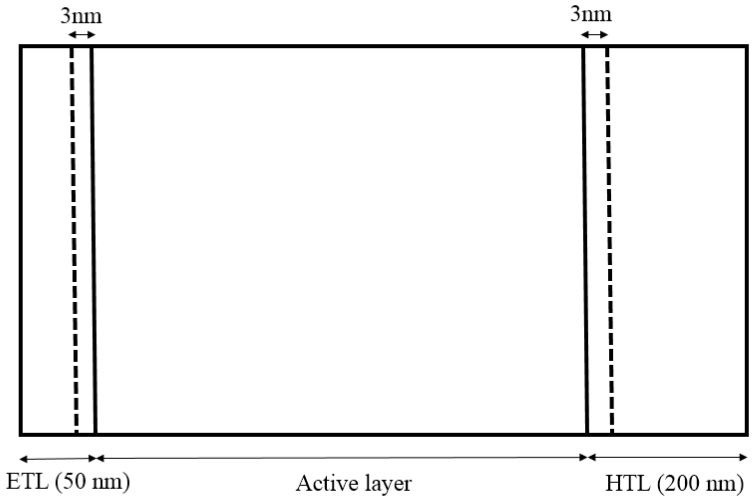

Figure 3.4. Ohmic Contacts between Active Layer and Transport Layers

3.1.3 Kinetic Monte Carlo Simulation

Figure 3.5 shows the flowchart describing the implementation of the KMC calculations, following the procedure described by Baidya *et al*. [158]. Two sets of calculations comprise the simulation. First of all, for each energy carrying particle, every possible event was calculated with considering possible reaction rate. For selected particle, only one event allows to happen base on randomly chosen. Second one, selected event rate calculated for all particles, to choose one particle that executes in the changes.

To implement these sets, out of the set of possible events for individual particles, the event with the maximum rate (minimum waiting time) was recorded. From the set of recorded events, one was randomly chosen and applied to execute the event for individual particle and increment the time step. The current state(s) of the particles near the individual particle were updated due to the change from the selected event. The simulation time was incremented, and the previous calculations repeated for all active particles. This process was repeated until convergence to a steady state (rate of charge generation equals the rate of charge carrier recombination plus the rate of charge carrier collection) was achieved. During each iteration, the numbers of injected, recombined, and extracted electrons/holes and each site's energy distribution and corresponding timestamp were saved to a database for further offline analysis.

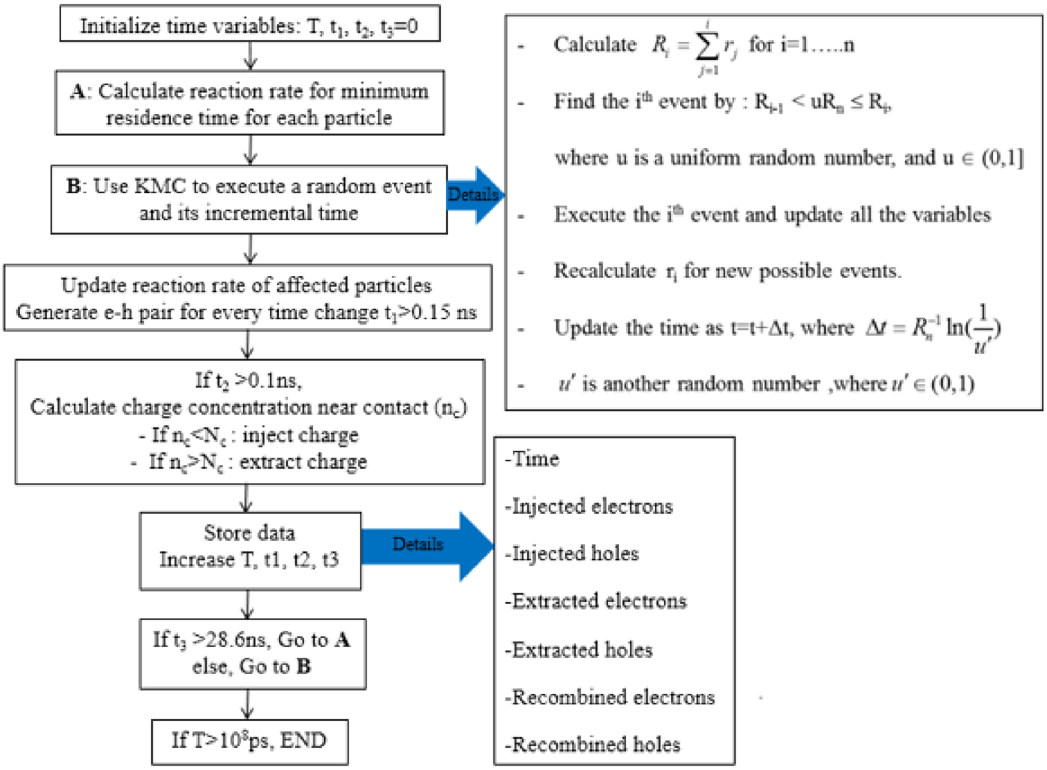

Figure 3.5. KMC Simulation and Energy Sites Tracking Flow Chart [108]

3.1.4 J-V Plots Generation and Data Analysis

A predictive current density-voltage characteristic analysis was performed based on the morphology resulting from the KMC simulations. Thirty-three measurements were acquired for this analysis, with applied voltages in the range of 0V to 1.2V. To obtain greater accuracy in the nonlinear portion of the characteristic curve, the step size between successive voltage measurements was varied. Between 0V and 0.8V, the voltage was varied in steps of 0.05V, while the voltage was varied in steps of 0.025 V between 0.8V and 1.2V. From the resulting J-V plots, the short circuit current density (J_{sc}) and open circuit voltage (V_{oc}) were estimated at the points V=0 and J=0, respectively. The maximum power J×V was also estimated. The equations (2.9) and (2.11) were used to calculate fill factor and efficiency, respectively. Figure 3.6 displays the flow chart of current density-voltage plot and simulation data analysis. For a given voltage, the net charge (injected electron + injected hole - extracted electron - extracted hole) was calculated and plotted as a function of time (Q-t). The resulting electric current at the applied voltage was estimated as the slope of a least-squares linear regression of the Q-t data.

From the Q-t data, the net current between two timestamps was estimated as follows:

$$I(t) = \frac{\Delta q(t)}{\Delta t} \tag{3.8}$$

The net current data were then fit to the decay equations in sections 2.8.5 and 2.8.6 to obtain the transient photocurrent (TPC) and transient photovoltage (TPV), respectively. The TPC was calculated assuming a short circuit condition; the TPV was calculated assuming a near-open circuit condition for a large resistance (~14 kΩ•cm^2) estimated from direct application of Ohm's law to the near open-circuit voltage level and a relatively small induced current. The TPC and TPV functions were then solved for the charge transport time (τ_t) and carrier recombination lifetime (τ_r).

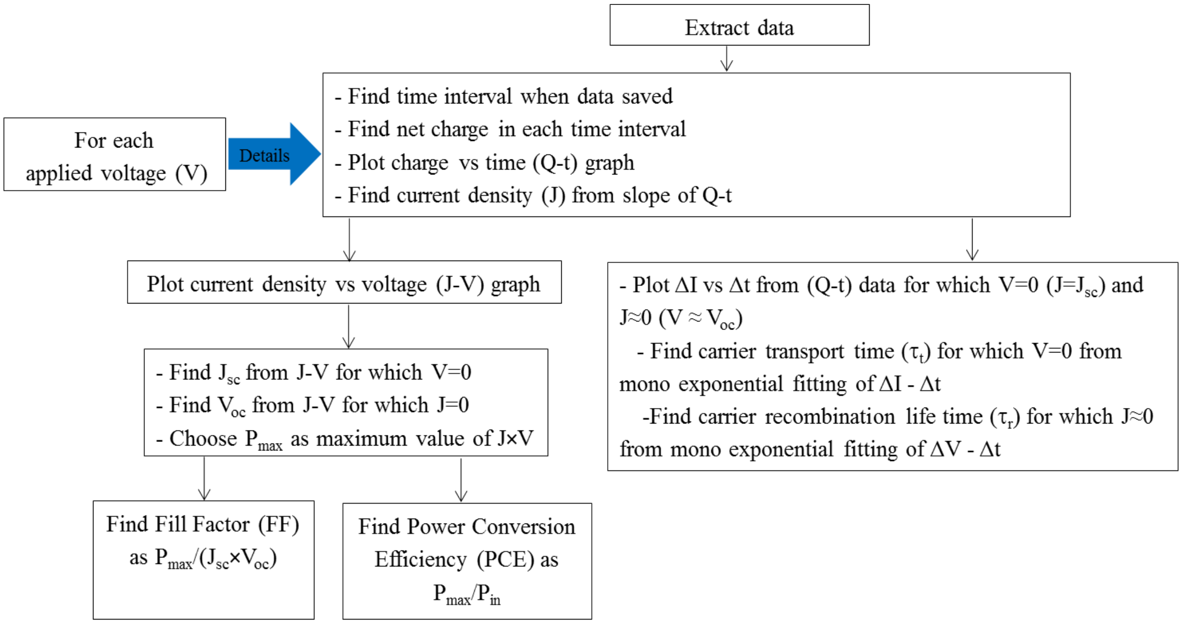

Figure 3.6. Predicted J-V Characteristic Generation and Data Analysis Flowchart

3.1.5 Coulombic Interaction Model

The coulombic energy varies as charge carriers are transferred from one localized site to a neighbor site. The change in coulombic energy results in changes in the overall hopping rate for each carrier. As mentioned in section 2.5, the coulombic cut-off radius (r_C) is the maximum distance over which a charge carrier can experience the Coulomb force from another charge carrier. Figure 3.7 shows the procedure for estimating the coulombic energy interaction for a given cut-off radius. For this work, the cut-off radius was set to 3 nm, which is equal to the thermal capture radius. The coulombic potential energy at site *i* was calculated according to

$$E_{C,i} = \sum_{k=1,k\neq i}^{N} \frac{q_i q_k}{4\pi\varepsilon_0\varepsilon_r r_{ik}} \quad where\, r_{ik} < 3nm \tag{3.9}$$

where q_k is the charge at site *k*, ε_r and ε_0 are, respectively, the relative and absolute permittivity. If site *j* was vacant (i.e., no charge carrier at that site), then the coulombic potential energy ($E_{C,j}$) at site *j* was calculated assuming the charge at site *i* was located at site *j*. The change in coulombic potential energy ($\Delta E_{C,ij}$) when the charge hopped from site *i* to *j* was determined from

$$\Delta E_{C,ij} = E_{C,j} - E_{C,i} \tag{3.10}$$

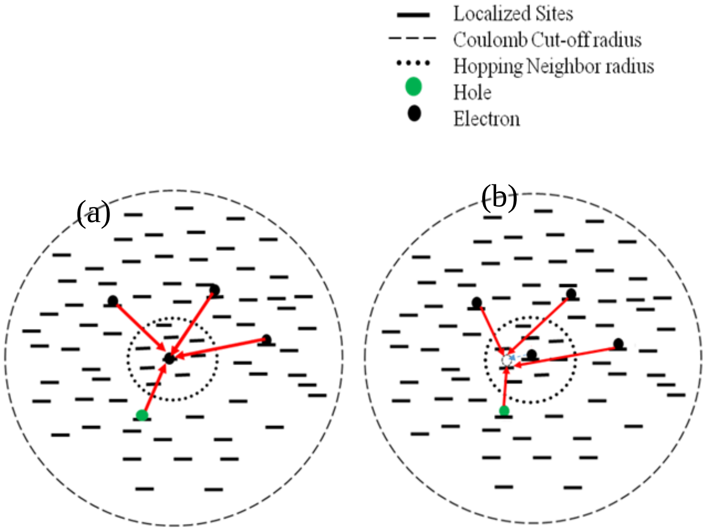

Figure 3.7. Coulombic Interactions of Charge Particles (a) at Site i; (b) at Site j [158].

3.1.6 Simulation on High Performance Computing

All morphology simulations and predictive analyses were performed using the MATLAB Release 14a software on the “blackjack” host in the SDSU HPC cluster. Origin 9.0 and MATLAB were used to generate all plots. PuTTY 0.66 was used to establish an SSH connection to the “blackjack” host to allow job scheduling/execution and simulation definition (through Pbs script) from a remote client computer running Microsoft Windows. WinSCP 5.7.6 beta was used for file transfer between the client computer and the cluster.

3.2 Fabrication Procedure

3.2.1 Materials

Compact TiO_2, mesoporous TiO_2 (30NRD) and methylammonium iodide (CH_3NH_3I) were purchased from Dyesol (http://www.greatcellsolar.com, Queanbeyan, Australia). Lead iodide (PbI_2) was purchased from Fisher scientific (Acros Organics) (https://www.acros.com, NJ, USA). Spiro-OMeTAD was purchased from Lumtec (http://www.lumtec.com.tw, new Taipei City, Taiwan). FTO coated glass substrates were ordered from Hartford Glass Company (http://www.hartfordglassco.com, Hartford City, IN, USA). Ag was purchased from Kurt J. Lasker (https://www.lesker.com, Jefferson Hills, PA, USA). The materials were then used to fabricate n-i-p organic lead halide-based perovskite cells according to the procedure described in the following section. Figure 3.8 shows the basic structure of the fabricated cells. Table 1.1 summarizes the layer fabricated from each material.

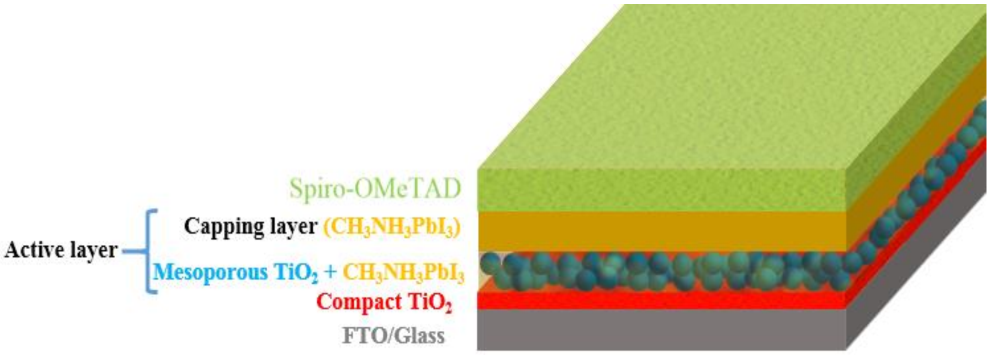

Figure 3.8. n-i-p Structure of Fabricated Perovskite Solar Cell

Table 3.1. Materials used at Different Layers of Perovskite Solar Cells [95]

Layer	Material
Cathode	Fluorine tin oxide (FTO)
ETL	Compact TiO_2, m-TiO_2
Active layer	Perovskite ($CH_3NH_3PbI_3$)
HTL	Spiro-OMeTAD
Anode	Silver (Ag)

3.2.2 Device Fabrication

1.5 cm × 1.5 cm glass substrates coated with fluorine-doped tin oxide (FTO) were used for the cell base. Zinc powder in a solution of 0.1 ml HCl in 1 ml distilled H_2O was used to etch the substrates. The etched substrates were subsequently sonically cleaned for 25 minutes with detergent water and rinsed with DI water, acetone, and isopropanol, respectively. The substrates were then dried in a nitrogen atmosphere, then subjected to plasma treatment in the presence of oxygen for 20 minutes.

3.2.2.1 Electron Transport Layer Deposition

Compact layers of TiO_2 (titanium diisopropoxide bis(acetylacetonate), 75 wt.% solution in 2-propanol) prepared from its precursor 0.15M solutions were spin coated onto the cleaned substrates at 4500 rpm for 45 seconds, which were then annealed at 200 ˚C for 10 min. After cooling to room temperature, a mesoporous TiO_2 paste (diluted in ethanol at a weight ratio of 1:6) was spin coated onto the substrate at 5000 rpm for 30 seconds, followed by annealing the substrates at 460 ˚C for 30 min. After cooling to room temperature, the substrates were then dipped in a 25mM $TiCl_4$ solution heated to 70 ˚C for 30 minutes, rinsed with distilled water and ethanol, then annealed at 460 ˚C for 30 min.

3.2.2.2 Active Layer Deposition

To fabricate different capping layers of varying coverage, PbI_2 solutions of varying concentrations (62, 262, 462, 662 mg/ml in DMF) were prepared by overnight stirring at 70 ˚C. The solutions were then spin coated onto a mesoporous TiO_2 layer at 4000 rpm for 40 seconds then annealed at 70 ˚C for 30 minutes. To form the perovskite layers, the resulting PbI_2 films were dipped in CH_3NH_3I solution (10 mg/ml in IPA) for 60 seconds then immediately spin coated at 6000 rpm for 10 seconds. The resulting perovskite films were then annealed at 100 ˚C for 15 minutes.

To fabricate different capping layer thicknesses, a 462 mg/ml PbI_2 solution was spin-coated onto a 250 nm thick mesoporous TiO_2 layer from 2000 rpm to 5000 rpm in steps of 1000 rpm for 40 sec.

3.2.2.3 Hole Transport Layer and Silver Anode Deposition

Spiro-OMeTAD was used to fabricate the HTL. The spiro-OMeTAD solution was prepared by adding 72.3 mg of (2,2′,7,7′-tetrakis(N,N-di-p-methoxyphenylamine)-9,9-spirobifluorene) (spiro-OMeTAD) powder, 28.8 µL of 4-tert-butylpyridine, and 17.5 µL of a stock solution containing 520 mg/mL lithium bis (trifluoromethylsulfonyl)imide in acetonitrile in 1 mL of chlorobenzene. The spiro-OMeTAD solution was spin coated onto the perovskite active layer at 2000 rpm for 40 seconds. Finally, a layer of silver (Ag) was then deposited, through thermal evaporation in vacuum, onto the substrate as an electrode.

3.3 Parameter Variations

During simulation, different perovskite solar cells with varying capping layer coverage and thickness were simulated. During the fabrication process, different perovskite cells were fabricated with varying PbI_2 concentrations and spin coating speeds. The following sections describe the variations in parameters required for the simulated and fabricated cells.

3.3.1 Parameter Variation – Model Simulations

Two different cases of parameter variation and their effects on performance were simulated. In the first case, four models were simulated assuming a 400 nm thick capping layer at coverages of 85%, 90%, 95%, and 100%. In the second case, four perovskite solar cells were simulated assuming a capping layer of 100% coverage at thicknesses of 350 nm, 400 nm, 450 nm, and 500nm. In both cases, the perovskite/mesoporous TiO_2 ratio was fixed at 0.15:1.

3.3.2 Parameter Variation – Cell Fabrication

Two different cases of parameter variations and their effects on performance were observed in fabrication as well. The varied parameters were the capping layer coverage and thickness, and the cells representing these variations were fabricated as described in section 3.2.2.2.

3.4 Film Characterizations

Five sets of measurements were performed to characterize the perovskite films fabricated with varying capping layer coverages and thicknesses. The following sections briefly describe the instruments used in the various characterization analyses.

3.4.1 UV-Visible Absorption Spectroscopy

An Agilent 8453 spectrophotometer with ChemStation software was used to measure UV-Vis absorption spectra (Figure 3.9). The instrument uses a mercury lamp for to provide ultraviolet (UV) light and a tungsten lamp to provide visible and near infrared (NIR) light.

A baseline absorption spectrum for a glass/FTO/TiO_2 substrate was obtained in the instrument's "blank" mode. Absorption spectra of the glass/FTO/TiO_2/perovskite substrates fabricated with varying capping layer coverages and thicknesses were then acquired in the instrument's "automatic" mode. The absorption spectra of the perovskite films were obtained by subtracting the baseline spectrum from the glass/FTO/TiO_2/perovskite substrate spectra.

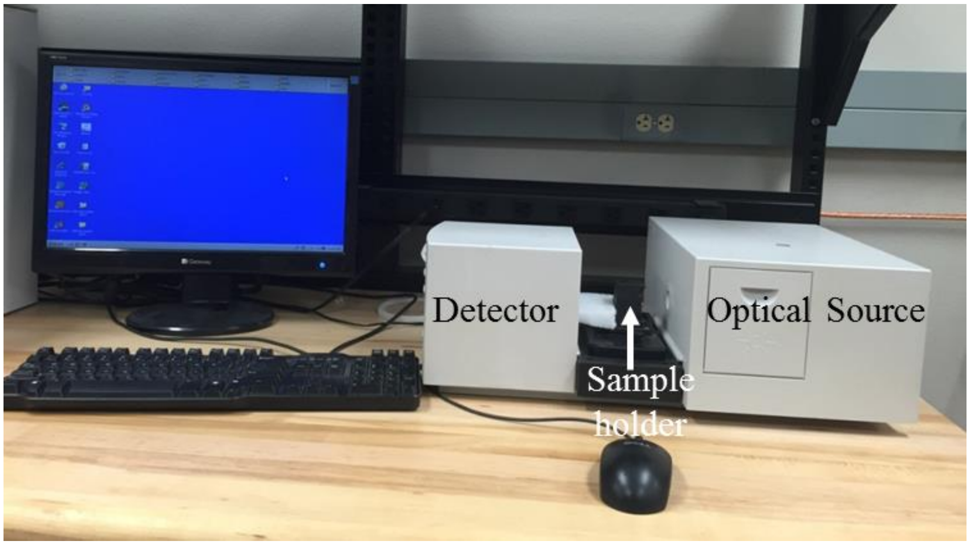

Figure 3.9. Agilent 8453 UV-Visible Spectrophotometer

3.4.2 X-ray Diffraction (XRD)

The Rigaku Smartlab system was used to record X-ray diffraction (XRD) spectra (Figure 3.10). X-rays with a wavelength of 1.54 Å were produced by a copper tube in the source at an operating voltage and current of 40 kV and 44 mA, respectively.

XRD spectra were recorded with the perovskite samples oriented horizontally in the instrument; the X-ray source and detector were rotated about the sample's z-axis with a goniometer. The measurements were acquired as a function of 2θ from 5° to 60°, using the instrument's parallel beam/parallel sample medium resolution mode in steps of 0.01°.

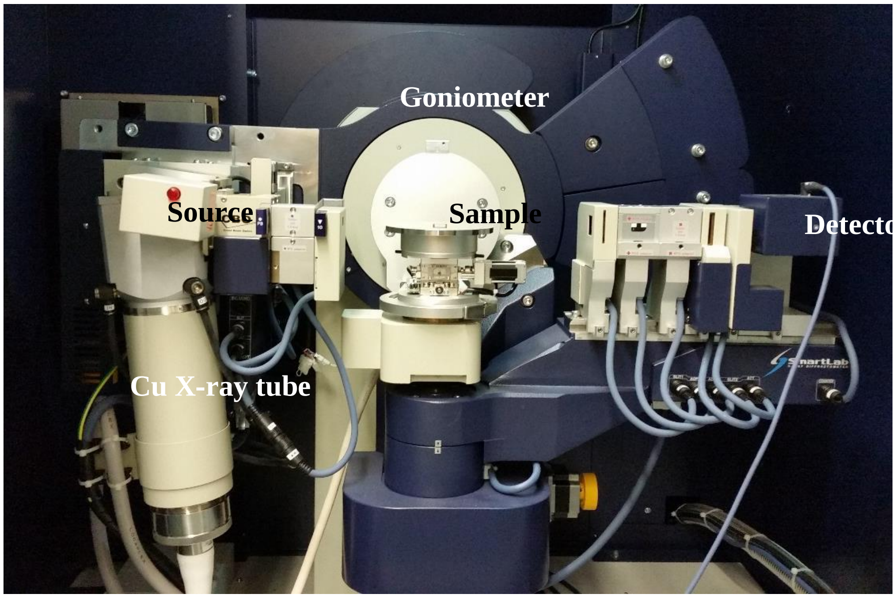

Figure 3.10. Rigaku Smartlab X-Ray Diffraction Diffractometer

3.4.3 Atomic Force Microscopy (AFM)

An Agilent SPM 5500 atomic force microscope (Figure 3.11) was used to map the topography and phase images for the perovskite film samples containing varying PbI_2 concentrations. A Si tip coated with Cr/Pt (Budget Sensors, Multi75 Eg, resonant frequency: ~75 KHz, spring constant ~1-4 N/m) was used for measurements in tapping mode. A lock-in amplifier (LIA1) was used to control the vertical separation between the tip and the sample at a resonant frequency (f1) of 71 kHz. The Gwyddion software was used to measure the percent coverage of the capping layers and their roughness from the image data [159, 160].

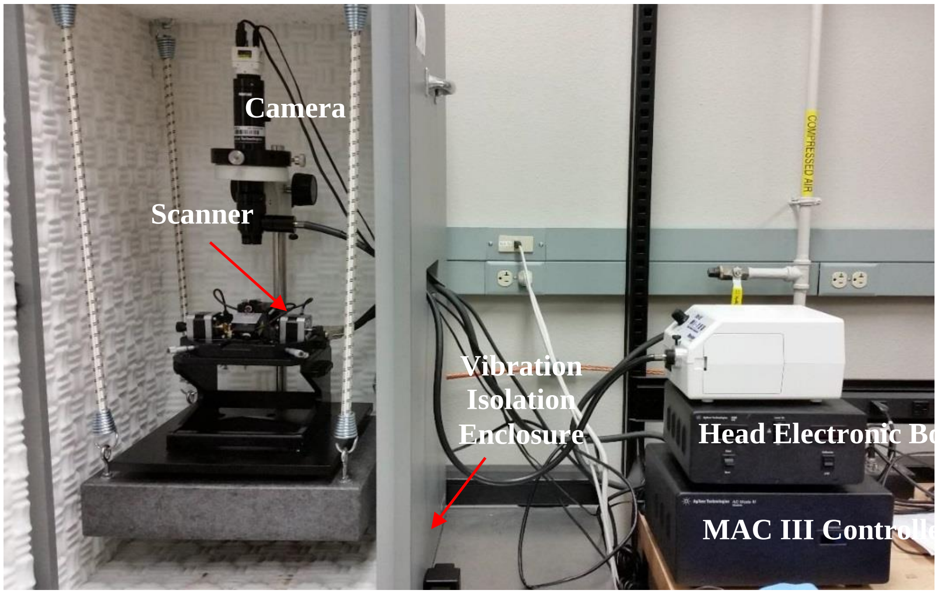

Figure 3.11. Agilent SPM 5500 Atomic Force Microscope

3.4.4 Scanning Electron Microscope (SEM)

A Hitachi S-3400N SEM (Figure 3.12) was used to image the surface morphology of perovskite film samples of varying PbI_2 concentrations. Prior to imaging, the films were coated with a 10 nm layer of gold. Imaging was performed in a vacuum environment, at a working distance of approximately 10 mm at a magnification factor of 5000. The instrument was operated with an accelerating voltage of 5 kV.

Figure 3.12. Hitachi S-3400N SEM.

3.4.5 Dektak 150 Profilometer

A Dektak 150 profilometer (Figure 3.13) was used to measure the film thickness of the active and transport layers fabricated with the varying capping layer thicknesses, with a constant (software-defined) force of approximately 5 mg at a maximum height of 6.5 µm.

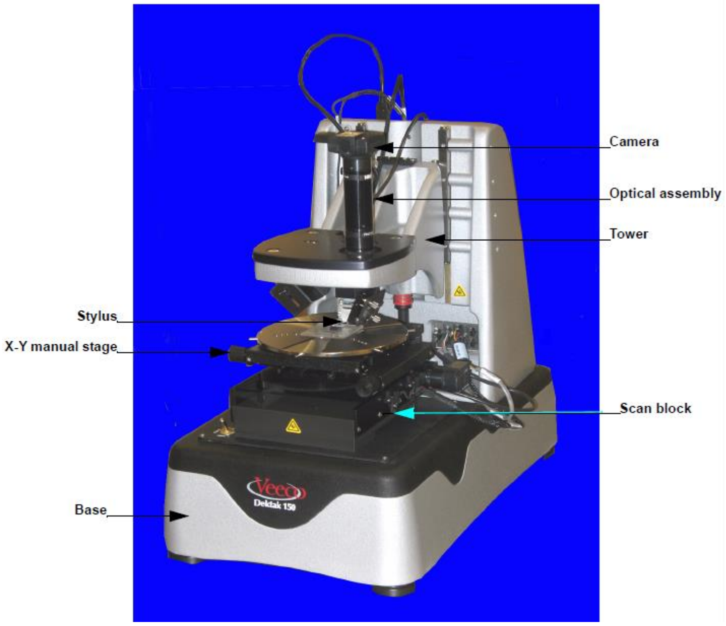

Figure 3.13. Dektak 150 Profilometer [161]

3.5 Device Characterization

3.5.1 Current Density-Voltage (J-V) Measurement

The current-voltage characteristics of the fabricated solar cell devices were measured with an Agilent 4155C semiconductor parameter analyzer (Figure 3.14) under an AM 1.5 illumination level of a Newport Xenon lamp at an intensity of approximately100 mW/cm^2; the Agilent 4155C semiconductor parameter analyzer applied the bias voltage and measured the resulting current. To ensure uniform illumination, the lamp was turned on and allowed to warm up for 30 minutes prior to acquiring any measurements. A National Renewable Energy Laboratory (NREL) photodetector (S1133 14-01) was used to calibrate the distance between the Xenon lamp and the photodetector.

All solar cells with an area of 0.16 cm^2 were characterized under the same conditions at a constant scanning rate of 0.5 V/s, sweeping from 0 V to 1.10 V for forward scans and 1.10 V to 0 V for reverse scans.

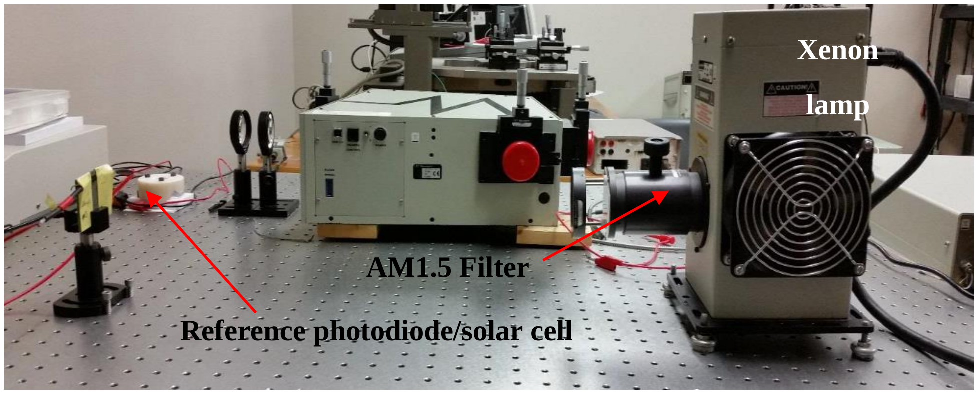

Figure 3.14. Solar Cell J-V Characteristic Measurement

3.5.2 External Quantum Efficiency Measurement (EQE)

A Newport Incident Photon to Current measurement kit was used to measure each cell’s external quantum efficiency (EQE). Two convex lenses in series were used to focus the light from a Cornerstone 260 monochromator onto a photodiode, as shown in Figure 3.15. The monochromator produces a monochromatic beam to an accuracy of approximately 0.35 nm. The monochromator input was varied in 5 nm steps from 500 nm to 800 nm. At each wavelength, a lock-in amplifier converted the output current from the device under test to a voltage level that was recorded by the Agilent 4155C analyzer. Voltage measurements were also performed for the reference sample (S1133-14).

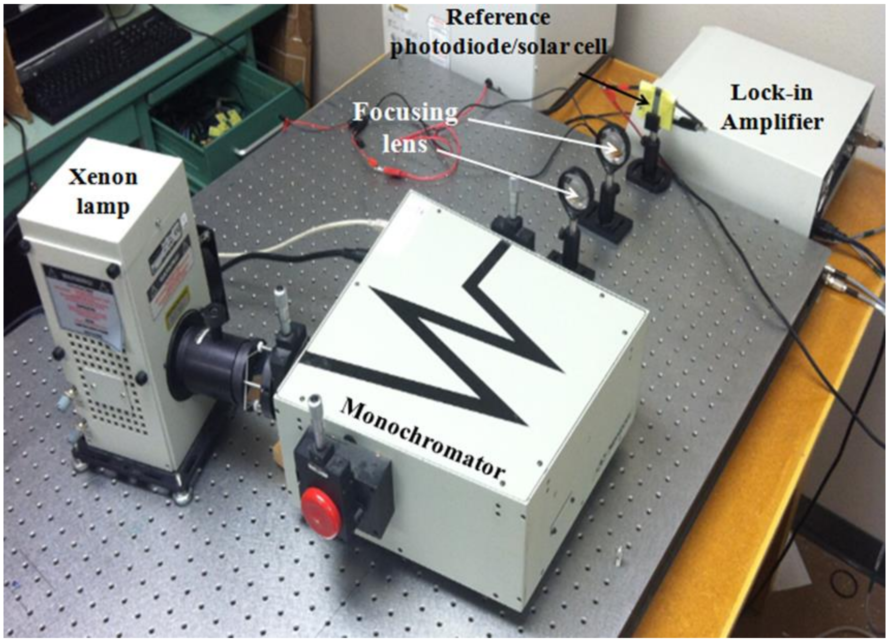

Figure 3.15. EQE Measurement Setup.

3.5.3 Transient Photocurrent/Photovoltage Spectroscopy

Transient photocurrent/photovoltage spectroscopy measurements were performed with the setup shown in Figure 3.16. A nitrogen laser coupled to a Model 1011 dye laser generated pulses of less than 1 ns width at a frequency of approximately 4 Hz; to ensure uniform pulses reached the cell's active layer, the pulse wavelength was chosen to be as close as possible to the perovskite film's absorption peak wavelength. The pulses were then directed to a beam splitter directing half of the beam to a photodiode and half to the solar cell under test. An Agilent MSO-X-4154A mixed oscilloscope (1.5 GHz, 5 Gsa/sec) was used to record the resulting current and voltage transients. The charge transport time (τ_t) and charge carrier recombination lifetime (τ_r), respectively, were obtained from the generated transient photocurrent and photovoltage measurements. For the TPV measurements, the solar cells were illuminated with an external halogen lamp source in order to obtain steady state conditions. The short-circuit TPC measurements used a 50 Ω resistance, while the (near) open-circuit TPV measurements were performed using a 1 MΩ resistance. As mentioned in sections 2.8.5 and 2.8.6, the data were fitted to exponential decay functions which were then solved for τ_t and τ_r.

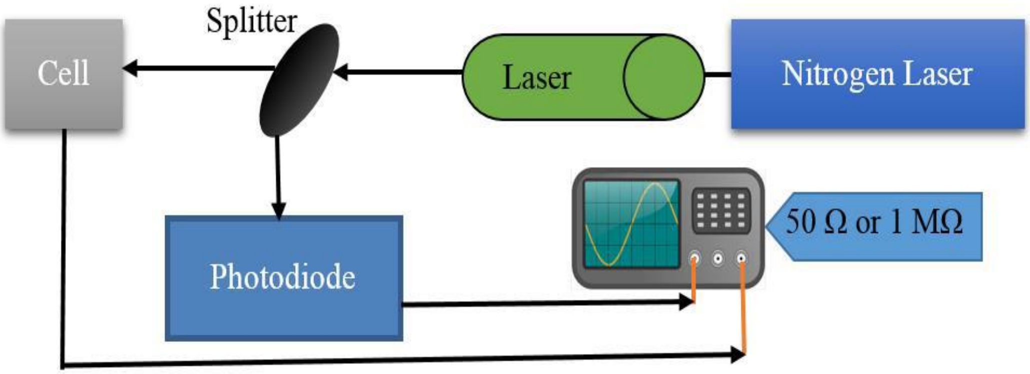

Figure 3.16. Transient Photoconductivity Measurement Set up [95] .

Chapter 4: Results and Discussion

4.1 Perovskite Solar Cell Structure Simulation

An n-i-p perovskite solar cell with 100% capping layer coverage generated by Monte Carlo (MC) simulation as mentioned in section 3.1.1 and shown in Figure 3.1 , The compact-TiO_2 and spiro-OMeTAD considered as an electron transport layer (ETL) and hole transport layer (HTL), respectively. The ETL and HTL are parallel to an x-y plane located at $0 < z \leq 50$ and $700 < z \leq 900$ with a thickness of 50 nm and 200 nm. The active layer considered with mesoporous-TiO_2 and perovskite located at $50 < z \leq 300$ with a thickness of 250 nm plus capping layer located at $300 < z \leq 700$ with a thickness of 400 nm.

4.2 Variation of Morphological Parameters in Simulation

4.2.1 Variation of Capping Layer Coverage

The MC model developed to simulate the perovskite morphology was based on the Metropolis algorithm. Figure 4.1 (a,c,e,g) and (b,d,f,h) show, respectively, the 3D and top view simulated morphology of the perovskite capping layer, at capping layer coverages of 85%, 90%, 95%, and 100%. The yellowish-brown regions in the simulated morphology are assigned to the perovskite, whereas the white regions are assigned to any pinholes and large gaps between the perovskite grains.

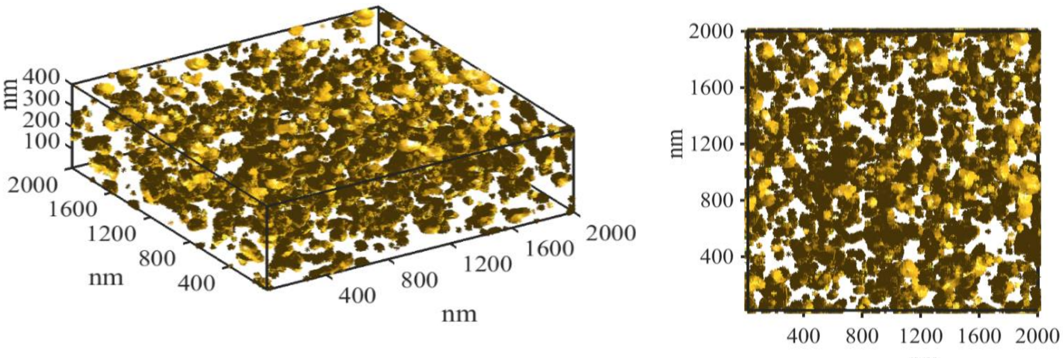

(a) 85% coverage

(b) 85% coverage

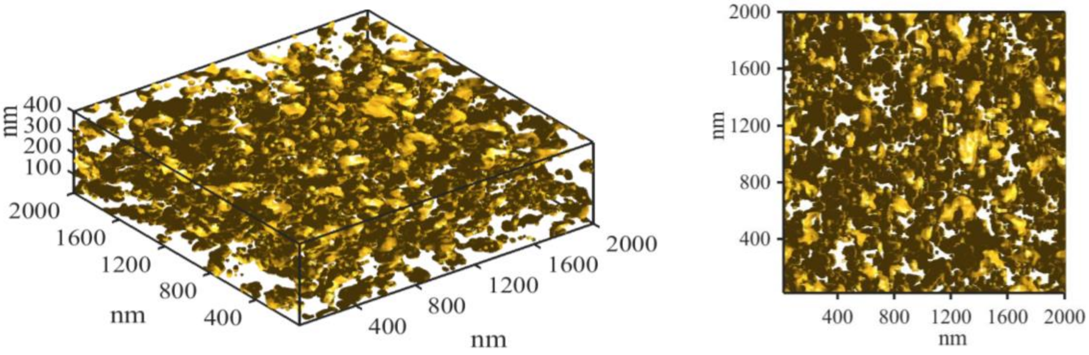

(c) 90% coverage

(d) 90% coverage

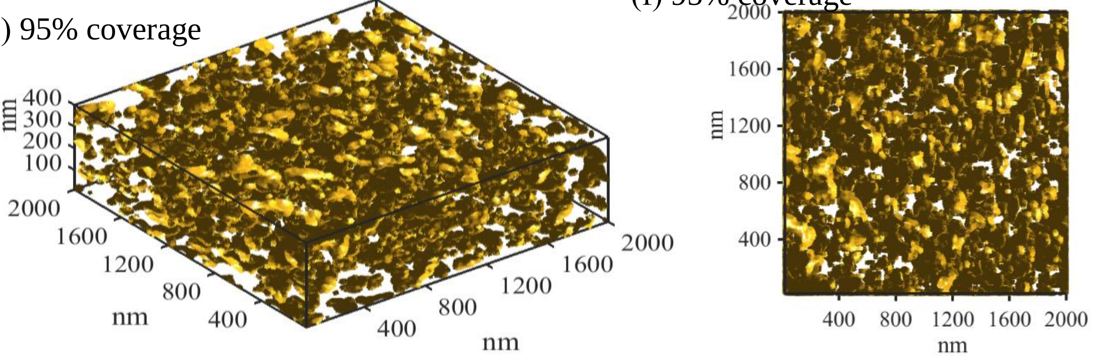

(e) 95% coverage

(f) 95% coverage

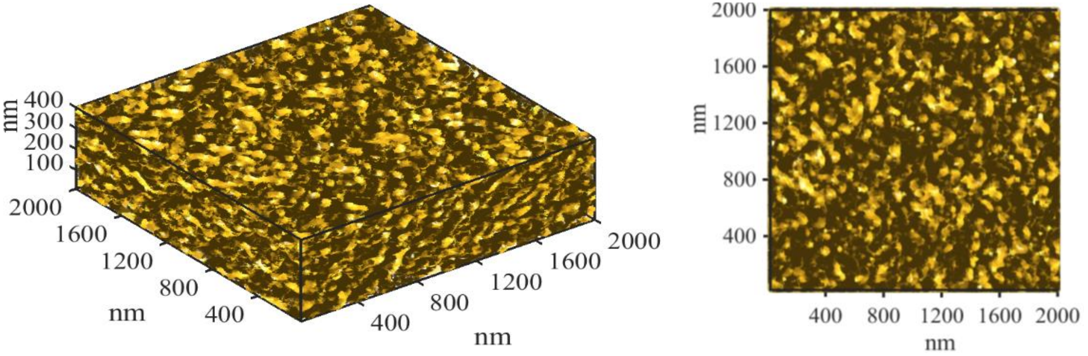

(g) 100% coverage

(h) 100% coverage

Figure 4.1. 3D Image and Top View, Simulated Morphology of Perovskite Solar Cells with Different Capping Layer Coverage (a, b) 85%; (c, d) 90%; (e, f) 95%; (g, h) 100%

Appropriate electronic band alignments between the ETL, HTL and the perovskite absorber layer are required for optimal device performance. Electrons need to transfer from the perovskite to ETL, and holes from the perovskite to the HTL, without any significant energy loss. The KMC simulation can visualize the energy band diagram of perovskite solar cells. Figure 4.2(a-d) show the energetic disorder for different capping layer coverages related to localized sites within a horizontal slice ($29 \leq x \leq 30$ nm, $20 \leq y \leq 30$ nm), with band bending of CBM and VBM levels at 0 V (without applying forward bias). Figure 4.2 (e-h) show the resulting flattening the band bending in the same slice when applying forward bias (0.975 V, 1.025 V, 1.050 V, and 1.10 V) for different capping layer coverages (85%, 90%, 95% and 100%), respectively. The band flattening results from the weak electric field induced in the absorber layer by applying a forward bias. The corresponding CBM and VBM offset also decrease with application of the forward bias.

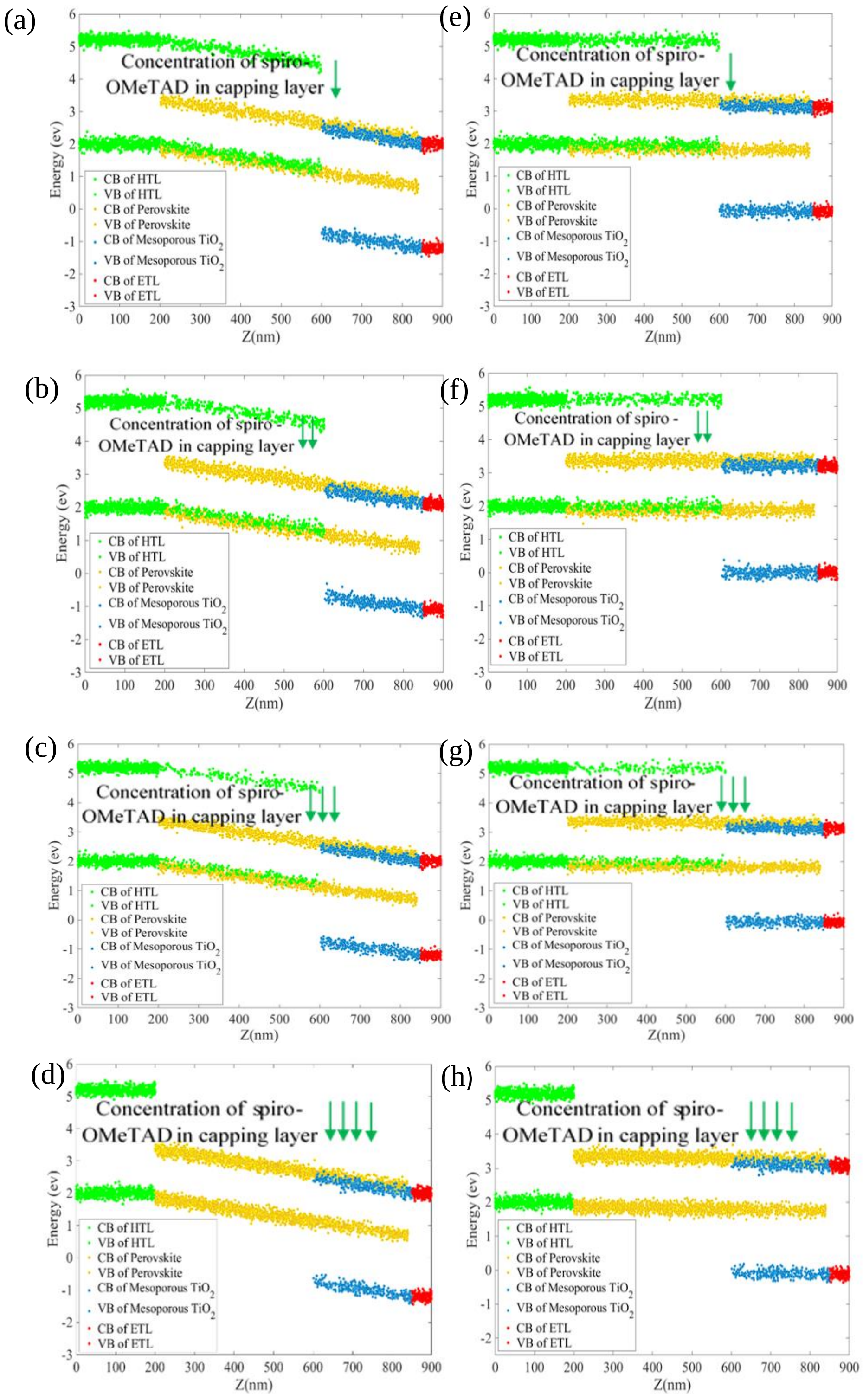

Figure 4.2. (a-d) Energy Band Diagram under Thermal Equilibrium; (e-h) Under 0.975 V, 1.025 V, 1.050 V and 1.10 V Forward Bias for Different Capping Layer Coverages (85%, 90%, 95 % and 100%) respectively.

Figure 4.3 (a) displays the simulated J-V characteristics of perovskite solar cell with different capping layer coverage of 400 nm thickness. Table 4.1 lists the simulated device performance, the number of recombination events at the J-V characteristic maximum power point (MPP), charge transport time (τ_t), and charge carrier recombination lifetime (τ_r) for different capping layer coverages. To reach effective interface properties and photovoltaic performance, the pin holes-free, and homogenous perovskite capping layer are critical [162-164]. The simulation inputs assume an increase in charge generation as the capping layer coverage increases. Lesser coverage led to less efficient charge transport pathways for carrier diffusion. In addition, a larger percentage of the gaps were filled with spiro-OMeTAD, which has a charge transport rate approximately 10^6 times less than the perovskite; this resulted in an increased number of recombination events. As a result, cell performance decreased with decreasing perovskite coverage in the capping layer.

Figure 4.3 (b) and (c) show the simulated transient photocurrent and photovoltage decays. The transient decays were calculated using the same approach described in section 3.1.4. The simulation estimated a τ_t of approximately 2.14 μs and a τ_r of approximately 8.32 μs for the highest efficiency device at 100% capping layer coverage.

The predicted number of recombination events at MPP, charge carrier transport time, and charge carrier lifetime (Table 4.1) are consistent with the J-V characteristic results. For all capping layer coverage levels, the τ_r is longer than τ_t, ensuring that generated carriers will reach their electrodes before recombination can occur. The simulation predicted a decrease in the number of recombination events and τ_t with increasing capping layer coverage; the τ_r was predicted to increase. At 100% coverage, the τ_t was at its minimum, and the τ_r was at its maximum. Figure 4.3 (d) shows the number of recombination events at the MPP versus capping layer coverage.

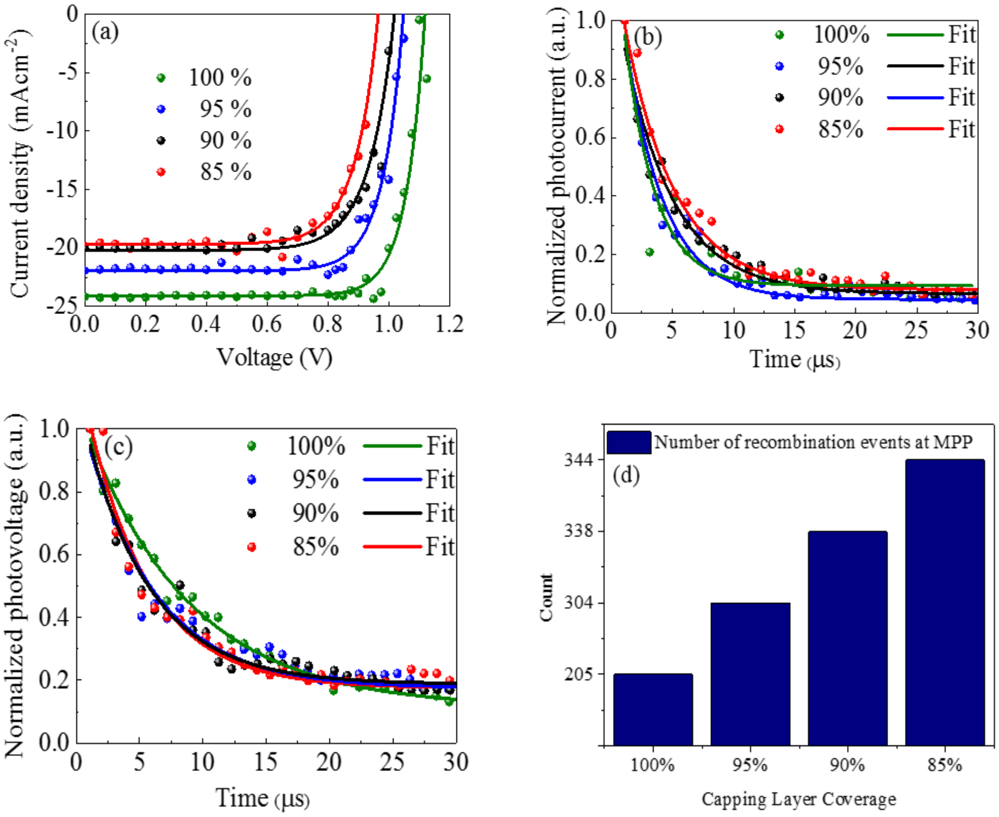

Figure 4.3. Simulated Cell Performance vs. Capping Layer Coverage: (a) Predicted J-V Characteristics; (b) TPC Decay; (c) TPV Decay; (d) Number of Recombination Events at J-V MPP

Table 4.1. Simulated Device Performance of Perovskite Solar Cells at 85%, 90%, 95%, and 100% Capping Layer Coverage

Capping layer Coverage (%)	**J_{sc} (mA/cm^2)**	**V_{oc} (V)**	**Fill Factor**	**Efficiency (%)**	**Number of Recombination Events at MPP**	**τ_t (μs)**	**τ_r (μs)**
85	19.83	0.97	0.72	13.84	344	4.16	5.95
90	20.20	1.02	0.73	15.04	338	4.11	6.15
95	21.94	1.05	0.76	17.50	304	3.21	6.56
100	**24.09**	**1.11**	**0.78**	**20.85**	**205**	**2.14**	**8.32**

4.2.2 Variation of Capping Layer Thickness

The thickness of the capping layer z was varied from 350 nm to 500 nm in steps of 50 nm, while the device x and y dimensions were fixed. Figure 4.4 (a-d) shows the device morphologies with different capping layer thickness at 100% capping layer coverage. The actual capping layer thickness was obtained after subtracting 300 nm for the ETL and 200 nm for the HTL.

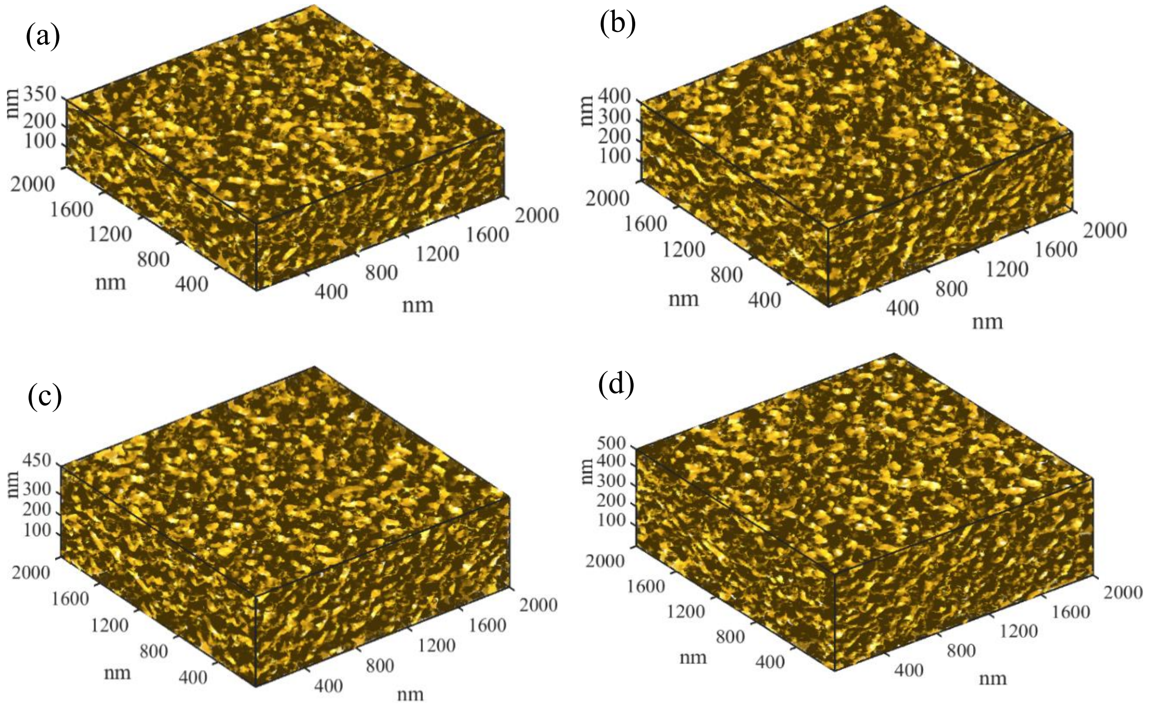

Figure 4.4. Simulated Morphology of Perovskite Solar Cells with Different Capping Layer Thickness (a) 350 nm; (b) 400 nm; (c) 450 nm; (d) 500 nm

Figure 4.5 (a) shows the simulated J-V curves for each capping layer thickness, assuming full illumination. The simulated J-V curves show that the thickness of the perovskite layer has a critical role in device efficiency. Table 4.2 shows the simulated device performance, the number of recombination events at the J-V characteristic MPP, τ_t and τ_r as a function of capping layer thickness.

The photon absorption efficiency in the simulated cells was directly proportional to capping layer thickness, with thicker layers providing increased absorption [163, 165]. However, thicker capping layers have reduced carrier transport efficiency. The device efficiency was low in the capping layer with 350 nm thickness [Figure 4.4 (a)] due to insufficient photon absorption. However, the capping layer with a thickness of 500 nm [Figure 4.4 (d)] had sufficient photon absorption but less efficient charge transport to the electrodes; the longer pathway results in a greater probability of carrier recombination before reaching the ETL and HTL. As a result, the overall efficiency is reduced. Maximum efficiency of approximately 20.85 % was obtained with an optimized perovskite capping layer thickness of 400 nm.

Figure 4.5 (b) and (c) show the predicted TPC and TPV decay as a function of capping layer thickness. The transient decays were calculated using the same approach described in section 3.1.4. The predicted number of recombination events at the J-V MPP, τ_t, and τ_r (Table 4.2) are consistent with the J-V characteristics results. With thinner capping layers, decreased photon absorption causes insufficient charge carrier collection. Therefore, the charge carrier will accommodate certain sites with a longer distance between each charge carrier. Coulombic interactions decrease as a result of the greater distance between each carrier, resulting in an increased τ_t and reduced τ_r. With thicker layers, more photon absorption results in more charge carriers. Thus, the probability of recombination increases, which accounts for the increase in τ_t and the decrease in τ_t.

The simulation predicted that at an optimized thickness of 400 nm, position-dependent coulombic interactions between charge carriers result in a balance between the carrier collection efficiency and the photo-generated charge carrier. The number of recombination events at MPP increased by increasing the thickness of the capping layer. Figure 4.5 (d) shows the number of recombination events at MPP versus different thickness of the capping layer.

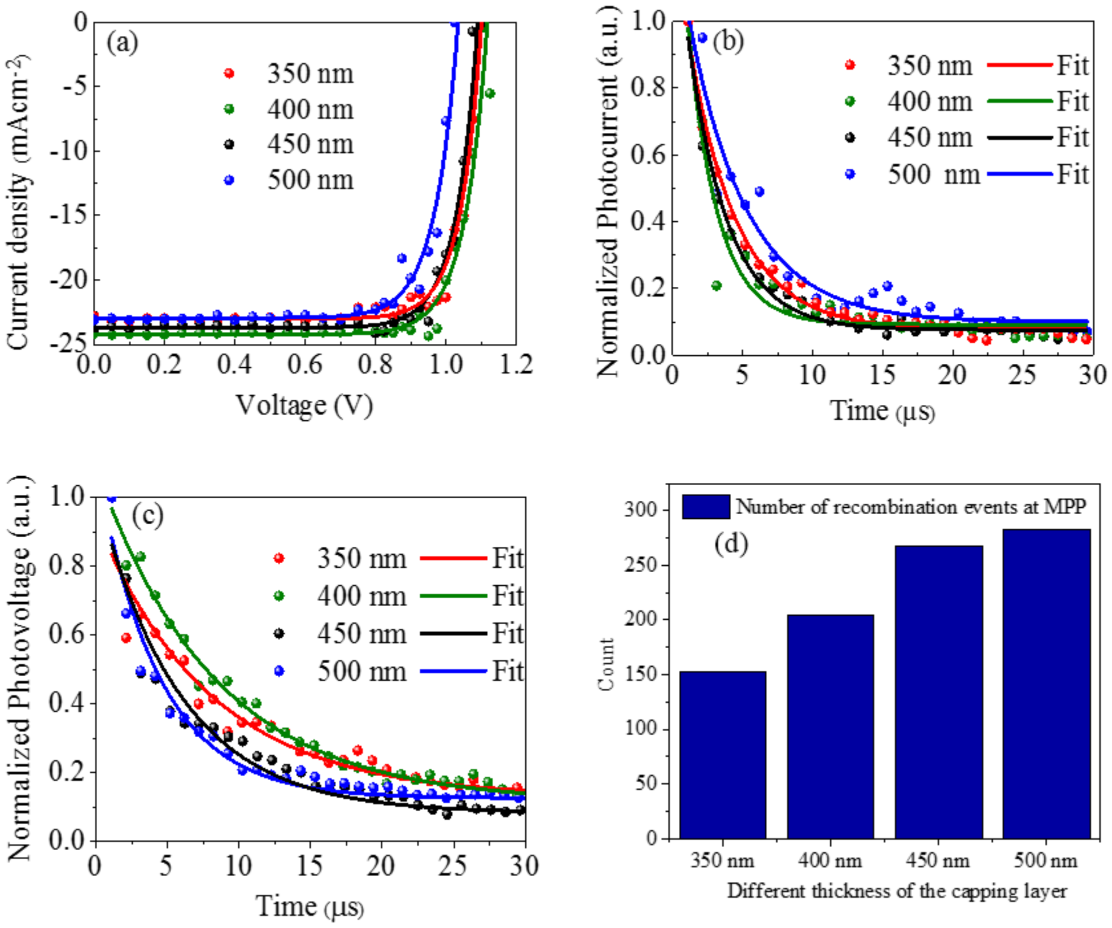

Figure 4.5. (a-d) Simulated Cell Performance vs. Capping Layer Thickness: (a) Predicted J-V Characteristics; (b) TPC Decay; (c) TPV Decay; (d) Number of Recombination Events at J-V MPP

Table 4.2. Simulated Device Performance of Perovskite Solar Cells.

Capping layer thickness (nm)	**J_{sc} (mA/cm^2)**	**V_{oc} (V)**	**Fill Factor**	**Efficiency (%)**	**Number of Recombination Events at MPP**	**τ_t (μs)**	**τ_r (μs)**
350	23.17	1.09	0.77	19.44	152	3.47	7.98
400	**24.09**	**1.11**	**0.78**	**20.85**	**205**	**2.14**	**8.32**
450	23.84	1.07	0.76	19.38	268	2.83	5.83
500	23.07	1.03	0.74	17.58	283	3.77	4.55

4.3 Variation of Morphological Parameters in Cell Fabrication

Perovskite solar cells were fabricated with varying of PbI_2 concentrations (to create variations in capping layer coverage), and also at an optimized PbI_2 concentration of 462 mg/ml at varying spin coating speeds (to create variations in capping layer thickness). The performance of the fabricated devices was then characterized as described in Chapter 3. This section presents the results obtained from those analyses.

4.3.1 Variation in PbI_2 Concentration

As mentioned earlier, capping layer coverages were fabricated through variation of the PbI_2 concentration when forming the perovskite film. XRD patterns were recorded to understand the effect of different PbI_2 concentration on perovskite crystallinity. Figure 4.6 (a-d) show the resulting XRD patterns of the films prepared at each concentration. The observed peaks at 14.08°, 28.41°, 31.85°, and 43.19° correspond to the (110), (220), (310), and (330) crystalline planes of $CH_3NH_3PbI_3$, confirming its tetragonal crystal structure [166, 167]. The (001) peak at 12.12° corresponds to PbI_2 [81, 166, 168]. The XRD results show that the perovskite crystallinity increased with increasing PbI_2 concentration. The 662 mg/ml samples have the largest peak at 12.12°, indicating more s PbI_2 is present. At concentrations greater than 462 mg/ml, the PbI_2 layer becomes more compact, potentially leading to an incomplete reaction of PbI_2 with CH_3NH_3I [169].

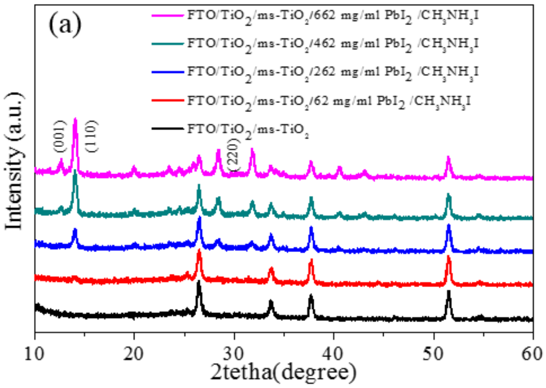

Figure 4.6. XRD Spectra of FTO / c-TiO_2 / m-TiO_2: Perovskite Films of Varying PbI_2 Concentration on Top of m-TiO_2

Figure 4.7 (a-o) show the AFM topography, AFM phase and the SEM images of FTO/compact TiO_2 /m-TiO_2/ perovskite films at varying PbI_2 concentrations. These images indicate that the gap between perovskite crystals decreases with increasing PbI_2 concentration, up to an “optimal” concentration of 462 mg/ml and formation of a homogenous perovskite capping layer. At higher PbI_2 concentrations, the gaps increase again, resulting in the formation of non-homogenous perovskite capping layers.

Comparison of the phase images of the m-TiO_2 film [Figure 4.7 (f)] and the perovskite films fabricated with lower PbI_2 concentrations (62 and 262 mg/ml) [Figure 4.7 (g) and (h)] shows partial capping layer coverage. A similar comparison can be made with the corresponding SEM images [Figure 4.7 (k) and Figure 4.7 (l) and (m)]. On the other hand, comparison of the images of the perovskite films at PbI_2 concentrations of 462 mg/ml or greater show full capping layer coverage. At a concentration of 662 mg/ml, the degree of non-homogeneity of the capping layer increases, resulting in an increase in film roughness that may hinder charge transport in the film and across the perovskite/charge transport layer interface. It has also been reported in previous analyses that the unreacted PbI_2 may act as a barrier for electron injection at the TiO_2/perovskite interface [169].

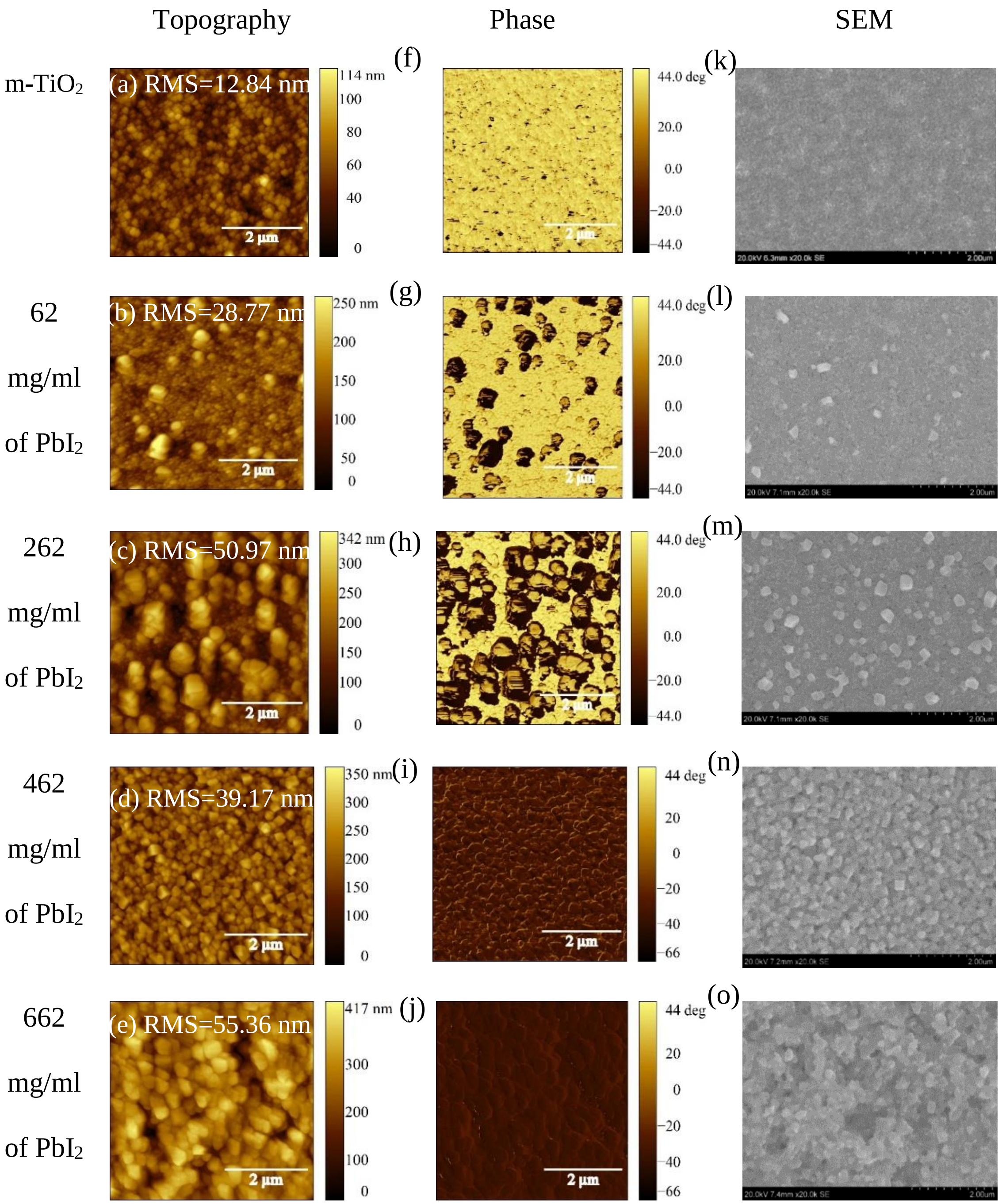

Figure 4.7. AFM and SEM Images of Fabricated Perovskite Films: (a-e) AFM Topography; (f-j) AFM Phase; (k-o) SEM images. Figures (a, f, k) are FTO/compact TiO_2/m-TiO_2; figures (b, g, l), (c, h, m), (d, i, n), and (e, j, o) are Perovskite Films on m-TiO_2 at PbI_2 concentrations of 62 mg/ml, 262 mg/ml, 462 mg/ml, and 662 mg/ml, respectively

Figure 4.8 (a-d) plot the measured performance of the cells fabricated with each PbI_2 concentration. Table 4.3 provides the corresponding numerical values for each performance parameter. J-V measurements of perovskites typically exhibit hysteresis effects between forward and reverse scans, which may be due to charge carriers trapping/detrapping, vacancy-assisted ion migrations [170-172]. Thus, the cells were characterized with both forward and reverse scans while switching the voltage. After increasing the PbI_2 concentration from 62 mg/ml to 462 mg/ml, the average forward scan/reverse scan efficiencies increased from approximately 3.55%/3.68% to 15.30%/18.36%. Interestingly, further increasing the PbI_2 concentration to 662 mg/ml led to a decrease in efficiency. While the higher PbI_2 concentration led to greater photon absorption as shown in Figure 4.9(a), it led to reduced carrier transport because of the increase in surface roughness [Figure 4.7(e)]; resulted in greater recombination of carriers before they could reach the carrier extraction layers. Thus, a homogenous and pin hole-free perovskite capping layer is critical for achieving good interface properties and photovoltaic performance [162-164]; 462 mg/ml of PbI_2 appears to be at or near the optimal concentration where these conditions can occur. The integrated J_{sc} from the external quantum efficiency (EQE) spectra in Figure 4.9 (b) is in good agreement with J_{sc} calculated from J-V characterization.

The TPC and TPV were measured as mentioned in section 3.5.3 for further insights into carrier transport. Figure 4.8(c) and (d) show the resulting TPC and TPV decay curves as a function of PbI_2 concentration. Note that the TPV decay does not reach a zero level in Figure 4.8 (d) due to the constant AM 1.5 background illumination on the cells during the measurement. Table 4.3 summarizes the observed values of photovoltaic parameters,

τ_t, and τ_r for perovskite solar cells prepared with a different concentration of PbI_2. The τ_t and τ_r of perovskite films prepared with a 462 mg/ml concentration are the shortest (2.44 µs) and longest (7.24 µs) respectively, indicating efficient carrier extraction in high-quality perovskite layer formation with a reduced number of potential traps. This is supported by the observed J_{sc} and V_{oc} for these cells. Meanwhile, the cell with 62 mg/ml showed the longest τ_t (approximately 7.49 µs) and the shortest τ_r (approximately 5.02 µs), due to the presence of more and larger gaps and pin-holes in the perovskite layer.

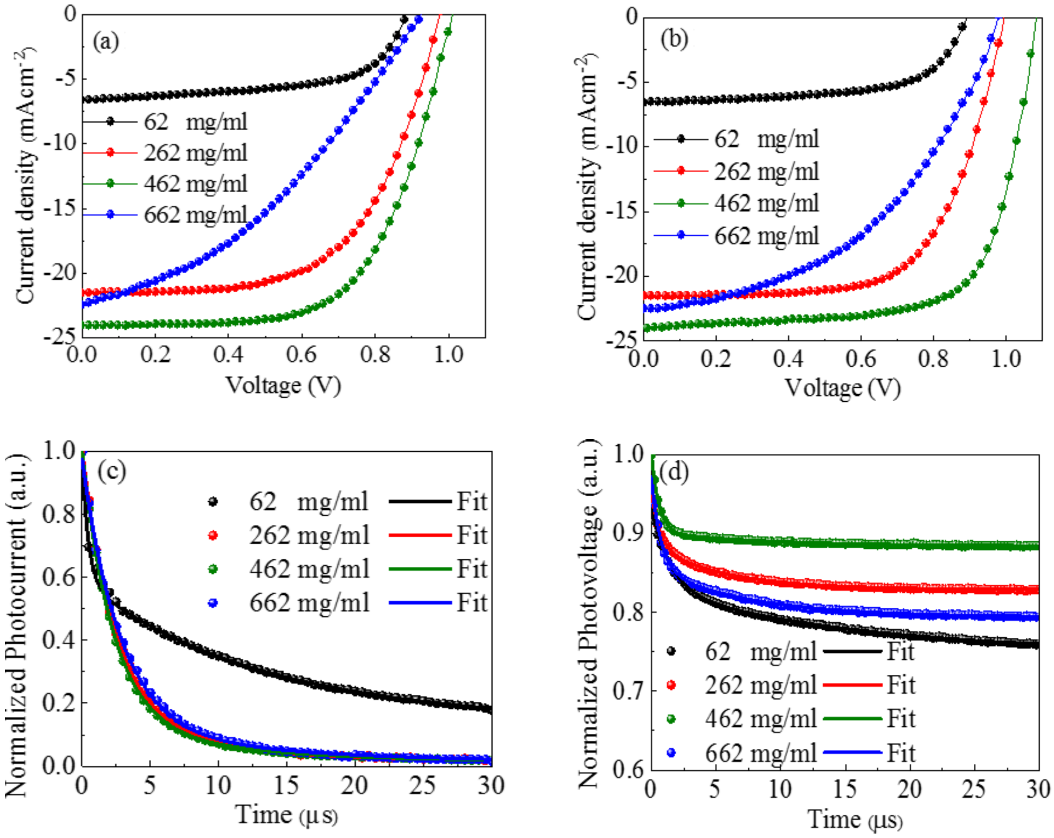

Figure 4.8. Measured Solar Cell Performance with Respect to PbI_2 Concentration: (a, b) Current Density-Voltage Characteristics (Forward Scan, Reverse Scan); (c) TPC Decay; (d) TPV Decay.

Table 4.3. Photovoltaic Parameters, Charge Transport Time and Charge Carrier Recombination Lifetime for Perovskite Solar Cells Prepared with Different PbI_2 Concentration.

Conc^n of PbI_2 (mg/ml)	**J_{sc} (mA/cm^2)**		**V_{oc} (V)**		**Fill Factor**		**Efficiency (%)**		**τ_t (μs)**	**τ_r (μs)**
	Fwd	Rev	Fwd	Reve	Fwd	Rev	Fwd	Rev		
62	6.65	6.59	0.89	0.90	0.60	0.62	3.55	3.68	7.49	5.02
262	21.58	21.59	0.98	1.00	0.60	0.65	12.61	13.93	4.85	5.69
462	**24.04**	**24.06**	**1.01**	**1.09**	**0.63**	**0.70**	**15.30**	**18.36**	**2.44**	**7.24**
662	22.47	22.55	0.93	0.98	0.37	0.46	7.73	10.19	4.34	5.09

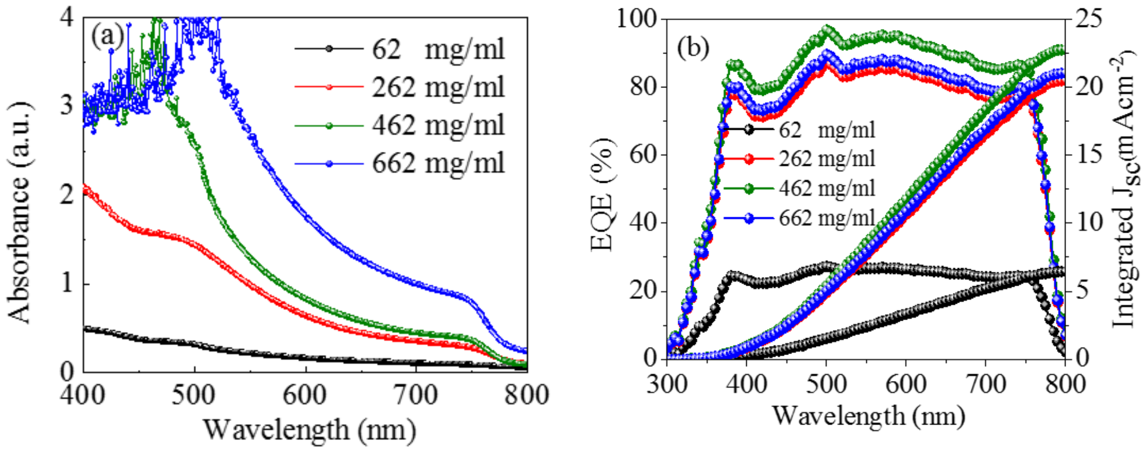

Figure 4.9. (a) UV-vis Absorbance Spectra; (b) EQE Spectra and Integrated Photocurrent Density J_{sc} of Perovskite Solar Cells Prepared with Different PbI_2 Concentrations.

4.3.2 Variation on Spin Coating Speed

Perovskite solar cells were also fabricated with varying capping layer thickness by changing spin coating speed at the “optimal” PbI_2 concentration of 462 mg/ml. As with preparation of cells with varying capping layer coverage, sequential deposition was used to prepare the perovskite films. Figure 4.10 (a-d) plot the J-V characteristics and the TPC and TPV decays of the $CH_3NH_3PbI_3$ perovskite solar cells fabricated with the PbI_2 films spin coated at speeds varying from 2000 rpm to 5000 rpm in steps of 1000 rpm, respectively. As measured with the Veeco DEKTAK 150 profilometer, the final capping layer thicknesses for these cells ranged from approximately 304 nm to 552 nm. The layer thickness appeared to be directly proportional to the spin speed; the thinner layers were created at faster spin speeds.

Figure 4.10 (c) and (d) show the measured TPC and TPV decays for the cells prepared with each capping layer thickness. As shown in Table 4.4, the τ_t and τ_r of perovskite films with the 380 nm thick capping layer are shortest and longest, respectively, showing efficient charge extraction and highest short circuit current, and circuit voltage. These results agree with the EQE and J-V measurements showing the maximum J_{sc} and V_{oc}; the highest device efficiency was achieved for the cell with the 380 nm thick capping layer. τ_t is the longest (6.31 μs) for the cell with 304 nm thickness, which, again, may be due to decreased photon absorption. In addition, the cell with the thickest capping layer (552 nm) has the shortest τ_r (4.79 μs) owing to more carrier recombination.

As shown in Table 4.4, the average efficiency was found to increase with an increase in the capping layer thickness from 304 nm to 380 nm, and decrease with further increases in the thickness to 457 nm and 552 nm. The cell with the 380 nm thick capping layer achieved the highest efficiency, approximately 18.36%, vs approximately 15.75% for the cell with the 304 nm thick capping layer. This improvement was observed in the other parameters as well; it can be attributed to the improved charge transport properties and reduced recombination. Figure 4.11 (a) shows the increase in photon absorption with increasing capping layer thickness. However, cells with a thickness exceeding the optimized thickness (380 nm) will suffer reduced charge transport; a longer charge carrier pathway leads to charge recombination before reaching the carrier extraction layers [173, 174]. The EQE spectra shown in Figure 4.11 (b) also supports these results, with integrated J_{sc} values in good agreement to those obtained from the J-V characteristic measurements.

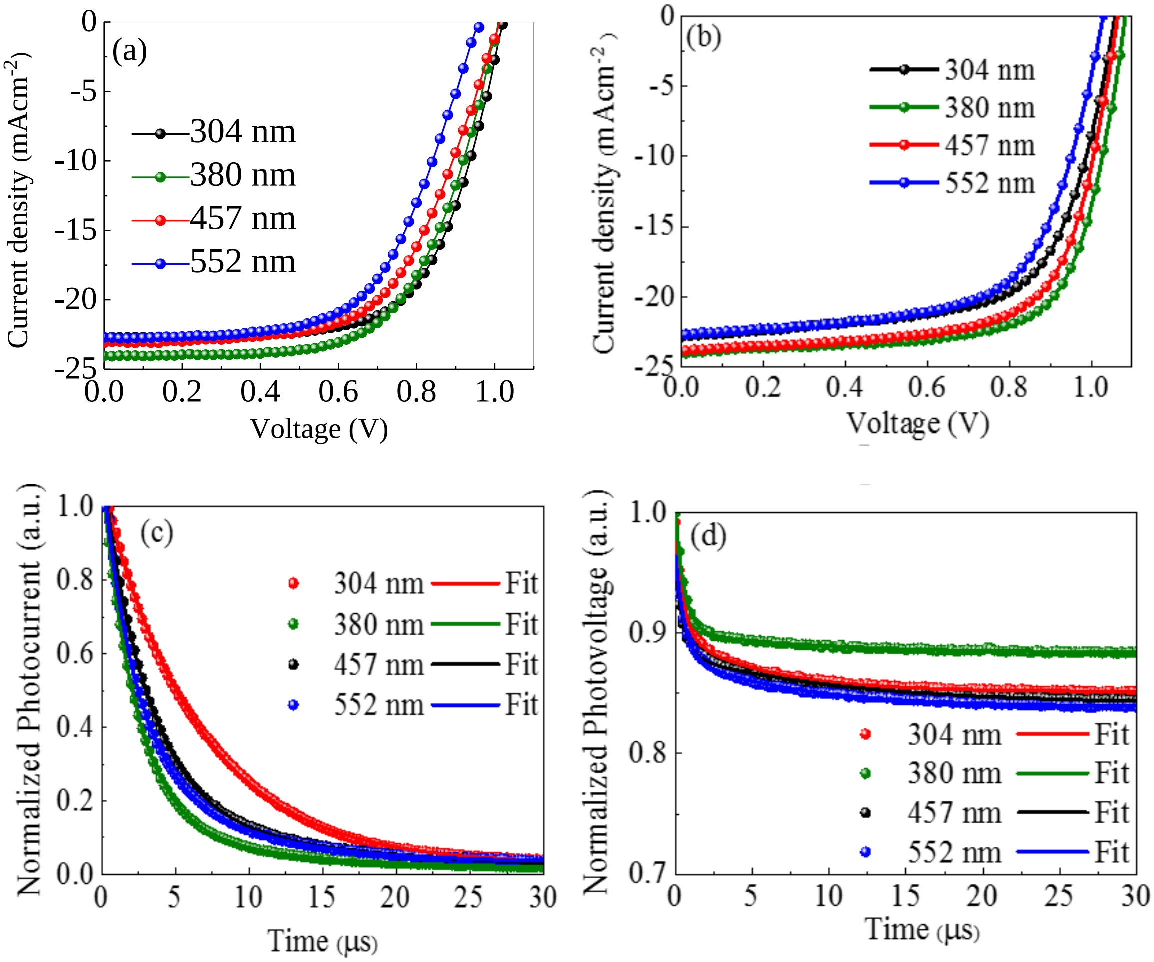

Figure 4.10. Measured Solar Cell Performance with Respect to Capping Layer Thickness: (a, b) Current Density-Voltage Characteristics (Forward Scan, Reverse Scan); (c) TPC Decay; (d) TPV Decay.

Table 4.4. Photovoltaic Parameters, Charge Transport Time and Charge Carrier Recombination Lifetime for Perovskite Solar Cells with Different Capping Layer Thickness.

Capping Layer Thickness (nm)	**J_{sc} (mA/cm^2)**		**V_{oc} (V)**		**Fill Factor**		**Efficiency (%)**		**τ_t (μs)**	**τ_r (μs)**
	Fwd	Rev	Fwd	Rev	Fwd	Rev	Fwd	Rev		
304	22.71	22.86	1.03	1.06	0.65	0.65	15.20	15.75	6.31	6.83
380	**24.04**	**24.06**	**1.01**	**1.09**	**0.63**	**0.70**	**15.30**	**18.36**	**2.44**	**7.24**
457	23.10	23.86	1.02	1.07	0.60	0.68	14.14	17.36	3.68	5.03
552	22.80	22.71	0.96	1.03	0.60	0.65	13.13	15.20	3.79	4.79

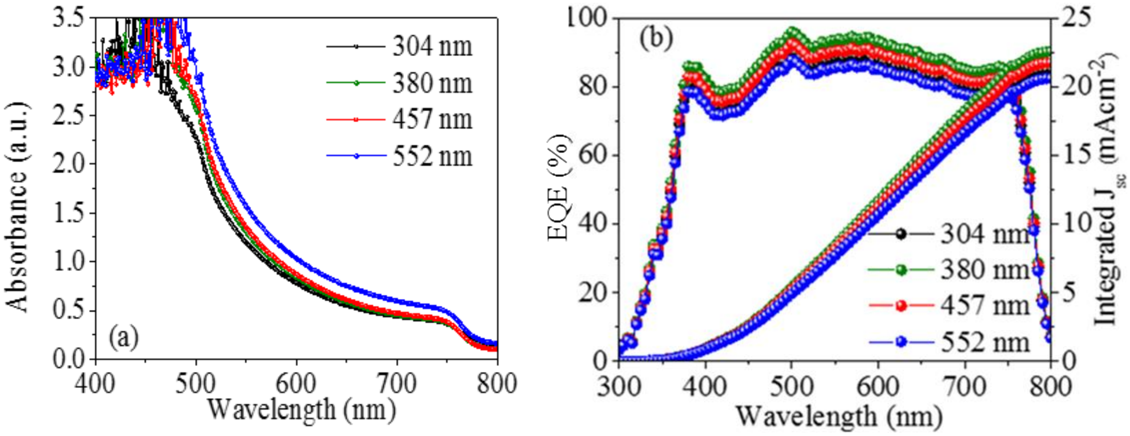

Figure 4.11. (a) UV-vis Absorbance Spectra; (b) EQE Spectra and Integrated Photocurrent Density J_{sc} of Perovskite Solar Cells Prepared with Different Capping Layer Thicknesses.

Figure 4.12 showed the efficacy of 12 perovskite cells with optimized PbI_2 concentration (462 mg/ml) and capping layer thickness (370 nm).

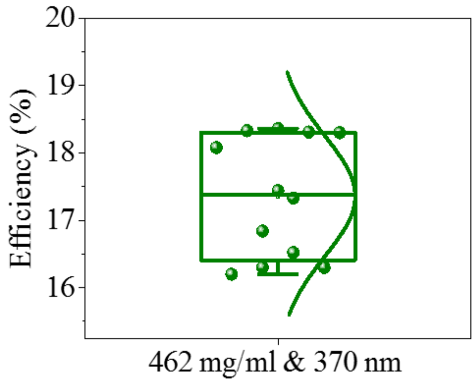

Figure 4.12. Statistics of Efficiency for Perovskite Solar Cell with Optimized PbI_2 Concentration and Capping Layer Thickness

4.4 Comparison of Simulated and Experimental Results

This section directly compares the simulation predictions and experimental results achieved for the fabricated solar cells with respect to variations in capping layer coverage and thickness. Table 4.7Table 4.8 summarize the corresponding simulation and experimental parameters.

Table 4.5 shows the thickness of compact-TiO_2, mesouporous-TiO_2, and spiro-OMeTAD used for studying capping layer morphology and perovskite thickness. Table 4.6 shows the thickness parameters of perovskite capping layer with considering different spin coating speed.

Table 4.5. Compact-TiO_2, mesoporous-TiO_2, and spiro-OMeTAD Layer Thicknesses Used for Studying Capping Layer Coverage and Thickness of Perovskite

	Experiment (nm)	**Simulation (nm)**
compact-TiO_2	49±3	50
mesoporous-TiO_2	252±8	250
spiro-OMeTAD	206±6	200

Table 4.6. Perovskite Capping Layer Thickness Parameters

Experiment (462 mg/ml PbI_2 solution)			**Simulation (100% coverage capping layer)**
Spin speed (rpm)	Duration (s)	Thickness (nm)	Thickness (nm)
5000	40	304±10	350
4000	40	380±9	400
3000	40	457±11	450
2000	40	552±16	500

4.4.1 Simulated / Experimental Capping Layer Coverage Comparison

Table 4.7 gives the performance parameters for the simulated and fabricated cells. Perovskite solar cells with a homogenous and the pinhole-free capping layer (100% coverage) were found to perform at maximum efficiency in simulation. Similar maximum performance efficiency was observed in physical devices fabricated with a PbI_2 concentration of approximately 462 mg/ml. Under these simulated and physical conditions, the shortest τ_t and longest τ_r were observed.

Table 4.7. Simulated / Measured Performance Capping Layer Coverage Comparison.

	(a) Simulation Results			
S. No.	**Coverage of capping layer (%)**	**PCE (%)**	**τ_t (µs)**	**τ_r (µs)**
1	85	13.84	4.16	5.95
2	90	15.04	4.11	6.15
3	95	17.5	3.21	6.56
4	**100**	**20.85**	**2.14**	**8.32**

	(b) Experimental Results			
S. No.	**Approx. Coverage of capping layer (%)**	**PCE (%)**	**τ_t (µs)**	**τ_r (µs)**
1	45-50 (62 mg/ml of PbI_2)	3.68	7.49	5.02
2	85-90 (262 mg/ml of PbI_2)	13.93	4.85	5.69
3	**95-100 (462 mg/ml of PbI_2)**	**18.36**	**2.44**	**7.24**
4	95-100 (662 mg/ml of PbI_2)	10.19	4.34	5.09

Figure 4.13 (a-c) plot the efficiencies, τ_t, and τ_r vs percentage of capping layer coverage. The observed behavior for these parameters is consistent with the simulated results. However, the perovskite solar cell fabricated with the 662 mg/ml concentration did not follow the trend; the high crystallinity of perovskite at the 662 mg/ml concentration resulted in a non-homogenous perovskite layer (as shown in Figure 4.7 (e) & (o)).

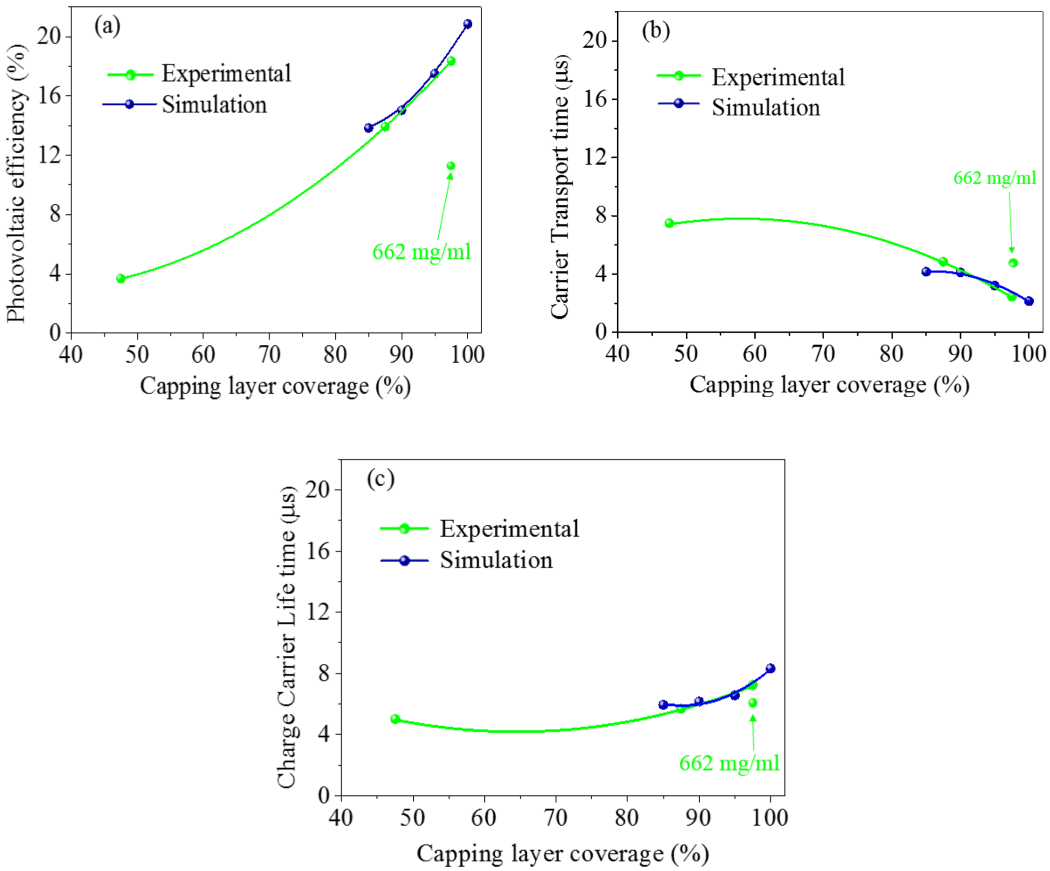

Figure 4.13. Simulated / Measured Performance Comparison with Respect to Capping Layer Coverage: (a) Efficiencies; (b) Charge Transport Time; (c) Charge Carrier Recombination Lifetime

4.4.2 Simulated / Experimental Capping Layer Thickness Comparison

Simulation and experimental results include the efficiencies, $\tau_{t,}$ and τ_r of solar cells simulated with different capping layer thickness and solar cells fabricated with different spin speeds from 2000 rpm to 5000 rpm at a step of 1000 rpm (as shown in Table 4.8). Figure 4.14 shows the comparison of efficiencies, $\tau_{t,}$ and τ_r from simulation and experimental results. Perovskite solar cells with a capping layer thickness of approximately 400 nm were found to perform at maximum efficiency in simulation. Similar maximum performance efficiency was observed in physical devices fabricated with a capping layer thickness of approximately 380 nm produced at a spin speed of 4000 rpm. Under these conditions, as shown in Figure 4.14 (b) and (c), the shortest τ_t and longest τ_r were observed. As with capping layer coverage, the measured efficiencies, τ_t and τ_r responses as a function of capping layer thickness were consistent with the simulated results.

Table 4.8. Simulated / Measured Performance Capping Layer Thickness Comparison

	(a) Simulation Results				**(b) Experimental Results**				
S. No.	**Thickness of capping layer (nm)**	**PCE (%)**	τ_t **(μs)**	τ_r **(μs)**	**Spin Coating speed (rpm)**	**Thickness of capping layer (nm)**	**PCE (%)**	τ_t **(μs)**	τ_r **(μs)**
1	350	19.44	3.47	7.98	5000	304	15.75	6.31	6.83
2	**400**	**20.85**	**2.14**	**8.32**	**4000**	**380**	**18.36**	**2.44**	**7.24**
3	450	19.38	2.83	5.83	3000	457	17.36	3.68	5.03
4	500	17.58	3.77	4.55	2000	552	15.20	3.79	4.79

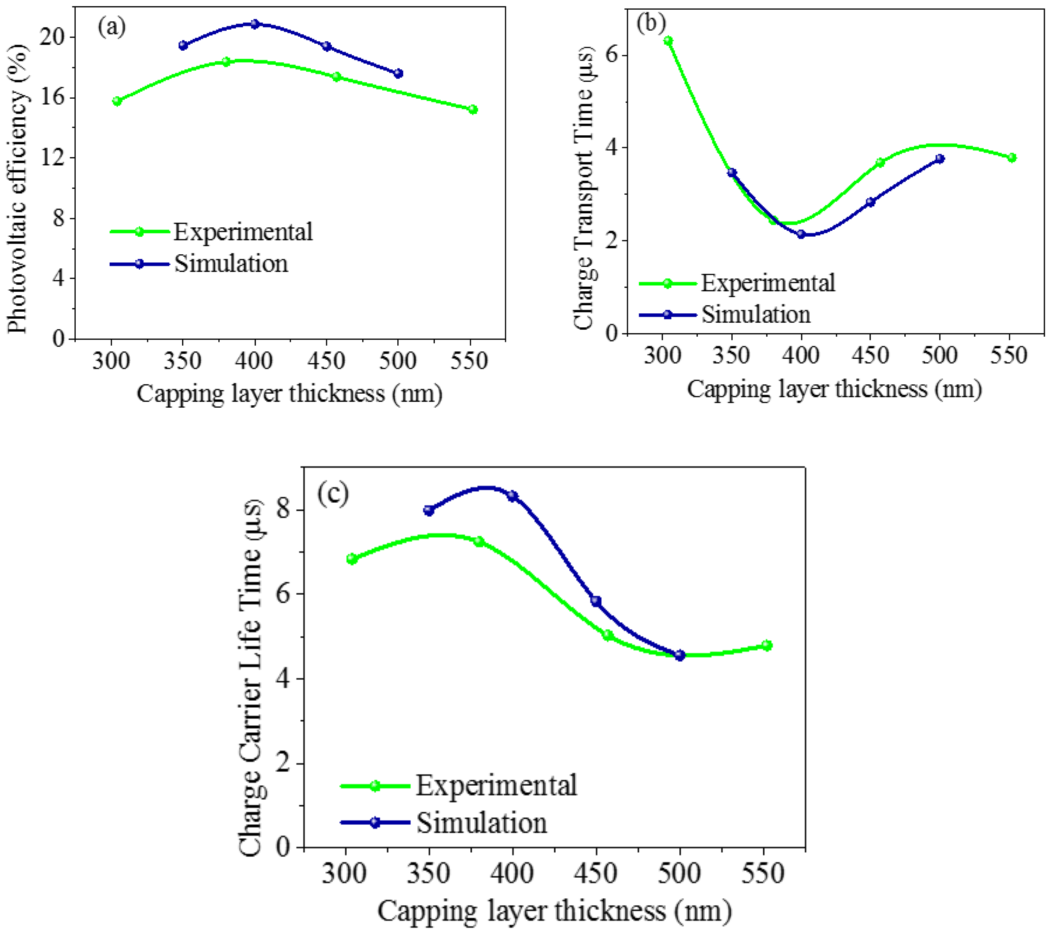

Figure 4.14. Simulated / Measured Performance Comparison with Respect to Capping Layer Thickness: (a) Efficiencies; (b) Charge Transport Time; (c) Charge Carrier Recombination Lifetime

Chapter 5: Summary and Conclusions

5.1 Summary

Demand for renewable and environmentally friendly energy sources is increasing, as is the need to reduce carbon dioxide emissions and avoid depletion of fossil fuel resources. Solar energy has become a potential alternative energy source due to its abundance and negligible environmental impacts. Solar cells which convert sunlight to electrical energy provide a promising approach to harnessing this energy. However, their contributions to current energy production remain limited due to the higher cost of fabricating crystalline silicon solar cells of the required purity. Perovskite solar cells have generated much interest as a potential replacement for silicon solar cells due to their lower fabrication costs and greater efficiencies.

The hybrid lead halide perovskite is a promising material in photovoltaic technology. Within the past ten years, the power conversion efficency (PCE) of perovskite solar cells has drastically increased from 3.8% to 22.7%, approaching the efficiencies achievable with current silicon cell technologies [81-84]. Due to these recent developments the basic device physics and performance characteristics, represented by the PCE and charge carrier dynamics, are not well understood [25, 26]. Rigorous computer-based modeling can obtain this information, enabling fabrication of devices with even greater PCE at significantly reduced costs.

As mentioned earlier, adequate simulation of 3D perovskite solar cell morphology and performance cannot be performed using current 1D and 2D models based on closed-form solutions of partial differential equations. Probabilistic/statistical approaches based on Monte Carlo (MC) simulations have shown great promise for this type of modeling [63]. The time-dependent KMC method produces more realistic models by modeling all physically possible transitions between states [68, 69]. As a result, this method is considered a useful tool for investigating all current solar cell technologies [73-76, 78, 79]. However, no research has been reported on the modeling and simulation of a complete perovskite solar cell using the KMC approach.

This thesis presents the results of work characterizing perovskite solar cell morphology and performance using KMC simulation. The basic morphology of a mesoscopic, methylammonium lead iodide ($CH_3NH_3PbI_3$) perovskite solar cell was developed. The effects of capping layer coverage and thickness on cell performance were investigated. Cells were fabricated with varying PbI_2 concentration and multiple spin coating speeds, and their performance characteristics were measured and compared to the model predictions.

5.2 Conclusions

The KMC simulation model developed for mesoscopic perovskite solar cells could successfully characterize the variation in performance parameters due to variation of morphological parameters such as the capping layer coverage and thickness. The simulations predicted a maximum PCE of approximately 20.85% for a perovskite film with 100% capping layer coverage and thickness of 400 nm. With this configuration, the simulations predicted a minimum charge transport time (τ_t) and maximum charge carrier recombination lifetime (τ_r). In general, the simulations predicted that for increasing capping layer coverage, the number of recombination events at the maximum power point (MPP) in the J-V characteristic and τ_t decreases, while τ_r increases. As the capping layer thickness increased, the number of recombination events at MPP decreased while τ_t and τ_r exhibited nonlinear behavior.

The performance of cells fabricated with varying concentrations of PbI_2 and spin coating speeds agreed with the corresponding model simulations. The best performance was observed for the fabricated cell with approximately 100% capping layer coverage (462 mg/ml of PbI_2) and thickness of approximately 380 nm (spin coated at 4000 rpm). The measured PCE was approximately 18.35%. As predicted in the simulations, the measured τ_t and τ_r of this perovskite cell were found to be the shortest and longest, respectively.

The measured performance of perovskite solar cells fabricated with a PbI_2 concentration of 662 mg/ml (corresponding to an approximately 100% capping layer coverage) performed worse than the cells fabricated from a 462 mg/ml concentration, suggesting the existence of an "optimal" concentration. This is most likely due to un-reacted PbI_2 hindering charge transport in the film and across the perovskite/charge transport layer.

5.3 Future work

The KMC models could be enhanced in a number of ways. First, the modeling could be extended to cover additional recombination event types and the existence of trap states. Second, this work could be extended to other perovskite material systems by incorporating related information about energetic disorder and morphology. Third, modeling was performed assuming a single cell; tandem solar cell modeling could be developed by cascading individual cell models and characterizing the resulting behavior at the interface(s); initial research into such devices (both Si and perovskite based) found higher photovoltaic efficiencies were indeed possible with this configuration.

References

1. energy, M.c.-o. *Green Energy*. 2017; Available from: https://www.cooperativeenergy.coop/customer-service/frequently-asked-questions/green-energy/green-energy-faqs/when-will-fossil-fuels-run-out/.
2. Change, F.F.A.C. *The Science of Climate Change*. 2018; Available from: https://www.nwf.org/Eco-Schools-USA/Become-an-Eco-School/Pathways/Climate-Change/Facts.aspx.
3. Organization, W.H. *Ambient (outdoor) air quality and health*. 2018; Available from: http://www.who.int/news-room/fact-sheets/detail/ambient-(outdoor)-air-quality-and-health.
4. Agency, I.E. *History*. 2018; Available from: https://www.iea.org/about/history/.
5. Agency, I.E. *Solar leads the charge in another record year for renewables*. 2017; Available from: https://www.iea.org/publications/renewables2017/.
6. Guardian, T. *Solar power growth leaps by 50% worldwide thanks to US and China*. Available from: https://www.theguardian.com/environment/2017/mar/07/solar-power-growth-worldwide-us-china-uk-europe.
7. Scientists, U.o.C. *How Solar Energy Works*. Available from: https://www.ucsusa.org/clean-energy/renewable-energy/how-solar-energy-works#.W_C5NzhKi70.
8. NREL, *Best Research-Cell Efficiencies.* 2018.
9. Green, M.A., et al., *Solar cell efficiency tables (Version 45).* Progress in photovoltaics: research and applications, 2015. **23**(1): p. 1-9.
10. Chopra, K., P. Paulson, and V. Dutta, *Thin‐film solar cells: an overview*. Progress in Photovoltaics: Research and applications, 2004. **12**(2‐3): p. 69-92.
11. Messenger, R.A. and A. Abtahi, *Photovoltaic systems engineering*. 2010: CRC press.
12. Kaur, M. and H. Singh, *A review: comparison of silicon solar cells and thin film solar cells.* International Journal Of Core Engineering & Management, 2016. **3**(2): p. 15-23.
13. Andersson, B.A., *Materials availability for large‐scale thin‐film photovoltaics.* Progress in photovoltaics: research and applications, 2000. **8**(1): p. 61-76.
14. Dubey, A., et al., *A strategic review on processing routes towards highly efficient perovskite solar cells.* Journal of Materials Chemistry A, 2018. **6**(6): p. 2406-2431.
15. Li, X., et al., *A vacuum flash–assisted solution process for high-efficiency large-area perovskite solar cells.* Science, 2016: p. aaf8060.
16. Jeon, N.J., et al., *Compositional engineering of perovskite materials for high-performance solar cells.* Nature, 2015. **517**(7535): p. 476.
17. Jeon, N.J., et al., *A fluorene-terminated hole-transporting material for highly efficient and stable perovskite solar cells.* Nature Energy, 2018. **3**(8): p. 682-689.
18. Kojima, A., et al., *Organometal halide perovskites as visible-light sensitizers for photovoltaic cells.* Journal of the American Chemical Society, 2009. **131**(17): p. 6050-6051.

19. Im, J.-H., et al., *6.5% efficient perovskite quantum-dot-sensitized solar cell.* Nanoscale, 2011. **3**(10): p. 4088-4093.
20. Yang, W.S., et al., *High-performance photovoltaic perovskite layers fabricated through intramolecular exchange.* Science, 2015. **348**(6240): p. 1234-1237.
21. Saliba, M., et al., *Incorporation of rubidium cations into perovskite solar cells improves photovoltaic performance.* Science, 2016. **354**(6309): p. 206-209.
22. Van Noorden, R., *Cheap solar cells tempt businesses.* Nature, 2014. **513**(7519): p. 470-470.
23. Oxford, P., *Reveals breakthrough in efficiency of new class of solar cell*. 2013.
24. Wang, U., *Perovskite Offers Shot at Cheaper Solar Energy.* The Wall Street Journal. Retrieved 7 May 2015, 2014.
25. Sum, T.C. and N. Mathews, *Advancements in perovskite solar cells: photophysics behind the photovoltaics.* Energy & Environmental Science, 2014. **7**(8): p. 2518-2534.
26. Jung, H.S. and N.G. Park, *Perovskite solar cells: from materials to devices.* Small, 2015. **11**(1): p. 10-25.
27. Inc., C. *Comsol products* Multiphysics software product suite 2015 [cited 2015 03/19/2015]; Available from: http://www.comsol.com/products.
28. Mathworks. *SIMULINK*. Simulation and Model-Based Design 2015 [cited 2015 03/30/2015]; Available from: http://www.mathworks.com/products/simulink/.
29. Australia, U. *PC1D- Software for modelling a solar cell*. 2014.
30. Gagliardi, A. and A. Abate, *Mesoporous Electron-Selective Contacts Enhance the Tolerance to Interfacial Ion Accumulation in Perovskite Solar Cells.* ACS Energy Letters, 2018. **3**(1): p. 163-169.
31. Wikipedia. *Kinetic Monte Carlo*. 2015 [cited 2015 03/20/2015]; Available from: http://en.wikipedia.org/wiki/Kinetic_Monte_Carlo.
32. Khanal, B., et al. *Modelling of Solid Electrolyte Interface (SEI) Layer of Lithium-ion Batteries Using Kinetic Monte Carlo Approach*. in *IIE Annual Conference. Proceedings*. 2017. Institute of Industrial and Systems Engineers (IISE).
33. Ohl, R.S., *Light-sensitive electric device*. 1946, Google Patents.
34. Chapin, D., C. Fuller, and G. Pearson, *A new silicon p-n junction photocell for converting solar radiation into electrical power.* Journal of Applied Physics, 1954(25): p. 676-677.
35. Gereth, R., *Contribution to Silicon Solar Cell Technology* Energy Conversion, 1972. **12**: p. 103-107.
36. Carlson, D.E. and C.R. Wronski, *Amorphous silicon solar cell.* Applied Physics Letters, 1976. **28**(11): p. 671-673.
37. Zhao, J., et al., *19.8% efficient "honeycomb" textured multicrystalline and 24.4% monocrystalline silicon solar cells.* Applied Physics Letters, 1998. **73**(14): p. 1991-1993.
38. Uda, H., et al., *Polycrystalline thin film CdS/CdTe solar cells.* Japanese Journal of Applied Physics, 1978. **17**: p. 585.
39. Edoff, M., *Thin film solar cells: research in an industrial perspective.* Ambio, 2012. **41**(2): p. 112-118.
40. Hall, R.B. and J.D. Meakin, *The design and fabrication of high efficiency thin film CdS/Cu 2 S solar cells.* Thin Solid Films, 1979. **63**(1): p. 203-211.

41. Tang, C.W., *Two-layer organic photovoltaic cell.* Applied Physics Letters, 1986. **48**(2): p. 183-185.
42. Yu, G., et al., *Polymer photovoltaic cells: enhanced efficiencies via a network of internal donor-acceptor heterojunctions.* Science-AAAS-Weekly Paper Edition, 1995. **270**(5243): p. 1789-1790.
43. Li, G., et al., *High-efficiency solution processable polymer photovoltaic cells by self-organization of polymer blends*, in *Materials For Sustainable Energy: A Collection of Peer-Reviewed Research and Review Articles from Nature Publishing Group*. 2011, World Scientific. p. 80-84.
44. He, Z., et al., *Enhanced power-conversion efficiency in polymer solar cells using an inverted device structure.* Nature Photonics, 2012. **6**(9): p. 591-595.
45. You, J., et al., *A polymer tandem solar cell with 10.6% power conversion efficiency.* Nature communications, 2013. **4**: p. 1446.
46. O'regan, B. and M. Grätzel, *A low-cost, high-efficiency solar cell based on dye-sensitized colloidal TiO2 films.* 1991.
47. Green, M.A., A. Ho-Baillie, and H.J. Snaith, *The emergence of perovskite solar cells.* Nature Photonics, 2014. **8**(7): p. 506-514.
48. Liu, M., M.B. Johnston, and H.J. Snaith, *Efficient planar heterojunction perovskite solar cells by vapour deposition.* Nature, 2013. **501**(7467): p. 395-398.
49. Lee, M.M., et al., *Efficient hybrid solar cells based on meso-superstructured organometal halide perovskites.* Science, 2012. **338**(6107): p. 643-647.
50. Stranks, S.D., et al., *Electron-hole diffusion lengths exceeding 1 micrometer in an organometal trihalide perovskite absorber.* Science, 2013. **342**(6156): p. 341-344.
51. Mei, A., et al., *A hole-conductor–free, fully printable mesoscopic perovskite solar cell with high stability.* Science, 2014. **345**(6194): p. 295-298.
52. Noh, J.H., et al., *Chemical management for colorful, efficient, and stable inorganic–organic hybrid nanostructured solar cells.* Nano letters, 2013. **13**(4): p. 1764-1769.
53. Xing, G., et al., *Long-range balanced electron-and hole-transport lengths in organic-inorganic CH3NH3PbI3.* Science, 2013. **342**(6156): p. 344-347.
54. Kim, H.-S., et al., *Lead iodide perovskite sensitized all-solid-state submicron thin film mesoscopic solar cell with efficiency exceeding 9%.* Scientific reports, 2012. **2**.
55. Burschka, J., et al., *Sequential deposition as a route to high-performance perovskite-sensitized solar cells.* Nature, 2013. **499**(7458): p. 316.
56. Ahn, N., et al., *Highly reproducible perovskite solar cells with average efficiency of 18.3% and best efficiency of 19.7% fabricated via Lewis base adduct of lead (II) iodide.* Journal of the American Chemical Society, 2015. **137**(27): p. 8696-8699.
57. Yang, W.S., et al., *Iodide management in formamidinium-lead-halide–based perovskite layers for efficient solar cells.* Science, 2017. **356**(6345): p. 1376-1379.
58. Foster, J.M., et al., *A Model for the Operation of Perovskite Based Hybrid Solar Cells: Formulation, Analysis, and Comparison to Experiment.* SIAM Journal on Applied Mathematics, 2014. **74**(6): p. 1935-1966.
59. Sun, X., et al., *A Physics-Based Analytical Model for Perovskite Solar Cells.* Photovoltaics, IEEE Journal of, 2015. **5**(5): p. 1389-1394.

60. Zhou, Y. and A. Gray-Weale, *A numerical model for charge transport and energy conversion of perovskite solar cells.* Physical Chemistry Chemical Physics, 2016. **18**(6): p. 4476-4486.
61. Fu, K., et al., *The simulation of physical mechanism for HTM-free perovskite organic lead iodide planar heterojunction solar cells.* Journal of Optics, 2015. **17**(10): p. 105904.
62. Zhou, Q., et al., *Two-dimensional device modeling of CH3NH3PbI3 based planar heterojunction perovskite solar cells.* Solar Energy, 2016. **123**: p. 51-56.
63. Gagliardi, A. and A. Abate, *Mesoporous electron-selective contacts enhance the tolerance to interfacial ion accumulation in perovskite solar cells.* ACS Energy Letters, 2017. **3**(1): p. 163-169.
64. Liu, F., et al., *Numerical simulation: toward the design of high-efficiency planar perovskite solar cells.* Applied Physics Letters, 2014. **104**(25): p. 253508.
65. Wang, Y., et al., *Towards printed perovskite solar cells with cuprous oxide hole transporting layers: a theoretical design.* Semiconductor Science and Technology, 2015. **30**(5): p. 054004.
66. Sherkar, T.S., et al., *Recombination in perovskite solar cells: significance of grain boundaries, interface traps, and defect ions.* ACS energy letters, 2017. **2**(5): p. 1214-1222.
67. Wang, H.Y., et al., *Multiple‐Trapping Model for the Charge Recombination Dynamics in Mesoporous‐Structured Perovskite Solar Cells.* ChemSusChem, 2017. **10**(24): p. 4872-4878.
68. Fichthorn, K.A. and W.H. Weinberg, *Theoretical foundations of dynamical Monte Carlo simulations.* The Journal of chemical physics, 1991. **95**(2): p. 1090-1096.
69. Kroese, D.P., et al., *Why the Monte Carlo method is so important today.* Wiley Interdisciplinary Reviews: Computational Statistics, 2014. **6**(6): p. 386-392.
70. Groves, C. and N.C. Greenham, *Bimolecular recombination in polymer electronic devices.* Physical Review B, 2008. **78**(15).
71. Deibel, C., T. Strobel, and V. Dyakonov, *Origin of the Efficient Polaron-Pair Dissociation in Polymer-Fullerene Blends.* Physical Review Letters, 2009. **103**(3).
72. Korolev, N.A., V.R. Nikitenko, and A.P. Tyutnev, *Numerical simulation of time-dependent geminate recombination in polymers.* Semiconductors, 2010. **44**(8): p. 912-918.
73. Meng, L., et al., *Dynamic Monte Carlo Simulation for Highly Efficient Polymer Blend Photovoltaics.* The Journal of Physical Chemistry B, 2010. **114**(1): p. 36-41.
74. Meng, L., et al., *An improved dynamic Monte Carlo model coupled with Poisson equation to simulate the performance of organic photovoltaic devices.* The Journal of chemical physics, 2011. **134**(12): p. 124102.
75. Baidya, P.M., et al., *Kinetic Monte Carlo modeling of dark and illuminated current-voltage characteristics of bulk heterojunction solar cells.* Applied Physics Letters, 2013. **103**(6): p. 063305.
76. Pelzer, K.M. and S.B. Darling, *Charge generation in organic photovoltaics: a review of theory and computation.* Molecular Systems Design & Engineering, 2016. **1**(1): p. 10-24.

77. Neupane, U., et al., *Kinetic Monte Carlo modeling on organic solar cells: Domain size, donor-acceptor ratio and thickness.* Nano energy, 2017. **35**: p. 128-137.
78. Muralidharan, P., et al. *A kinetic Monte Carlo approach to study transport in amorphous silicon/crystalline silicon HIT cells*. in *Photovoltaic Specialist Conference (PVSC), 2015 IEEE 42nd*. 2015. IEEE.
79. Muralidharan, P., et al. *Multiscale modeling of silicon heterojunction solar cells*. in *Photovoltaic Specialists Conference (PVSC), 2016 IEEE 43rd*. 2016. IEEE.
80. El Yadari, M., et al., *Monte Carlo study of the double perovskite nano Sr 2 VMoO 6.* Journal of Alloys and Compounds, 2013. **579**: p. 86-91.
81. Dymshits, A., et al., *The electronic structure of metal oxide/organo metal halide perovskite junctions in perovskite based solar cells.* Scientific reports, 2015. **5**.
82. Lin, K.-F., et al., *Unraveling the high performance of tri-iodide perovskite absorber based photovoltaics with a non-polar solvent washing treatment.* Solar Energy Materials and Solar Cells, 2015. **141**: p. 309-314.
83. Mabrouk, S., et al., *Increased efficiency for perovskite photovoltaics via doping the PbI2 layer.* The Journal of Physical Chemistry C, 2016. **120**(43): p. 24577-24582.
84. NREL. *Best Research-Cell Efficiencies*. 2018 [cited 2018 01/01]; Available from: https://www.nrel.gov/pv/assets/images/efficiency-chart.png.
85. Mabrouk, S., et al., *Dithieno [3, 2-b: 2', 3'-d] pyrrole-based hole transport materials for perovskite solar cells with efficiencies over 18%.* Journal of Materials Chemistry A, 2018. **6**(17): p. 7950-7958.
86. Elbohy, H., et al., *Tuning Hole Transport Layer Using Urea for High‐Performance Perovskite Solar Cells.* Advanced Functional Materials, 2018: p. 1806740.
87. Gaml, E.A., et al., *Alternative benzodithiophene (BDT) based polymeric hole transport layer for efficient perovskite solar cells.* Solar Energy Materials and Solar Cells, 2017. **168**: p. 8-13.
88. Chandrasekhar, P., et al., *Higher efficiency perovskite solar cells using Au@ SiO 2 core–shell nanoparticles.* Sustainable Energy & Fuels, 2018. **2**(10): p. 2260-2267.
89. Gong, J., S.B. Darling, and F. You, *Perovskite photovoltaics: life-cycle assessment of energy and environmental impacts.* Energy & Environmental Science, 2015. **8**(7): p. 1953-1968.
90. Fonash, S., *Solar cell device physics*. 1981: Access Online via Elsevier.
91. Nelson, J. and M. Ratner, *The physics of solar cells*. Physics Today. Vol. 57. 2004. 71-71.
92. Kasap, S.O., *Principles of electronic materials and devices*. Vol. 81. 2006: McGraw-Hill New York, NY.
93. Jackson, R.K., et al., *The technical and broader societal impact of organic photovoltaics.* 2008 Ieee International Symposium on Electronics and the Environment, 2008: p. 407-407.
94. Jansson, F., et al., *Effect of electric field on diffusion in disordered materials.* Annalen Der Physik, 2009. **18**(12): p. 856-862.

95. Adhikari, N., *Nanoscale Study of Perovskite Solar Cells for Efficient Charge Transport.* 2016.
96. Nelson, J., *The Physics of Solar Cells*. 2003, London: Imperial College Press.
97. JEONG, J. *PHOTOVOLTAICS: Measuring the 'Sun'*. 2009.
98. C. Honsberg, S.B. *Quantum Efficiency*. February 3, 2015]; Available from: http://pveducation.org/pvcdrom/solar-cell-operation/quantum-efficiency.
99. Rose, G., *Beschreibung einiger neuen Mineralien des Urals.* Annalen der Physik, 1839. **124**(12): p. 551-573.
100. Navrotsky, A. and D.J. Weidner, *Perovskite: a structure of great interest to geophysics and materials science.* Washington DC American Geophysical Union Geophysical Monograph Series, 1989. **45**.
101. Mabrouk, S., et al., *Higher efficiency perovskite solar cells using additives of LiI, LiTFSI and BMImI in the PbI 2 precursor.* Sustainable Energy & Fuels, 2017. **1**: p. 2162-2171.
102. Snaith, H.J., *Perovskites: the emergence of a new era for low-cost, high-efficiency solar cells.* The Journal of Physical Chemistry Letters, 2013. **4**(21): p. 3623-3630.
103. Shi, E., et al., *Two-dimensional halide perovskite nanomaterials and heterostructures.* Chemical Society Reviews, 2018.
104. Chang, S.H., et al., *Optical, Excitonic, and Electronic Properties of CH3NH3PbI3 Thin Films and Their Application in Photovoltaics*, in *Perovskite Materials-Synthesis, Characterisation, Properties, and Applications*. 2016, InTech.
105. Pellet, N., *Investigations on hybrid organic-inorganic perovskites for high performance solar cells.* 2017.
106. Mora-Seró, I., *How Do Perovskite Solar Cells Work?* Joule, 2018. **2**(4): p. 585-587.
107. Evasari, E.R., *Electrical Modeling of Perovskite Solar Cells*. 2018.
108. Neupane, U., *A Kinetic Monte Carlo Study of Morphology Dependence of Bulk Heterojunction Solar Cells on JV Behavior.* 2015.
109. Popov, A., *Disordered semiconductors: physics and applications*. 2010: Pan Stanford.
110. Bisquert, J., *Interpretation of electron diffusion coefficient in organic and inorganic semiconductors with broad distributions of states.* Physical Chemistry Chemical Physics, 2008. **10**(22): p. 3175-3194.
111. Yin, W.J., et al., *Origin of high electronic quality in structurally disordered CH3NH3PbI3 and the passivation effect of Cl and O at grain boundaries.* Advanced Electronic Materials, 2015. **1**(6).
112. Yin, W.-J., et al., *Halide perovskite materials for solar cells: a theoretical review.* Journal of Materials Chemistry A, 2015. **3**(17): p. 8926-8942.
113. Landi, G., et al., *Correlation between electronic defect states distribution and device performance of perovskite solar cells.* Advanced Science, 2017. **4**(10): p. 1700183.
114. Shao, Y., Y. Yuan, and J. Huang, *Correlation of energy disorder and open-circuit voltage in hybrid perovskite solar cells.* Nature Energy, 2016. **1**: p. 15001.
115. Bässler, H., *Charge transport in disordered organic photoconductors a Monte Carlo simulation study.* physica status solidi (b), 1993. **175**(1): p. 15-56.

116. Choy, W.C.H., *Organic Solar Cells*, in *Materials and Device Physics*. 2012, Springer-Verlag London. p. 17-18.
117. Gonzalez-Vazquez, J., J.A. Anta, and J. Bisquert, *Random walk numerical simulation for hopping transport at finite carrier concentrations: diffusion coefficient and transport energy concept.* Physical Chemistry Chemical Physics, 2009. **11**(44): p. 10359-10367.
118. Anta, J.A., *Random walk numerical simulation for solar cell applications.* Energy & Environmental Science, 2009. **2**(4): p. 387-392.
119. Kopidakis, N., et al., *Temperature dependence of the electron diffusion coefficient in electrolyte-filled ${\mathrm{TiO}}_{2}$ nanoparticle films: Evidence against multiple trapping in exponential conduction-band tails.* Physical Review B, 2006. **73**(4): p. 045326.
120. Hagfeldt, A., et al., *Dye-Sensitized Solar Cells.* Chemical Reviews, 2010. **110**(11): p. 6595-6663.
121. Miller, A. and E. Abrahams, *Impurity conduction at low concentrations.* Physical Review, 1960. **120**(3): p. 745.
122. Ma, J. and L.-W. Wang, *Nanoscale charge localization induced by random orientations of organic molecules in hybrid perovskite CH3NH3PbI3.* Nano letters, 2014. **15**(1): p. 248-253.
123. Oku, T., *Crystal structures of CH3NH3PbI3 and related perovskite compounds used for solar cells*, in *Solar Cells-New Approaches and Reviews*. 2015, InTech.
124. Shi, J., et al., *Interfaces in perovskite solar cells.* Small, 2015. **11**(21): p. 2472-2486.
125. Lee, S., et al., *Nb-doped TiO2: a new compact layer material for TiO2 dye-sensitized solar cells.* The Journal of Physical Chemistry C, 2009. **113**(16): p. 6878-6882.
126. Zhou, H., et al., *Interface engineering of highly efficient perovskite solar cells.* Science, 2014. **345**(6196): p. 542-546.
127. Wojciechowski, K., et al., *Sub-150 C processed meso-superstructured perovskite solar cells with enhanced efficiency.* Energy & Environmental Science, 2014. **7**(3): p. 1142-1147.
128. Nelson, J., *The Physics of Solar Cells*, in *The Physics of Solar Cells*. 2010, Imperial College Press. p. 88-89.
129. Casalegno, M., G. Raos, and R. Po, *Methodological assessment of kinetic Monte Carlo simulations of organic photovoltaic devices: The treatment of electrostatic interactions.* The Journal of chemical physics, 2010. **132**(9): p. 094705.
130. Tipler, P.A. and G. Mosca, *Physics for scientists and engineers*. 2007: Macmillan.
131. Sherkar, T.S., et al., *Improving Perovskite Solar Cells: Insights From a Validated Device Model.* Advanced Energy Materials, 2017.
132. HPC, i. *What is a cluster?* ; Available from: https://insidehpc.com/hpc101/intro-to-hpc-whats-a-cluster/.
133. *HPC & Cluster Computing*. Available from: https://www.sdstate.edu/information-technology/hpc-cluster-computing.
134. *PuTTY: a free SSH and Telnet client*. 2018; Available from: https://www.chiark.greenend.org.uk/~sgtatham/putty/.

135. *WinSCP Free SFTP.SCP and FTP client for Windows*. Available from: https://winscp.net/eng/download.php.
136. University, S.H. *Beers's Law*. Available from: https://teaching.shu.ac.uk/hwb/chemistry/tutorials/molspec/beers1.htm.
137. College, M. *UV Visible Absorption Spectroscopy*. Available from: http://faculty.sdmiramar.edu/fgarces/LabMatters/Instruments/UV_Vis/Cary50.htm.
138. ChemViews. *100th Anniversary of the Discovery of X-ray Diffraction*. 2012; Available from: https://www.chemistryviews.org/details/ezine/2064331/100th_Anniversary_of_the_Discovery_of_X-ray_Diffraction.html.
139. nanosurf. *How AFM works*. Available from: https://www.nanosurf.com/en/how-afm-works/history-and-background-of-afm.
140. MichiganTech. *Module Components*. Available from: http://www.phy.mtu.edu/nue/afm.htm.
141. Lab, B.B.a.M. *Basic AFM operation*. 2014; Available from: http://www.iupui.edu/~bbml/afmintro.shtml.
142. Benatar, R.H.a.L. *A practical guide to Scanning Probe Microscopy*. 2000.
143. parksystems. *Phase Imaging*. Available from: https://www.parksystems.com/index.php/park-spm-modes/91-standard-imaging-mode/221-phase-imaging-phase-detection-microscopy-pdm.
144. JEOL. *Scanning Electron Microscope A To Z*. Available from: https://www.jeol.co.jp/en/applications/pdf/sm/sem_atoz_all.pdf.
145. Vickers, E.T., et al., *Improving Charge Carrier Delocalization in Perovskite Quantum Dots by Surface Passivation with Conductive Aromatic Ligands.* ACS Energy Letters, 2018. **3**(12): p. 2931-2939.
146. Venkatesan, S., *Engineering Nanomophology in Polymer Solar Cells for Effiecient Charge Transport.* 2014.
147. instruments, n.s. *Optical Profilometry*. Available from: https://www.nanoscience.com/techniques/optical-profilometry/.
148. Zhao, Y., G.-C. Wang, and T.-M. Lu, *Characterization of Amorphous and Crystalline Rough Surface--Principles and Applications*. Vol. 37. 2000: Elsevier.
149. Mechanical Sensors, C.L.T., Qiao, *Sensors and Measurements.* South Dakota State University, 2016.
150. Watkins, P.K., A.B. Walker, and G.L.B. Verschoor, *Dynamical Monte Carlo Modelling of Organic Solar Cells: The Dependence of Internal Quantum Efficiency on Morphology.* Nano Letters, 2005. **5**(9): p. 1814-1818.
151. Vasilopoulou, M., et al., *Hydrogen and nitrogen codoping of anatase TiO 2 for efficiency enhancement in organic solar cells.* Scientific reports, 2017. **7**(1): p. 17839.
152. Fernandes, S.L., et al. *Hysteresis dependence on $CH_3NH_3PbI_3$ deposition method in perovskite solar cells*. in *SPIE Optics + Photonics for Sustainable Energy*. 2016. SPIE.
153. Agarwal, S. and P.R. Nair, *Pinhole induced efficiency variation in perovskite solar cells.* arXiv preprint arXiv:1704.06605, 2017.

154. Milot, R.L., et al., *Temperature‐dependent charge‐carrier dynamics in CH3NH3PbI3 perovskite thin films.* Advanced Functional Materials, 2015. **25**(39): p. 6218-6227.
155. Johnston, M.B. and L.M. Herz, *Hybrid perovskites for photovoltaics: charge-carrier recombination, diffusion, and radiative efficiencies.* Accounts of chemical research, 2015. **49**(1): p. 146-154.
156. González, T. and D. Pardo, *Physical models of ohmic contact for Monte Carlo device simulation.* Solid-State Electronics, 1996. **39**(4): p. 555-562.
157. Piatkowski, P., et al., *Direct monitoring of ultrafast electron and hole dynamics in perovskite solar cells.* Physical Chemistry Chemical Physics, 2015. **17**(22): p. 14674-14684.
158. Baidya, P.M., *Impact of donor/acceptor interface and an interfacial buffer layer on performance characteristics of bulk heterojunction solar cells: A kinetic monte carlo study*, in *Department of Electrical Engineering and Computer Science*. 2013, South Dakota State University. p. 110.
159. !!! INVALID CITATION !!! [158-161].
160. Venkatesan, S., et al., *Origin of high carrier mobility and low residual stress in RF superimposed DC sputtered Al doped ZnO thin film for next generation flexible devices.* 2018.
161. Veeco, *DEKTAK 150 SURFACE PROFILER USER'S MANUAL*, Veeco, Editor. 2009.
162. Yao, Z., et al., *CH3NH3PbI3 grain growth and interfacial properties in meso-structured perovskite solar cells fabricated by two-step deposition.* Science and Technology of Advanced Materials, 2017. **18**(1): p. 253-262.
163. Yusoff, A.R.b.M. and M.K. Nazeeruddin, *Organohalide lead perovskites for photovoltaic applications.* The journal of physical chemistry letters, 2016. **7**(5): p. 851-866.
164. Cohen, B.-E., et al., *Impact of antisolvent treatment on carrier density in efficient hole-conductor-free perovskite-based solar cells.* The Journal of Physical Chemistry C, 2015. **120**(1): p. 142-147.
165. Liu, D., M.K. Gangishetty, and T.L. Kelly, *Effect of CH 3 NH 3 PbI 3 thickness on device efficiency in planar heterojunction perovskite solar cells.* Journal of Materials Chemistry A, 2014. **2**(46): p. 19873-19881.
166. Tress, W., et al., *Understanding the rate-dependent J–V hysteresis, slow time component, and aging in* $CH_3NH_3PbI_3$ *perovskite solar cells: the role of a compensated electric field.* Energy & Environmental Science, 2015. **8**(3): p. 995-1004.
167. Mabrouk, S., et al., *Higher efficiency perovskite solar cells using additives of LiI, LiTFSI and BMImI in the PbI 2 precursor.* Sustainable Energy & Fuels, 2017. **1**(10): p. 2162-2171.
168. Jiang, C.-S., et al., *Carrier separation and transport in perovskite solar cells studied by nanometre-scale profiling of electrical potential.* Nature communications, 2015. **6**.
169. Bi, D., et al., *Unraveling the effect of PbI2 concentration on charge recombination kinetics in perovskite solar cells.* Acs Photonics, 2015. **2**(5): p. 589-594.

170. Wu, Y., et al., *On the origin of hysteresis in perovskite solar cells.* Advanced Functional Materials, 2016. **26**(37): p. 6807-6813.
171. Wu, F., et al., *Inverted Current–Voltage Hysteresis in Perovskite Solar Cells.* ACS Energy Letters, 2018. **3**(10): p. 2457-2460.
172. Wu, F., et al., *Bias-Dependent Normal and Inverted J–V Hysteresis in Perovskite Solar Cells.* ACS applied materials & interfaces, 2018. **10**(30): p. 25604-25613.
173. Yang, W., Y. Yao, and C.-Q. Wu, *Origin of the high open circuit voltage in planar heterojunction perovskite solar cells: role of the reduced bimolecular recombination.* Journal of Applied Physics, 2015. **117**(9): p. 095502.
174. Zhang, B., et al., *Carrier Transport in CH3NH3PbI3 Films with Different Thickness for Perovskite Solar Cells.* Advanced Materials Interfaces, 2016. **3**(17).